Demonstrating High Performing Thermophotovoltaic Systems Using Novel Cell-Side Architectures

by

Bosun A. Roy-Layinde

A dissertation submitted in partial fulfillment
of the requirements for the degree of
Doctor of Philosophy
(Chemical Engineering)
in the University of Michigan
2024

Doctoral Committee:

Professor Andrej Lenert, Chair
Professor Mark Burns
Professor Stephen R. Forrest
Assistant Professor Xiwen Gong

Bosun A. Roy-Layinde

roybosun@umich.edu

ORCID iD: 0000-0003-2388-0218

Dedication

If you know where I came from, you'll be pleased with where I'm going next.

To my parents, Toyin, and Nureni.

To my siblings, Ayo and Eniola.

To my partner, Ifeoma Maduewesi.

To the Grace that life has bestowed upon me.

To all who have been a part of my journey.

To all those who are dreaming, keep it going.

Acknowledgments

It is hard to thank everyone who has helped me in this four-page chapter because, in my experience, it takes a village to raise a child. Please forgive me if I forget to include your name.

Firstly, I would like to thank my research advisor, Professor Andrej Lenert, who has been a solid support system for me in the last few years. Your patience in guiding me through the intricacies of research, your persistent push for excellence, and the constructive feedback you've provided have been instrumental in shaping me into a better researcher. Your ability to care for your students as individuals, not just as researchers, has made a lasting impact on my life. I want you to know that I look up to you not only as a mentor but also as a role model. The lessons I have learned from you extend beyond the laboratory and have shaped me into a better person. As I prepare to step into the real world, I find myself grappling with the fear of not finding a support system as good as the one I've been fortunate to have in your research group. The care and mentorship you've provided feel like a protective bubble, and the thought of leaving it is daunting. I am scared that people in the real world might not be as exceptional as you have been. However, I take comfort in the fact that the values and skills you've instilled in me will serve as a guiding light. Your mentorship has equipped me with the tools to navigate the challenges that lie ahead, and for that, I am eternally grateful. To Professor Forrest, I have learned not only the nuances of my field but also the importance of resilience and perseverance under your guidance. Your mentorship has been nothing short of transformative. To the rest of my thesis committee, Professor Mark Burns and Professor Xiwen Gong, thank you for your immense inputs and guidance.

To the first members of the Lenert lab, Hannah, Tobias, Sean, Alex and Zach, thank you for welcoming me into the lab with open arms. I want to appreciate each of you for contributing to the creation of an outstanding work culture. The collaborative spirit, mutual respect, and shared dedication to our research goals have fostered an environment where everyone's contributions are valued. Moreover, the enjoyable and fun atmosphere that permeates our workspace made every day a joy. Whether it's the lighthearted moments during breaks, shared laughter over challenges, or the occasional team-building activities, your commitment to creating a positive and uplifting environment is forever appreciated. To the current members of Lenert lab, Areefa, Andres, Carissa, Seungwon, Michael and Yiwei, thank you for keeping the amazing culture alive. In essence, I am grateful to be part of a team that not only excels in research but also values each member's well-being and growth. Your collective efforts have made this lab an extraordinary place to work, and I am honored to be a part of it. To my amazing undergrad, Arijit Jatkar, you are one exceptional student. I am glad to have worked with you. To Areefa and Seugwon, I am excited to see how you both will move our research field forward. I am always rooting for you both.

To my research mentors turned friends, Tobias Burger, and Jihun Lim, thank you for your patience and teachings. From the beginning of my journey in research, you have been more than mentors; you have been my guides, patiently leading me through the complexities of our field. Your commitment to teaching me the fundamental principles has laid a solid foundation for my understanding and has been crucial in shaping my approach to research challenges. I wish you the best in your future endeavors.

To my academic and life mentors, James Akinola, Solomon Oyakhire, Korede Akinpelumi, Chinedu Moghalu and Nanko Madu, thank you for inspiring me. Mr Moghalu, in particular, has served as a pillar of support since the beginning. He celebrates my successes as if I were his son.

To my friends turned families here at UofM, Gbemileke, Kenny, Seun, Tosin, Fiki, Olamide, James, Samuel, Nnaemeka, Chris, Luke, Carissa, Onyema and Awwal, thank you for the memories. I will forever cherish them close to my hearts. Specifically, Gbemileke, the best roommate anyone can ever ask for. Thank you, for being not just a roommate but a steadfast supporter, a collaborative partner, and a friend. I look forward to celebrating your achievements and witnessing the great heights you are destined to reach in your academic endeavors. To my friends and cousins outside UofM, Tunde, Seun, Fuad, Demola, Adebisi, Anselem, Taofeek, Ayomikun, Monwe, Chike, Bonez, Kush, Osho, Buchi, Wale, Yemi, Gala and so many others, I appreciate you all so much. I am looking forward to our future memories together.

To my siblings, Ayoola and Eniola, you are, without a doubt, the best siblings in the world. Your love transcends the physical distance, reaching across continents and bridging the gap between us. I miss you both dearly, and the distance only serves to deepen the appreciation I have for the both of you. Your encouragement and love have been a pillar of strength, motivating me to persevere through the academic journey. Even in our physical separation, you are always present in my thoughts, and your unwavering support has been a driving force behind my achievements. To you both, I express my deepest love and gratitude. You are my anchors, my constants, and the embodiment of familial love. The journey may be long, but the reunion will be sweet, and I look forward to the day when we can once again be together, sharing in the joys of life.

To my father, Nureni, thank you for the consistent support and prayers. To my mother, Toyin, I don’t know how to thank you in a few words. Despite the physical distance that separates us, your love and encouragement have transcended borders, shaping my academic pursuit in ways words cannot fully capture. Your consistent checks, caring messages, and genuine interest in my well-being have provided solace during challenging times. It is your reassuring voice that echoes

in my mind when faced with adversity, reminding me that I am not alone in this academic endeavor. Despite your limited understanding of the intricate details of my research, my mom has never failed to inquire about my work. Beyond emotional support, my parents have played a pivotal role in ensuring my physical well-being. From sending medications all the way from Nigeria to monitoring my health from afar, they have shown a level of dedication that goes beyond the call of parenthood. Their selflessness has not only eased the burdens of distance but has also emphasized the importance of familial bonds in the pursuit of knowledge.

To my partner, Ifeoma, your laughter, encouragement, and shared moments of happiness have provided a respite from the rigors of research and have made this journey not just academically fulfilling, but personally enriching. You have played a crucial role in helping me navigate the intricacies of life in the United States. From providing guidance on cultural nuances to helping me adapt to a new environment, your insights have been instrumental in making this transition smoother. Your willingness to be a partner in every sense has eased the challenges of being away from home and has made the United States feel like a second home. In moments of celebration and in times of despair, my partner's presence has been my constant. This acknowledgment is a humble tribute to a woman whose love, resilience, and unwavering belief in my potential have been the guiding lights on this scholarly odyssey. I am excited to see what the future holds for us.

Table of Contents

List of Tables

List of Figures

Abstract

Thermophotovoltaic (TPV) generation is the conversion of thermal radiation to electrical power through the photovoltaic effect. This is a promising approach for various energy applications such as cogeneration of heat and power, thermal energy storage, and waste heat recovery. However, current TPV efficiency levels are insufficient for widespread implementation of these systems. This thesis aimed to overcome this gap by gaining a detailed understanding of energy losses in thin-film TPV cells and establishing scalable fabrication strategies to minimize them. The research focuses on an innovative photovoltaic architecture featuring an active semiconductor layer suspended over wide air cavities. The air-bridge cell maximizes refractive index contrast and minimizes the loss of long-wavelength (out-of-band) photons, thereby increasing conversion efficiency. Each chapter addresses a key challenge related to maximizing photon recovery and utilization in air-bridge TPVs: (Ch. 2) understanding the limitations of air-bridge cells based on InGaAs, (Ch. 3) experimentally demonstrating high efficiency air-bridge cells that circumvents these limitations, (Ch. 4) demonstrating transmissive spectral control as an alternative to reflective control, (Ch. 5) developing a novel approach to realizing tandem TPV cells that overcomes the challenges of conventional approaches.

Through this research, significant gains were obtained in understanding energy losses in these devices and in their overall performance and reliability. Detailed optical and electronic simulations identified key losses in heterojunction cells, resulting in device architectures capable of high TPV conversion efficiencies throughout a broad range of emitter temperatures (1000 to 1500 ºC). Notably, an air-bridge cell with a 0.9 eV bandgap achieved nearly 45% efficiency at

1400 ºC emitter temperatures by optimally balancing photon and carrier utilization. Furthermore, novel bifacial devices without back surface reflectors demonstrated efficiencies over 30% at significantly lower emitter temperatures compatible with waste heat streams and nuclear power. Both results represent an 8% absolute efficiency gain compared to prior results in their temperature ranges, largely credited to the near-complete recovery of long-wavelength photons in air-bridge cells. In addition, the research also led to the development of designs and fabrication processes which increased reliability of both single junction and tandem devices. Tandem devices featuring two air-bridge subcells were implemented in a range of semiconductors, demonstrating a way to achieve comparable optical properties to single junction air-bridge cells by avoiding the use of tunnel junctions.

Overall, these results suggest the applicability of the air-bridge cells to a range of semiconductor systems suitable for electricity generation from thermal sources found in both consumer and industrial applications. The combination of ultra-high efficiency, low emitter temperatures, and device stability could allow widespread adoption of TPV systems, including their use in long-duration thermal batteries. Thermal batteries equipped with such TPV cells can achieve competitive roundtrip efficiencies with electrochemical approaches, while maintaining their lower costs, which are sufficiently low to enable a fully renewable grid.

Chapter 1: Introduction

1.1 Thermophotovoltaic power generation

Thermophotovoltaic (TPV) generators use the photovoltaic effect to convert infrared radiation from a thermal emitter into electrical power. TPV conversion of thermal radiation to electrical power is a readily scalable process for on-demand electricity generation. A TPV system consists of two major parts, a thermal emitter and a photovoltaic cell in close proximity, as shown in Figure 1.1. Heat supplied by an upstream primary energy source maintains the emitter at elevated temperatures (>1000 K) which drives emission of infrared radiation. Photons with energy greater than the cell's bandgap (in-band) excite electron-hole pairs. Meanwhile, absorption of emitted photons with energy less than the bandgap (out-of-band) generates undesirable low-grade waste heat.

TPV systems differ from solar photovoltaics in two major ways. First, the thermal emitter is cooler than the Sun which is approximately at 6000°C. Second, TPV cells are typically placed near the heat source (milimeter scale distances). Because of their proximity to the heat source, TPVs can produce orders of magnitude more electrical power than rooftop solar PVs. The elevated power density of TPVs can justify the use of high quality III-V cells and their corresponding substrates. Furthermore, the solid-state architecture of TPVs, with few or no moving parts, makes it a promising approach for a variety of renewable energy application as discussed below.

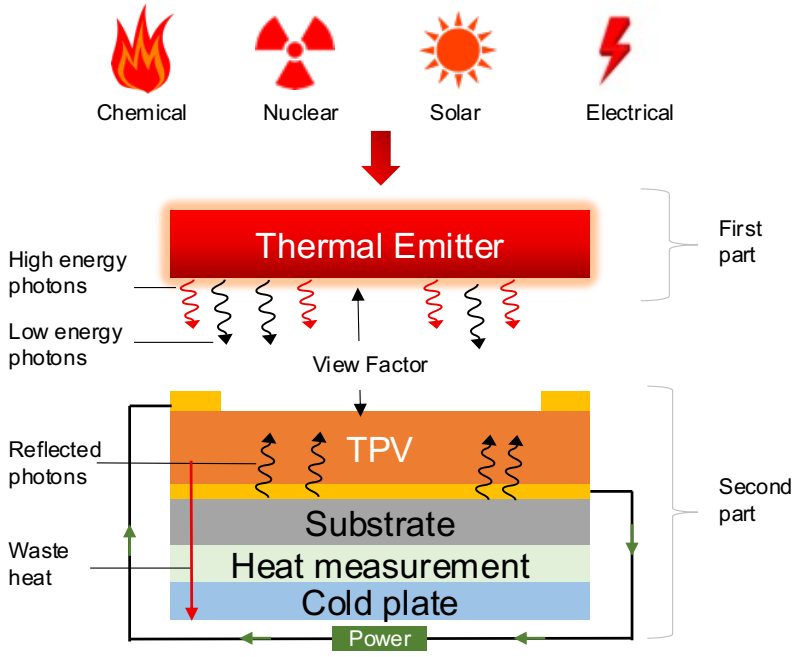

Figure 1.1 TPV system schematic and heat flow. Primary sources of energy such as solar supplies heat to the thermal emitter which drives emission in the mostly infrared regime. The TPV cell with a known bandgap absorbs photons with energy greater than the bandgap to produce electrical power while recycling low energy photons back to the emitter to be reabsorbed.

1.2 TPV utilization in emerging technologies

1.2.1 Thermal energy grid storage

With the cost of renewable electricity falling substantially over the last decade, one of the most pressing technological challenges to reaching high renewable penetration has become the deployment of short and long-term energy storage. The energy storage sector is dominated by pumped-storage hydropower (PH) and lithium-ion batteries. Thermal energy grid storage (thermal batteries) is an alternative storage technology that has the potential to overcome these challenges and meet the growing unmet need for low-cost, long-term stationary energy storage. Thermal batteries utilize storage minerals that are abundant in the earth's crust, easily accessible, and cost-

effective. This is in contrast to the present battery systems that heavily depend on lithium. In addition, thermal batteries have small footprint and may be installed in any location, unlike pumped hydro systems. During low demand periods, excess renewable electricity from the grid is absorbed by thermal batteries to resistively heat earth-abundant materials such as graphite, silicon, or ceramic blocks[1–4], as shown in Figure 1.2. This step represents the charging phase. The high-temperature materials can retain heat for days or months. When there is demand for power, TPVs can be utilized to convert this stored heat into electricity (discharge phase) that can be fed back into the grid. This energy storage approach provides a fast, modular, and low-cost alternative to energy storage, hence increasing grid resilience. It is crucial to note that the round-trip efficiency of this system is determined by the efficiency of TPV conversion (discharge phase) since the efficiency of converting electricity to heat (charging phase) can be close to perfect (100%).

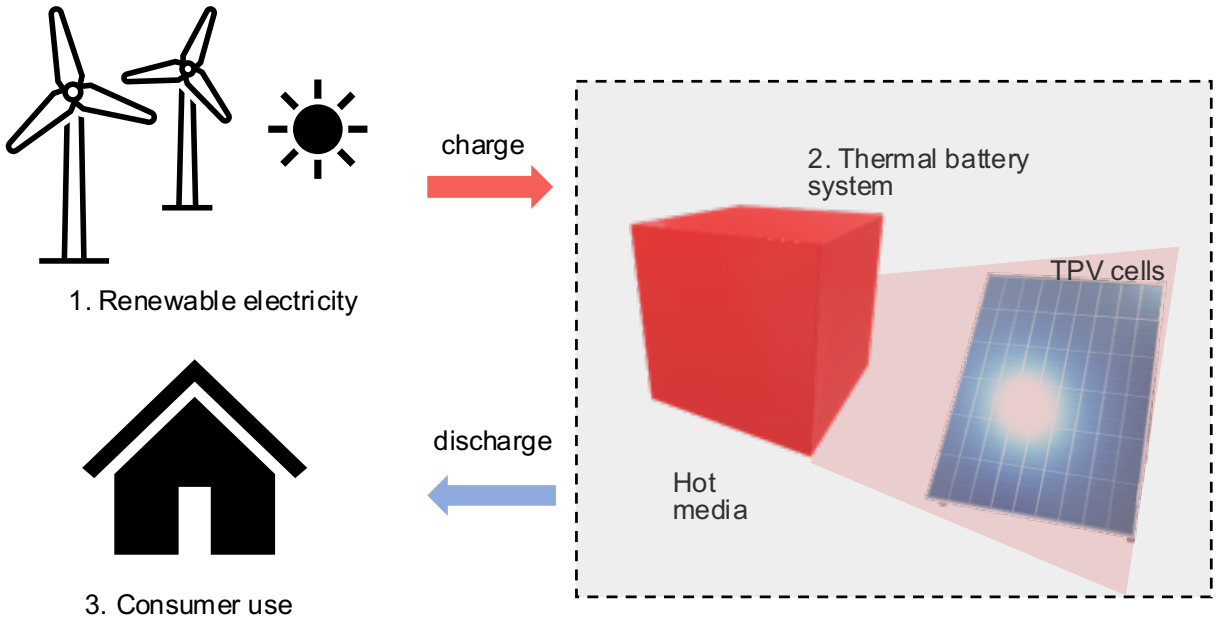

Figure 1.2 Use of TPVs in thermal energy grid storage. The hot media stores renewable electricity from the grid, and when needed, TPV cells transform this heat back into electricity.

1.2.2 Cogeneration of heat and power

In addition to harnessing the power generated by TPV cells, the surplus heat they produce can be effectively utilized for residential and space water heating[5,6]. Previous studies have identified various system configurations that can be employed to utilize TPVs in a cogeneration setup within a completely electrified building[2]. This application of TPV has the potential to be integrated with thermal energy grid storage, thereby enhancing its economic value.

1.2.3 Waste heat recovery

A large portion of global industrial energy use and emissions is due to cement, chemical, iron, and steel production. These sectors have significant waste heat streams at temperatures ranging from 700 to 1100°C. These high-temperature waste heat can be used to power an emitter (such as graphite or tungsten) that generates infrared radiation, which is then converted to electrical power using TPV cells, lowering the input power required for industrial operations. The utilization of TPVs in this application represents a solid-state solution for recovering waste heat in a renewable way[7,8]. Other applications for TPVs include space, nuclear heat, direct solar conversion, and concentrated solar thermal.

1.3 State-of-the art performance

There has been a rising interest in the use of TPVs because of its scale-insensitive performance above 1-10 kW[9] which is particularly desirable in applications such as remote power generation and co-generation of heat and power near the point of use[10–13]. Further, because of its capacity for near-instantaneous power ramping, which is important for regulating the supply of intermittent

renewable energy sources like wind and solar[14–16], notable advances have been made in TPV cells in the last decade as shown in Figure 1.3a. These advancements have been demonstrated in a variety of contexts, including: (1) materials ranging from inexpensive silicon to more expensive thin-film III-V cells such as InGaAs[17–23], GaAs[18,24], GaSb[6], and InGaAsSb[25,26]; (2) single junction designs and tandem configurations of cells[4,27,28] (3) Emitter temperatures ranging from 800°C to 2300°C employing different emitter materials, and (4) active cell sizes ranging from small cells to monolithic interconnected modules (MIM)[25,29,30]. Figure 1.3b depicts the state-of-the-art efficiencies for several materials as a function of their characterized emitter temperature at the time of writing this thesis.

Some studies in the literature have focused on increasing efficiency by improving charge carrier management through effective metal gridline design to reduce resistance losses, increasing cell bandgap to maximize output voltage, multi-junction design to increase output power, and an efficient thermal management system to maintain performance while in operation.

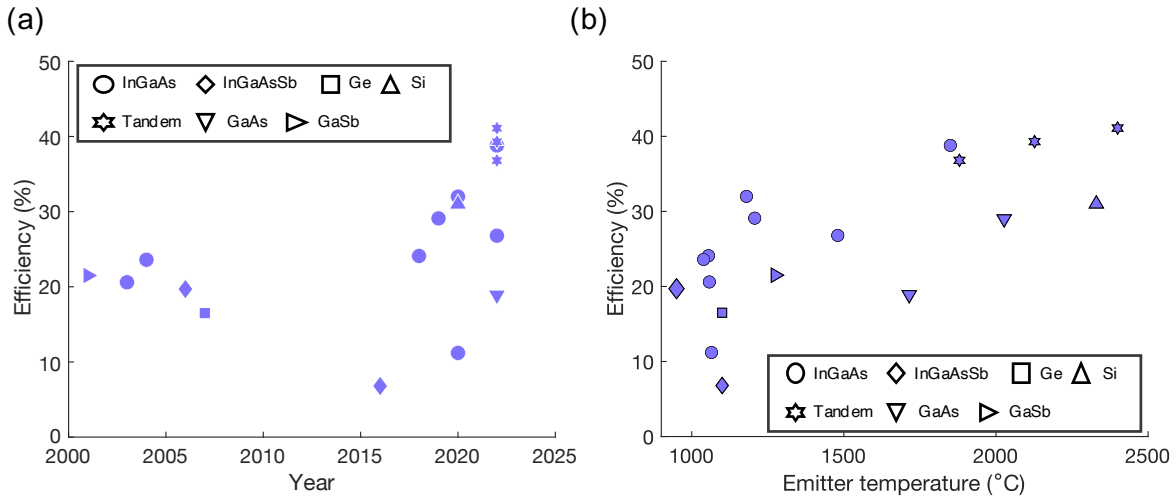

Figure 1.3 State-of-the-art efficiency. (a) Historical progress of efficiency for various leading TPV cell materials. (b) Efficiency as a function of corresponding emitter temperatures.

Others have focused on improved efficiency using spectral control strategies, such as designing selective emitters[31–39] that preferentially emit useful radiation or architectures that minimize the absorption of undesired photons in the cell. These architectures may include a front surface filter[40–43] (FSF) that prevents undesired low energy photons from entering the cell and/or a back surface reflector (mirror) that redirects unwanted low energy photons back to the emitter[19,20,41,44]. This is accompanied with some epitaxial lift off to remove the growth substrate, effectively avoiding parasitic absorption in the substrate. Others have added a low-index layer[44,45] (dielectric spacer) between the absorber and the rear metal to increase back surface reflection even more. This results in a refractive index mismatch, which increases reflection according to Snell's law. Recently, my collaborators Tobias Burger and Dejiu Fan, used air as the low-index layer between the absorber and the rear metal, thereby reducing Fresnel's losses at the metal-air interface[19]. This airbridge cell (ABC) architecture is a promising approach to improve the efficiency of TPV systems by enabling near-perfect reflection of undesired low energy photons, thereby overcoming the performance of prior spectral control strategies[46–55,56]. Specifically, the addition of a ~600-nm deep air pocket below an $In_{0.53}Ga_{0.47}As$/InP heterojunction improves the efficiency of converting absorbed thermal radiation into electrical power from approximately 23% to 32%[57]. This airbridge architecture sets the foundation for my thesis.

1.4 TPV power conversion efficiency

TPV power conversion efficiency η_{TPV} is given by the ratio of the output electrical power P_{out} to the heat absorbed Q_{abs} by the cell[58–62]. [63]Because the temperatures of the thermal emitter are well below that of the sun, a large fraction of the incident spectrum is at photon energies less than the

cell's bandgap. This is undesirable because it increases waste heat generation Q_c, which raises the heat absorbed Q_{abs} by the cell, resulting in lower cell efficiency.

$$\eta_{TPV} = \frac{P_{out}}{Q_{abs}} = \frac{P_{out}}{Q_{inc}+Q_{ref}} = \frac{P_{out}}{P_{out}+Q_c} \quad (1.1)$$

This metric does not account for upstream losses associated with primary energy conversion and corresponding heat transfer, as well as cavity losses associated with imperfections such as the inactive surfaces on the cell and convective loss from the thermal emitter[63]. In thermal batteries, losses occurring in conversion of electrical energy to heat and thermal storage would be considered upstream losses. These losses are expected to be small (<10%) in well-insulated grid-scale systems due to their low surface-to-volume ratios. Similarly, cavity losses are expected to be negligible at larger scales such as >1 kW, which are beyond the scope of this thesis. Thus, in the case of large thermal batteries, η_{TPV} governs the overall system efficiency. TPV efficiency can be further decoupled into two key meaningful metrics (spectral management and carrier management efficiency) as discussed below.

1.4.1 Spectral management

Spectral management efficiency (*SE.IQE*), denoted as the product of the spectral efficiency *SE* and the internal quantum efficiency *IQE*, primarily describes how efficiently the absorbed photons are utilized to excite charge carriers and converted to short-circuit current J_{SC}[59,64]. Spectral utilization, in turn, is dominated by the sub-bandgap (out-of-band) wavelength range. The importance of this range can be appreciated by noting that even though an object at 1500°C emits a large amount of visible light, the peak of the emission spectrum is still in the infrared (IR), and the vast majority of the power is situated at photon energies below the bandgap of the cell. For example, for a cell with a bandgap of 0.74eV under 1500°C blackbody irradiation, 75% of the irradiation is in the

undesired out-of-band (OOB) range, as illustrated in Figure 1.4a. This OOB fraction of power increases as the emission temperature decreases. Consequently, it is imperative to effectively manage the emission and absorption of these undesired OOB photons by reflecting them back to the hot emitter. This serves the dual purpose of minimizing waste heat produced by the cell and enhancing the power conversion efficiency.

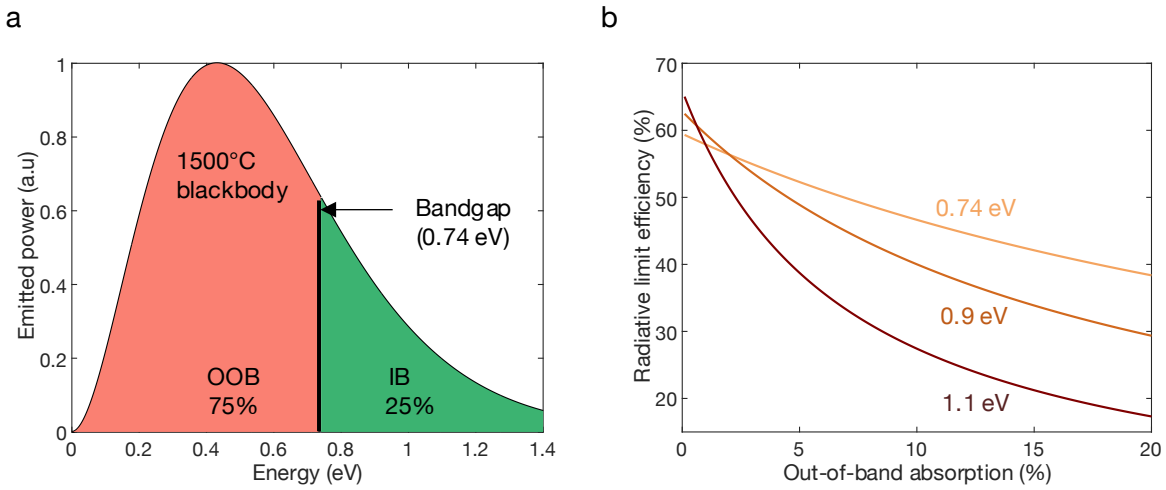

Figure 1.4 Effect of out-of-band absorption on spectral management (a) Emitted power as a function of photon energy for a 1500°C blackbody spectrum. 25% of the spectrum is in the in-band (IB) regime while 75% is in the undesired OOB regime. (b) Radiative limit efficiency as a function of OOB absorption for three bandgap materials.

Photon recovery/recuperation methods may include deliberately suppressing these out-of-band (OOB) photons from the emitter using spectral engineering (emissive control), allowing the OOB photons transmit through the cell to a secondary emitter, or reflecting this OOB radiation back to the emitter until it is reenergized and emitted at a high enough energy to be converted. The upper bound efficiency, known as the radiative limit because it neglects non-radiative carrier recombination, is highly dependent on OOB photon absorption. Regardless of the cell's bandgap, Figure 1.4b shows a substantial drop in efficiency as OOB absorption increases. When OOB

absorption approaches zero (i.e., OOB reflection is near-unity), the larger bandgap cell exhibits a higher radiative limit efficiency. This is because complete suppression of OOB absorption minimizes the conventional temperature-bandgap trade-off, allowing wider bandgap materials to be employed without incurring significant spectral management cost. Asides from parasitic absorption of low energy photons, other factors that contribute to poor spectral management may include reflectance or parasitic absorption of in-band photons, thermalization of high energy photons and short diffusion lengths of photogenerated carriers (IQE losses)[59,64].

1.4.2 Charge carrier management

Charge carrier management *VF.FF*, denoted as the product of the voltage factor *VF* and the fill factor *FF*, describes how well excited charge carriers are collected to maximize output voltage. Voltage factor *VF*, which is the ratio of the open circuit voltage V_{OC} to the bandgap voltage E_g, quantifies how well the bandgap is utilized[59,64]. The fill factor *FF* is the ratio of the maximum power produced P_{MPP} to the product of J_{SC} and V_{OC}. Charge carrier management captures imperfections related to material defects, non-radiative recombination of excited carriers, ohmic losses due to series resistance and inadequate thermal management resulting in cell heating.

1.5 Experimental quantification of TPV efficiency

1.5.1 Output power

To measure the electrical power, the conventional approach is to sweep voltage across the junction and then measure the current produced. The power generated P_{out} is a product of the voltage and

current measured. These measurements are conducted using a four-point probe wire configuration to eliminate any external resistance introduced by the wires.

1.5.2 Heat absorption measurement

Unlike P_{out}, the methods used to measure heat transfer to the TPV cells are more varied. There are two general methods in literature for measuring heat absorbed, broadly categorized as optical and calorimetry methods as shown in Figure 1.5. In the optical method, the heat absorbed for a reflective cell is measured as the difference between the power from photons incident Q_{inc} on the cell and the power from photons reflected Q_{ref} from the cell[20,23,26,40,65–67]. This method requires that the optical properties of the cell and emitter are well characterized under relevant operating conditions. Furthermore, parameters such as geometric view factor are required to accurately quantify the radiative exchange between the cell and emitter. For the calorimetry methods, the heat absorbed is calculated as the sum of the waste heat Q_c generated by the cell and the power produced P_{out} by the cell[4,28,68–72].

For optical measurement, commonly accessible instruments such as the Fourier Transform Infrared (FTIR) and UV-Vis-NIR spectroscopy are used to measure the optical properties of both the cell and the emitter in the wavelength range relevant to high temperature emission. The optical measurements may differ based on the errors in the system, reference sample calibration, base-line correction or inherent noise associated with the tool.

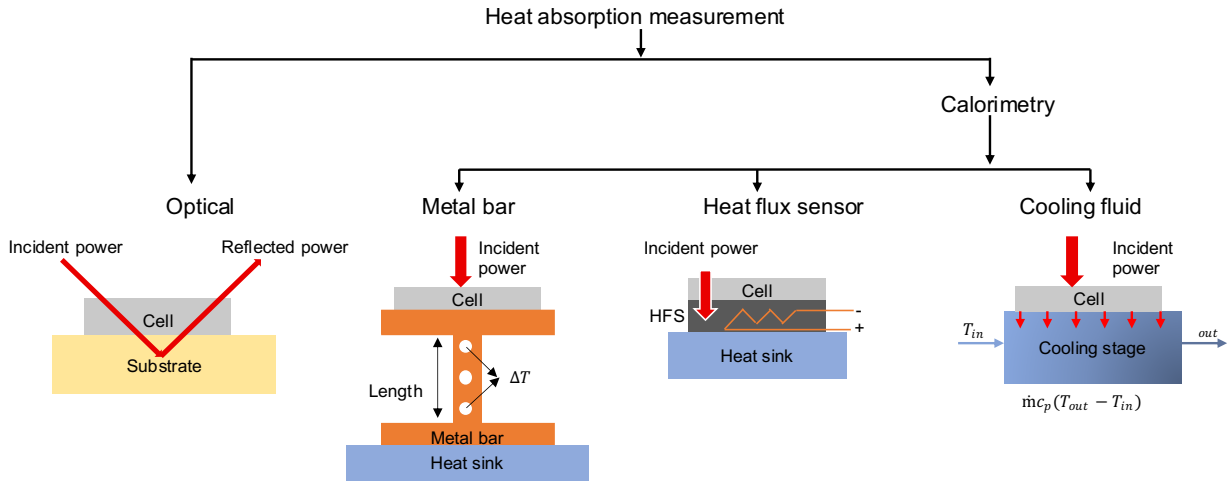

Figure 1.5 Two methods of measuring waste heat in TPV cells. Optical measurements rely on measurement of the reflectance (or absorptance) properties of the cell and emitter. The calorimetry approach is a direct measurement of the waste heat generated by the cell using a metal bar, heat flux sensor, or coolant flow.

Calorimetry measurements rely on concurrent measurements of both the electrical power produced and the waste heat generated by the cell. This method of heat measurement may be advantageous because it does not rely on separate measurement of the cell's reflectance. Metal bar, heat flux sensor (HFS), and coolant flow techniques are commonly utilized. In the metal bar approach, the cell is placed on a metal bar containing evenly spaced temperature readings as shown in Figure 1.5. This approach is based on quantifying heat flow using conductive heat transfer (Fourier's law), in which the thermal conductivity is determined by the metal. The HFS technique relies on the basic principles of the Seebeck effect to generate an output voltage as heat goes through it. The HFS is placed behind the cell to monitor the heat that passes through it. Finally, in the cooling flow technique, the heat rejected by the cell heats a coolant, resulting in a temperature difference between the inlet and outlet fluids. The heat sink is made of conductive material (such as copper and aluminum) and has a coolant running through it.

1.6 Device electrical model

The power generated by a TPV cell is equal to the product of the current J and the voltage V, where J is equal to the photogenerated current density (J_{ph}) minus the current lost to radiative (J_{rad}) and non-radiative recombination (J_{nrad}) according to:

$$J = J_{ph} - (J_{rad} + J_{nrad}) \tag{1.2}$$

Shunt currents are neglected because they are small relative to the overall current density under normal illumination conditions. The other relevant current densities are described as follows:

1.6.1 Photogeneration. J_{ph} is the product of the incident photon flux $b(E, T_h)$, apparent view factor F_v, absorptance of the cell $a(E)$, and the internal quantum efficiency $IQE(E)$ according to:

$$J_{ph} = F_v \cdot q \int_{E_g}^{\infty} a(E) \cdot b(E, T_h) \cdot IQE(E)\, dE, \tag{1.3}$$

where the photon flux is given by Planck's law:

$$b(E, T_h) = \frac{2\pi E^2}{c^2 h^3 \left(\exp\left(\frac{E}{k_B T_h}\right) - 1\right)}. \tag{1.4}$$

Here, E is photon energy, T_h is the emitter temperature, q is the electron charge, c is the speed of light, h is Planck's constant, and k_B is the Boltzmann constant. The absorptance of the cell $a(E)$ is measured and compared to calculations using transfer matrix methods.

1.6.2 Non radiative recombination. The non-radiative recombination current density is given by:

$$J_{nrad} = J_{O1}\left(e^{\frac{qV_I}{k_B T_c}} - 1\right) + J_{O2}\left(e^{\frac{qV_I}{2k_B T_c}} - 1\right) + J_{Aug} \tag{1.5}$$

where J_{O1} is due to thermally generated minority carriers diffusing through into the depletion region, J_{O2} denote the saturation current density generated due to generation and recombination of charge carriers in the depletion region, and J_{Aug} is the Auger recombination current. $V' = V - JR_s$ accounts for the series resistance R_s. Consistent with prior modeling of thin heterojunctions with an n-type InGaAs absorber[73–76], J_{O1} and J_{O2} are approximated as follows:

$$J_{O1} \approx q{n_i}^2 \left(\frac{1}{N_D}\sqrt{\frac{D_p}{\tau_1}}\right) \tag{1.6}$$

$$\text{and} \quad J_{O2} \approx \frac{qn_iW}{\tau_2}, \tag{1.7}$$

where n_i is the intrinsic carrier concentration, N_D is the concentration of donors, τ_1 is the lifetime of minority holes in the quasi-neutral region, D_p is the diffusion coefficient of minority holes, W is the depletion width, and τ_2 is the lifetime in the depletion region. This model uses literature data for modeling the temperature dependence of the bandgap[77]. The dependence of the intrinsic carrier concentration on cell temperature is given by:

$$n_i = \sqrt{N_c \cdot N_v}\exp\left(\frac{-E_g}{2k_BT_c}\right) \tag{1.8}$$

where N_c (N_v) is the effective density of states in the conduction (valence) band.

We note that τ_1, τ_2 and R_s are parameters specific to the ABC and are determined by fitting to experiments as discussed above. Further, the temperature dependencies of τ_1, τ_2 and R_s are assumed to be negligible.

The Auger recombination current is calculated by:

$$J_{Aug} = L(C_n + C_p){n_i}^3 \exp\left(\frac{3qV}{2k_BT_c}\right) \tag{1.9}$$

where L is the thickness of the active region and C_n and C_p are the Auger recombination coefficients for recombination involving two holes and two electrons, respectively. For InGaAs, $C_n = C_p = 8.1 \times 10^{-29}\text{cm}^{-3}$ [78].

1.6.3 Radiative recombination. Current resulting from radiative recombination is given by:

$$J_{rad} = J_{int} + J_{ext} \tag{1.10}$$

where J_{int} describes photons that are parasitically absorbed within the cell by non-luminescent layers (i.e., no quasi-Fermi level splitting), while J_{ext} describes the photons emitted by the cell. J_{int} is calculated can be calculated using the Multilayer Electromagnetic Solver for Heat Transfer[79] following previously reported procedures. J_{ext} is approximated by:

$$J_{ext} = qe^{\frac{qV}{k_B T_c}} \int_{E_g}^{\infty} a(E) \cdot b(E, T_c) \cdot IQE(E)\, dE \tag{1.11}$$

Here, we have used a Boltzmann approximation to describe the voltage-dependent emission. This model allows us to describe the effects of temperature on the *J-V* characteristics and other figures of merit of the TPV.

1.7 Common fabrication techniques

The fabrication steps involved in this dissertation include photolithography, material (metal) deposition, thermocompression bonding (aligned and non-aligned), wet or plasma etching, and metal lift off. This section presents a summary of the steps involved in TPV fabrication.

1.7.1 Photolithography

This is a lithography technique that uses ultraviolet (UV) light to transfer patterns from a mask onto a substrate surface. Typically, this process entails utilizing photoresist materials, which are organic polymers that undergo structural changes upon radiation exposure[80,81]. The viscosity, rotation speed, and spin coating time determine the final thickness of these photoresist materials on the substrate. Following this step, the substrate undergoes a soft-baking process on a hotplate. This serves to enhance the adhesion of the photoresist and eliminate any remaining solvent. The patterns on the mask are transferred to the substrate when it is exposed to UV light. When a positive photoresist is used, the exposed areas can be removed in a developer. In contrast, when a negative resist is utilized, the areas that are exposed to light become insoluble, while the unexposed areas can be easily removed by the developer. Figure 1.6 shows a simple schematic of a photolithography process illustrating the deposition of a positive photoresist onto a substrate.

Following the lithography process, patterns can be created through metal lift-offs or selective etching of specific areas. Metals such as titanium, platinum, chromium, and gold can be deposited using various methods like electro-beam deposition, vacuum thermal evaporation, or sputtering. The metals are subsequently eliminated from the unwanted areas using the metal lift off procedure. An additional type of photoresist called the lift-off resist is necessary for this. A lift-off resist is positioned below the regular photoresist to achieve a precise undercut, which guarantees the elimination of metals in unwanted areas. For the etching procedure, materials are selectively removed via a wet or dry-etching procedure. Wet etching requires the use of a chemical mixture that reacts with the material surface such as hydrochloric acid (HCl) for InP removal. While dry

etching makes uses of plasma, which produce high-energy free radicals, to remove achieve a more precise removal of surface of the target material.

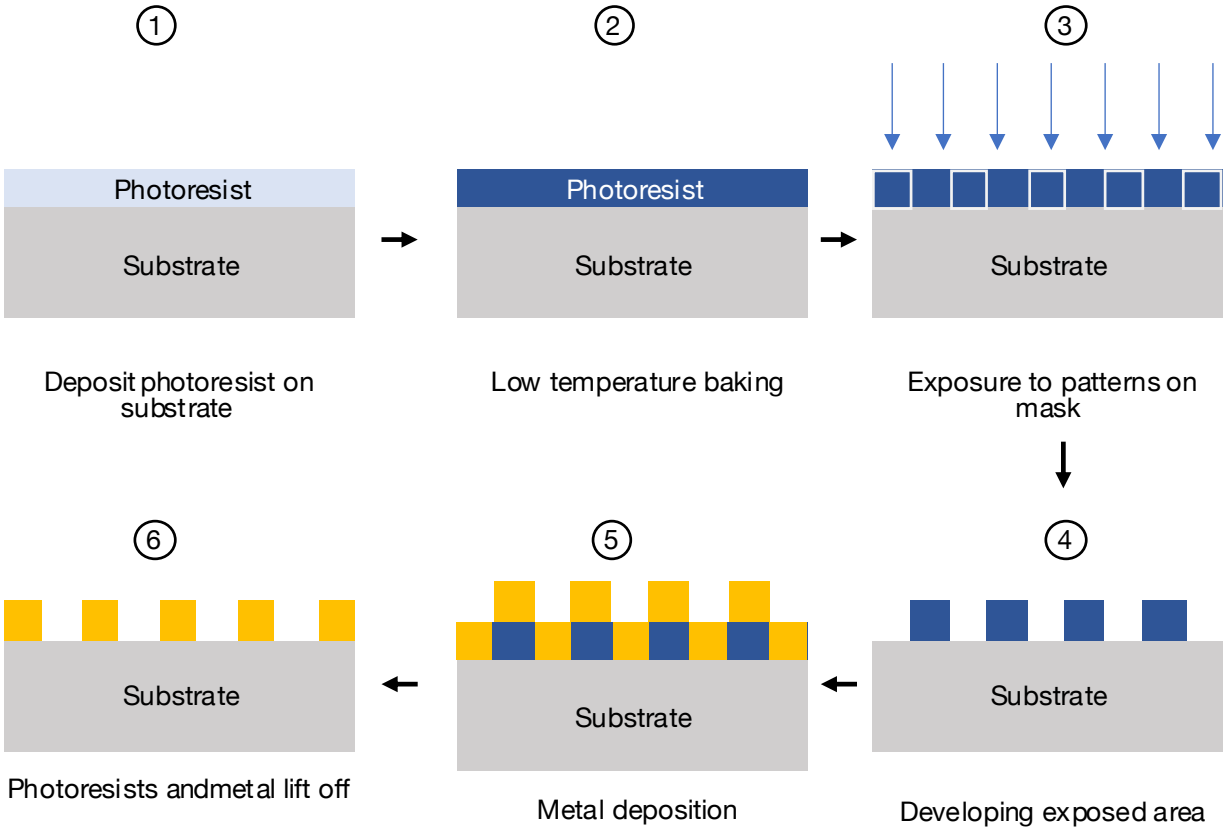

Figure 1.6 Photolithography process

1.7.2 Thermocompression bonding

Thermocompression bonding is frequently used in the microelectronics packaging industry to join two materials together by applying heat and pressure simultaneously[82]. Through this approach, the elevated temperature serves to both soften the metal and enhance the diffusion process, resulting in a reduced pressure requirement. At lower temperatures, a higher pressure is necessary to achieve a high-quality bond.

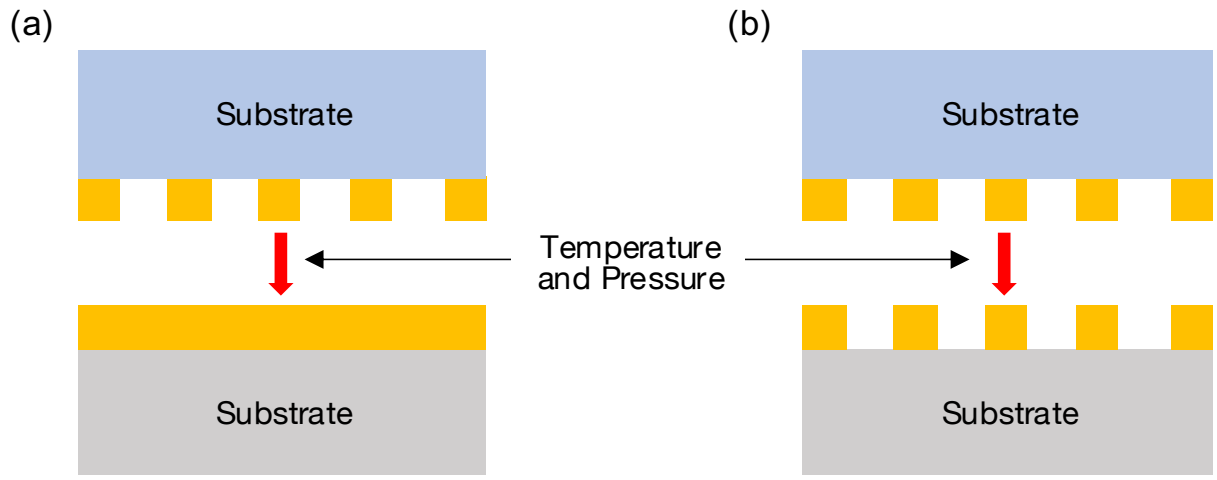

Figure 1.7 Thermocompression bonding. Non-aligned (a) and aligned (b) cold-weld bonding of gold patterns

Common metals utilized in thermocompression bonding include Au, Cu, and Al. One possible reason for poor bonding could be the presence of surface contamination and interdiffusion of materials. Applying appropriate cleaning techniques, like UV-ozone clean, and utilizing interdiffusion materials, such as Ta in Cu-Cu bonding, can potentially address these challenges[83]. Gold is often chosen for thermocompression due to its resistance to oxidation and its malleability. Gold-gold bonding plays a crucial role in many of the studies discussed in the upcoming chapters. This can be separated into aligned and non-aligned bonding. For non-aligned bonding, the surface of one substrate is patterned with gold while the other surface is entirely covered in gold as shown in Figure 1.7a. In the case of aligned bonding, such as in 1.7b, identical gold patterns are created on both materials. Spatial alignment of these complimentary gold patterns can be achieved using tools like a Finetech flip chip bonder, which may place samples with 0.5 μm accuracy.

1.8 Dissertation outline

Chapter 1 provided a fundamental introduction to thermophotovoltaic (TPV) power generation and its application to renewable energy technologies. It established the figure of merit (i.e., power conversion efficiency) and how it is separated into two other meaningful metrics. This chapter also introduces important experimental characterization and fabrication procedures and methods for device modeling, and provides a summary of the state-of-the art performance.

Chapter 2 investigates the use of single-junction InGaAs airbridge TPV cells (ABCs) under varying thermal conditions. In this work, experimental characterization of an InGaAs ABC with varying emitter and cell temperature is used to develop a predictive device model where carrier lifetimes and series resistances are the only fitting parameters. The utility of this model is demonstrated through its use in identifying near-term opportunities for improving performance at elevated power densities, and for designing a thermal management strategy that maximizes overall power output.

Chapter 3 experimentally demonstrates a high-performing single-junction InGaAs(P) air-bridge TPVs with record-high efficiencies, leveraging the learnings and design strategies identified in Chapter 2. The peak and average performance is significantly greater than previously attained in TPVs, promising large improvements in round-trip efficiency and cost per unit stored energy of thermal batteries.

Chapter 4 describes the fabrication of a semitransparent TPV cell consisting of a thin InGaAs/InP heterojunction membrane supported by an infrared-transparent heat-conducting substrate. The cell

demonstrates a novel concept of transmissive spectral control which enables enhanced recuperation of below-bandgap photons by allowing them to transmit through the cell to be absorbed by a secondary emitter. By enabling near-zero photon loss, the semitransparent architecture facilitates high TPV efficiencies at lower emission temperatures.

Chapter 5 investigates an air-bridge tandem TPV cell architecture that enables high spectral management and high output voltage and power. These tandem cells are realized by assembling individual III-V thin-film single-junction TPV cells via a low-temperature cold-welding process between gold grids, facilitating the integration of an air bridge between the sub-cells. In this regard, these cells pave way for high performance across a broad application space by not only ensuring high photon utilization but also enhancing flexibility of bandgap partners toward low-cost materials.

Lastly, Chapter 6 summarizes the major findings of this thesis and discusses potential directions to improve TPV systems.

Chapter 2: Sustaining Efficiency at Elevated Power Densities in InGaAs Airbridge Thermophotovoltaic Cells

This chapter is adapted from Roy-Layinde, B., Burger, T., Fan, D., Lee, B., McSherry, S., Forrest, S. R. & Lenert, A., "Sustaining efficiency at elevated power densities in InGaAs airbridge thermophotovoltaic cells," *Solar Energy Materials and Solar Cells* 236, 111523 (2022).

2.1. Motivation

Despite the potential advantages offered by the airbridge cell (ABC), the performance of InGaAs ABCs currently peaks at relatively low power densities ($\leq$0.3 W/cm^2) and does not account for power losses for thermal management of the cell. Sustaining high efficiency at elevated power densities is important for practical deployment of thermophotovoltaic (TPV) applications, including grid-scale energy storage[15,16,84–86] and distributed generation[12,87,88]. In particular, TPV cells are likely to see elevated emitter temperatures, and therefore elevated power densities, in energy storage applications to maximize their round-trip efficiency[15,16]. Furthermore, effective thermal management of the cells becomes an integral aspect of the overall design under such conditions.

This chapter investigates how elevated power densities affect the performance of InGaAs ABCs and propose strategies to overcome existing limitations. This chapter consists of experiments and models that enable design. We experimentally measure the optical and current-voltage characteristics of the InGaAs ABC while varying the cell temperature from 20ºC to 75ºC, and the SiC emitter temperature from 804ºC to 1177ºC. These data are used to parametrize the device

model that captures various temperature-related effects, including bandgap narrowing and increased recombination. The model, in turn, allows us to analyze how increasing the power density affects the performance of the three relevant cell designs shown in Fig 2.1: (a) a cell with a planar metallic back surface reflector, designated as 'planar', with an OOB reflectance of ~95%, (b) the previously demonstrated InGaAs ABC whose cell architecture is described in[19] and (c) a closer to ideal ABC (termed ABC*) with improved carrier management, corresponding to the longest reported lifetimes in InGaAs[89].

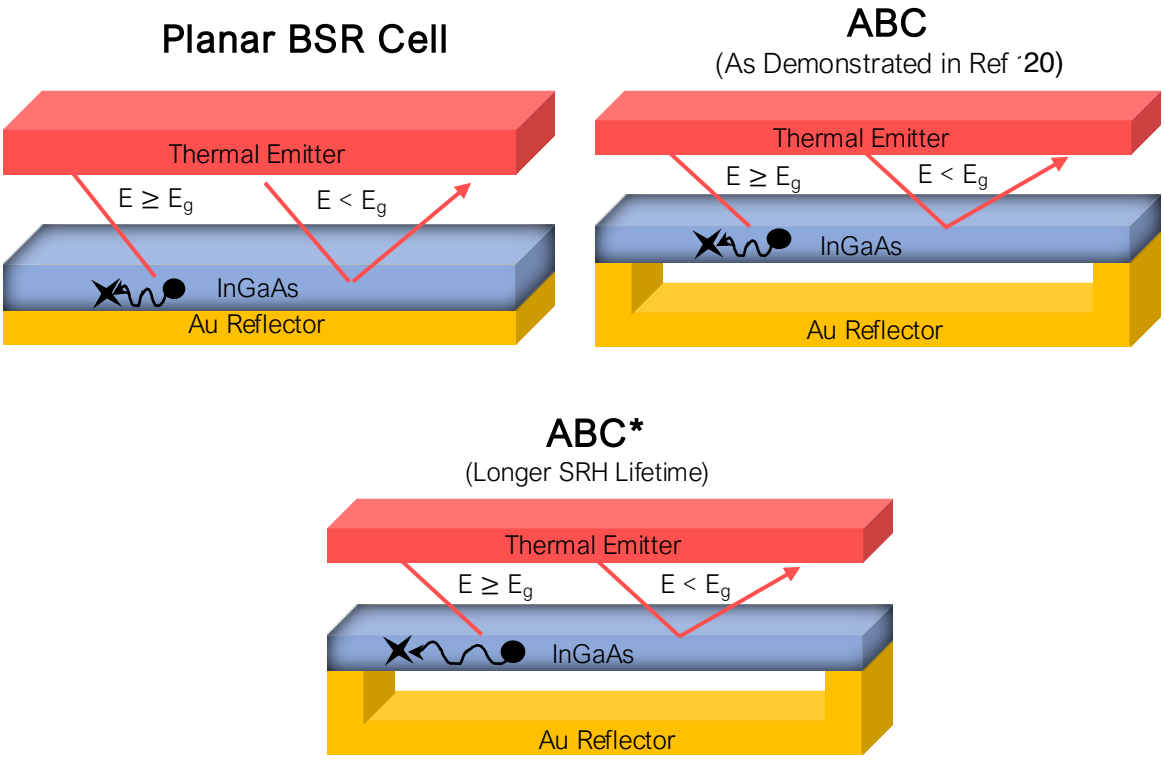

Figure. 2.1 Three TPV configurations at the focus of this chapter: (a) Planar: an InGaAs cell with a planar back mirror exhibiting out-of-band reflectance (R_{oob}) of ~95%, (b) ABC: the InGaAs airbridge cell (ABC) demonstrated in Ref.[57] exhibiting close to 99% R_{oob}, and (c) ABC*: an ABC with better material quality (corresponding to longest reported lifetimes[78]). Arrows in this figure signify the magnitude of carrier lifetime in the cells.

We also consider the power required to cool the cells. These considerations reveal that overall efficiencies exceeding 40% can be achieved at higher power densities (0.5 W/cm^2). Notably, this operating point corresponds to an emitter temperature of ~1070ºC, which is relatively low and consequently may enable the deployment of ABCs in applications such as waste heat harvesting and solar thermal power generation. Overall, this chapter addresses important questions related to using ABCs in energy systems and provides a near-term pathway to achieving high performance.

2.2. TPV characterization

Figures 2.2a and 2.2b show the experimental setup used for current density-voltage (*J-V*) characterization with variable emitter and cell temperatures. *J-V* characteristics are measured using a Keithley 2401 source meter. Emitter and cell temperatures are independently varied in our experiments. Specifically, emitter temperature is regulated from 804ºC to 1177ºC by controlling the electrical input power to the lamp, while the cell temperature is maintained at 20ºC using a chilled water loop. The cell temperature is varied from 20ºC to 75ºC using the water chiller/heater, while the emitter temperature is maintained at 1159ºC. The temperature of the emitter is determined through Fourier transform infrared spectroscopy (FTIR) characterization and fitting of the emission spectrum using our previous procedure[57]. Cell parameters, including dark currents and series resistances, are extracted from *J-V* measurement.

In addition to dark and illuminated *J-V* characterization with varying cell temperature, spectral reflectance of the ABC versus cell temperature is characterized at an incidence angle of 30º over a spectral region from 0.3 eV to 1.35 eV using an Agilent Cary 620 FTIR microscope and a heated

stage. Absorption data are supplemented outside the specified range (< 0.3 eV and > 1.35 eV) by simulated results based on transfer matrix modeling.

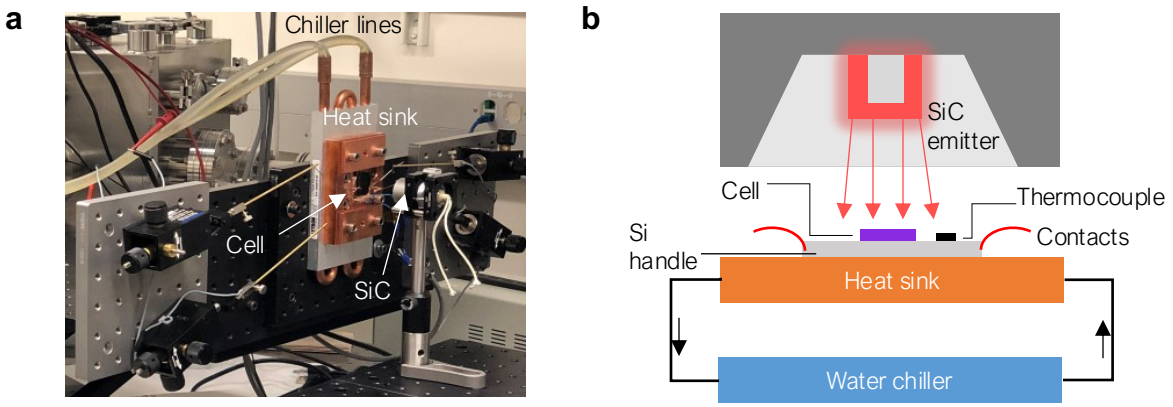

Figure. 2.2 Experimental characterization of temperature dependence. a) Image and b) schematic of the temperature dependence measurement setup. A SiC globar emitter is used as the source of thermal radiation. The water chiller is used to cool and regulate the cell's temperature.

2.3. Model validation

The model used here is described in chapter 1.6 which is based on the double-diode model. To determine τ_1, τ_2 and R_s, the model is fit to (i.e., trained on) illuminated *J-V* measurements at a specific operation condition (T_h = 1182ºC, T_c = 50ºC) following a previous procedure[57], resulting in τ_1 =13 ns, τ_2 = 70 ns and R_s = 30 mΩ.cm^2. The carrier lifetimes are consistent with previous studies[48], although they fall short of the best-reported values of 47 µs[48]. The accuracy of the model is then evaluated by comparing predicted *J-V* to measured data across the full range of experimental conditions. Experimental *J-V* characteristics of the ABC are shown alongside the model at varying cell temperatures in Fig. 3a. The root mean square error (RMSE) of the predictions for open-circuit voltage (V_{oc}), maximum power density (P_{mpp}) and short-circuit current density (J_{sc}) with varying cell temperature are 1.5%, 4.8% and 4.2%, respectively. Fig. 2.3b shows

J-V data at three emitter temperatures while maintaining the cell at 20ºC. The model predicts V_{oc}, P_{mpp} and J_{sc} with varying emitter temperatures within 0.65%, 1.7% and 0.08% RMSE, respectively. Overall, the error is less than 5% suggesting that the assumptions of temperature-independent carrier lifetime and series resistance are reasonable.

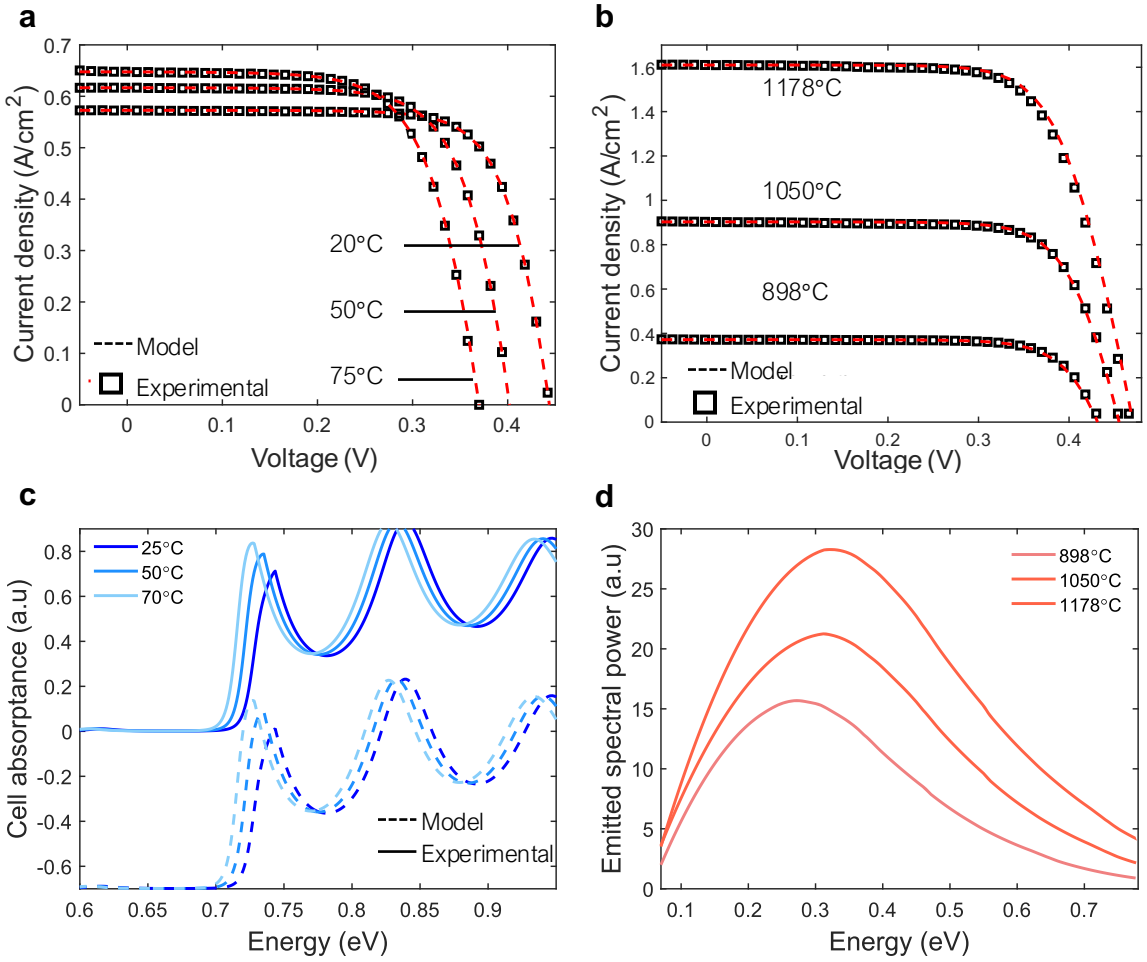

Figure. 2.3 Model training and validation. a) Current density (J) vs voltage (V) curves at three representative ABC temperatures (20ºC, 45ºC, 75ºC) and a constant emitter temperature of 1159ºC. b) ABC J-V data at three representative emitter temperatures (898ºC, 1050ºC, 1177ºC) and a constant cell temperature of 20ºC. c) Spectral absorptance of the ABC at three representative cell temperatures. d) Spectral emission from the SiC emitter at three representative emitter temperatures.

A decrease in the open-circuit voltage is observed with increasing cell temperature due to increased recombination. The decline in voltage is largely explained by the increasing intrinsic carrier concentration, which increases the rate of non-radiative recombination in the cell. In addition to lower voltage, we observe an increase in photocurrent density with temperature due to bandgap narrowing, as shown in Fig. 2.3c. The first absorption peak at energy higher than the bandgap, which is associated with an optical cavity resonance (within the cell) centered around ~0.73 eV, increases because of bandgap narrowing. We also observe a redshift (~2.14 $\times 10^{-2}$ %/K) of the optical cavity resonance, consistent with a change in the refractive index of GaAs and InAs with temperature coefficients on the order of 10^{-2} %/K[90,91]. With increasing emitter temperature, there is an increase in the photocurrent density as more in-band photons are emitted (Fig. 2.3d). This effect is described by Planck's equation and the experimental effective emissivity of the thermal emitter. Accompanying this is a logarithmic rise in open-circuit voltage.

2.4 Figures of Merit

The figure of merit used here is the conversion efficiency, defined as the ratio of generated power density (P_{mpp}) to the radiative heat flux absorbed by the cell (Q_{abs})[63]. Conversion efficiency may be further decoupled into metrics specific to the quality of spectral and charge carrier management according to [64]:

$$\eta = \frac{P_{mpp}}{Q_{abs}} = (SE \cdot IQE)(VF)(FF) = \left(\frac{J_{sc}V_g}{Q_{abs}}\right)\left(\frac{V_{oc}}{V_g}\right)\left(\frac{P_{mpp}}{J_{sc}V_{oc}}\right). \quad (2.1)$$

Here, spectral management is defined by the product of spectral efficiency (SE) and the internal quantum efficiency (IQE); it describes how well the absorbed power is converted into the short

circuit current multiplied by the bandgap voltage (V_g). Charge carrier management is described by the voltage factor (VF) and the fill factor (FF). Here, the voltage factor is the ratio of the open-circuit voltage to the bandgap voltage. The fill factor (last term on right in Eq. 2.1) largely reflects loss to series resistance and shunting.

2.5 Understanding and Overcoming Performance Loss at High Power Densities

Using the validated model described in chapter 1.6, we focus on understanding how the three different systems behave at high power densities. Figure 2.4a shows the predicted efficiency versus power density of the InGaAs ABC compared to the planar cell and the higher performance ABC*. The increasing power densities were modeled with increasing emitter temperatures from ~650ºC to ~1450ºC as shown in Figure 2.4b. Even though ABC* can achieve better efficiencies at higher power densities relative to the others, we see a similar trend where the efficiency plateaus and begins to drop with increasing the power density.

To better understand the limitations of the existing ABC, the model is used to provide a breakdown of the loss pathways following photon absorption as a function of emitter temperature. As shown in Fig. 2.4c, non-radiative recombination is the dominant loss pathway, accounting for 36% of the power loss. We find that non-radiative recombination rate is largely controlled by defect mediated (SRH) recombination, and only <1% by Auger recombination. The other loss pathways include absorption of OOB photons and thermalization of high energy photons. Although their overall fraction remains relatively constant at ~30% of the total, thermalization overtakes OOB-loss as emitter temperature increases due to the blue shift in the blackbody distribution. Ohmic losses also constitute an important pathway for energy loss, particularly at high emitter temperatures because

they scale quadratically with current density. We note this analysis is performed for a constant F_v = 0.75, and that operation at higher view factors will increase the photocurrent density produced and lead to higher Ohmic losses.

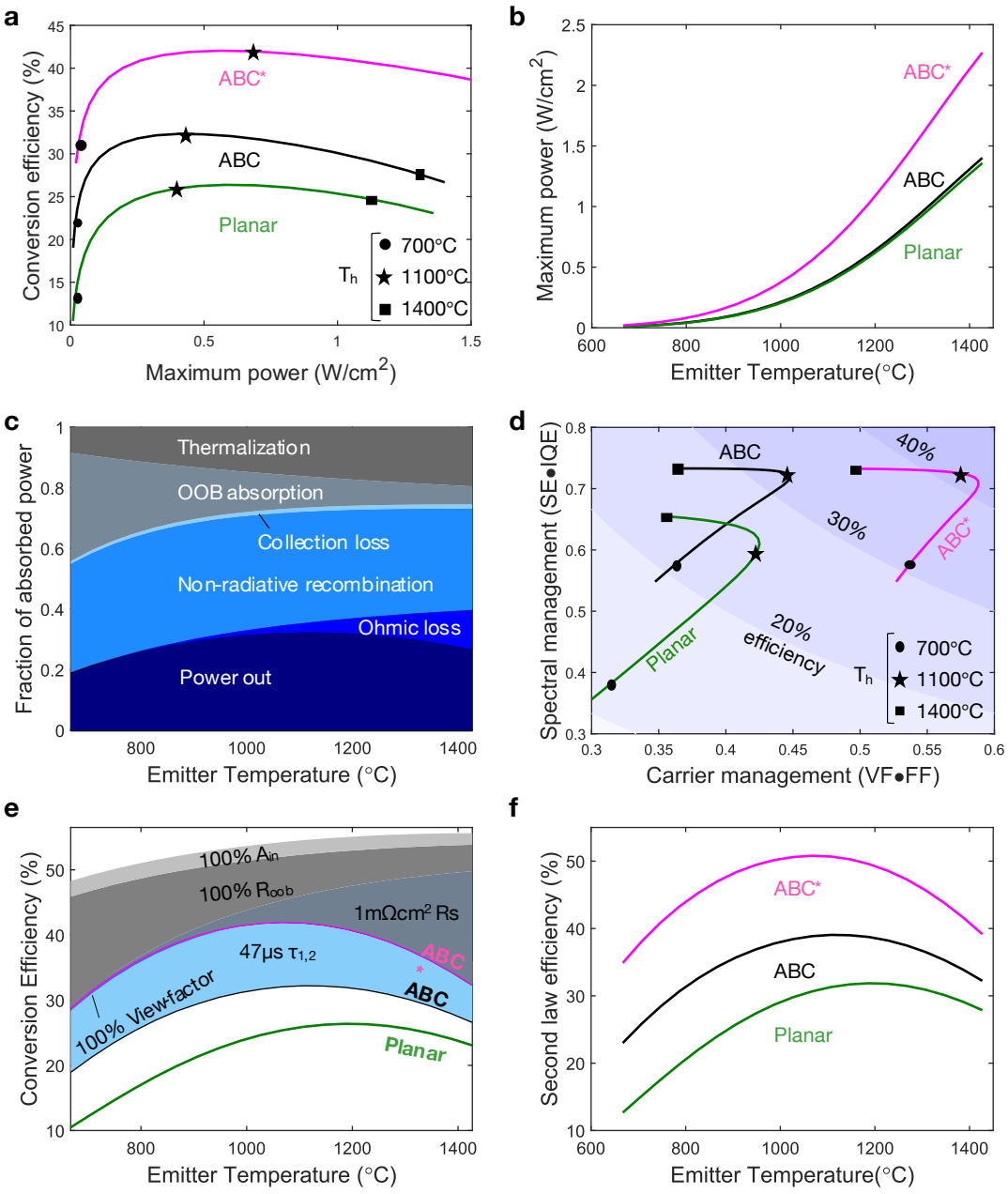

Figure. 2.4 Current ABC performance and near-term improvements. (a) Predicted efficiency versus power for ABC, ABC* and planar configurations. The circle, star and square markers denote T_h = 700ºC, 1100ºC and 1400ºC respectively. **(b)** Power produced for the three different

systems as a function of emitter temperatures. **(c)** Loss pathways in ABC as a function of emitter temperature. **(d)** Efficiency plots for variable emitter temperature as a function of carrier and spectral management. Black, pink, and green solid curves represent simulated efficiency for the ABC, ABC*, and planar cell, respectively. (**e)** Efficiency projection with improved spectral and carrier management. 100% A_{in} and 100% R_{oob} represents total absorption and reflection of in-band and out-of-band photons respectively. $1m\Omega \cdot cm^2$ represents an improve in series resistance from the current $30m\Omega \cdot cm^2$. Also, 47μs signifies improvement from ABC to ABC*. (**f)** Second law efficiency (to Carnot limit) for the three different configurations at varying emitter temperatures.

The above losses can be categorized as either affecting spectral management (e.g., OOB loss and thermalization) or carrier management (e.g., recombination and Ohmic losses). The effects of increasing emitter temperature on spectral and carrier management of the ABC are depicted by the black curve in Fig. 2.4d. Remarkably, an increase of the emitter temperature from 667 to 1427ºC changes the spectral management efficiency of the ABC by only ~15%, from 58 to 73%. The relative insensitivity of the ABC to emitter temperature is due to its very high reflectance (~98.5%) which limits OOB loss from becoming dominant. In contrast, the spectral efficiency of the planar cell changes from 39% to 65% over the same emitter temperature range. The flattening of the ABC curve after reaching peak efficiency at ~1080ºC indicates that a further emitter temperature increase has small effects on spectral management. Carrier management metrics, in contrast, are observed to sharply drop with increasing T_h beyond that point, largely due to Ohmic losses.

To describe potential near-term performance improvements that may be achieved through the use of improved quality material, we model the performance of the ABC* cell, which exhibits the spectral properties of the ABC, but with the longest carrier reported for InGaAs (47μs)[78]. This results in an increased V_{oc}, increasing absolute efficiency over the entire emitter temperature range. Further, the carrier management metrics of the ABC* exhibit relative insensitivity to changes in

emitter temperature, as Ohmic losses represent a smaller fraction of the output voltage. Notably, the efficiency of the ABC* peaks above 40% with an emitter temperature of ~1050ºC.

To reach efficiencies exceeding 50%, additional advances are necessary, including reducing series resistance, increasing OOB reflectance and IB absorption. Figure 2.4e shows a projection of conversion efficiency for various cell improvements as a function of variable T_h. Moving from ABC to ABC* is considered a near-term improvement, which yields a ~10% absolute increase in efficiency. Design of a TPV cavity with emitter-cell view factor approaching unity maximizes cell illumination and photocurrent, further increasing efficiency by ~0.6%. Beyond near-term improvements[92], decreasing cell series resistance from $30 m\Omega \cdot cm^2$ to $1 m\Omega \cdot cm^2$ would increase the conversion efficiency by ~5% absolute at 1127ºC and enable operation at higher emitter temperatures and power densities. Optimized grids and selective contacts[93] may yield such reductions. Another ~5-15% absolute efficiency gain is observed in the limit of boosting the OOB reflectance from 98.5% to 100%. Lastly, improving the absorption of in-band photons from 62% to ~100% using anti-reflective coatings and/or textured surfaces increases the output power, enabling another ~2% absolute efficiency increase. Overall, these cell improvements would enable >50% conversion efficiency at moderate emitter temperatures (i.e., <1000ºC), while also sustaining high efficiency at the elevated power densities associated with high emitter temperatures. In Figure 2.4f, we compare the second law efficiencies for each system as a function of emitter temperature. For example, the ABC cell currently operates at 39% of the Carnot limit at an optimal temperature of 1107°C. As highlighted by the difference in second law efficiency between the ABC and Planar systems, increasing R_{oob} leads to significantly less entropy generation

at lower temperatures. This comparison also shows that all three systems considered in this work still have significant room for improvement.

2.6 Thermal management

Active thermal management is needed at high power densities to maximize overall power output and mitigate temperature-related degradation of device lifetime[94–96]. An understanding of how heating affects efficiency allows us to calculate the heat load for each TPV system, and in turn, predict the amount of power consumed by the cooling system. The understanding is provided by the experimentally validated model that captures the effects of cell temperature on various optical and carrier-related mechanisms.

2.6.1 Temperature coefficients

Table 2.1 illustrates the effects of temperature on key cell performance characteristics. While temperature effects are well documented for solar PV cells[97–101], they are not as well understood for TPVs. A complicating factor is that these coefficients depend on the temperature of the emitter. The data form Table 2.1 were calculated at a constant emitter temperature (T_h = 1160°C). These results are represented using best-fit linear temperature coefficients (normalized to 20°C), where the temperature coefficient of a given parameter (G) is given by $\beta_G = 1/G(20^o\mathrm{C}) \cdot (G(T_c) - G(20^o\mathrm{C}))/(T_c - 20^o\mathrm{C})$. We observe that the voltage factor decrease with increasing T_c has the largest effect on efficiency ($\beta_{VF} = -0.324\%/\mathrm{K}$). In contrast, spectral management ($SE \cdot IQE$) has a slightly positive coefficient with increasing cell temperature, which is attributed to increasing photocurrent density due to bandgap narrowing. Furthermore, a comparison of the temperature

coefficients for the three systems reveals their respective strengths and weaknesses. The spectral efficiency of the planar cell benefits most from increased cell temperature (and its associated bandgap narrowing) due to its relatively high OOB absorption. Meanwhile, carrier management in ABC* is least sensitive to increases in cell temperature because of its relatively high V_{oc}.

Table 2.1 Temperature coefficients of the ABC, ABC*, and planar cell at constant emitter temperature of 1160°C.

Cell	$SE.IQE$ ($\%/K$)	V_{oc} $(\%/K)$	VF $(\%/K)$	J_{sc} $(\%/K)$	FF $(\%/K)$	η $(\%/K)$
ABC	0.012	-0.367	-0.324	0.07	-0.177	-0.461
Planar	0.152	-0.359	-0.317	0.21	-0.179	-0.356
ABC*	0.012	-0.234	-0.188	0.07	-0.11	-0.277

Figure 2.5a illustrates the heat load (Q_c) required to maintain the three cells at a fixed cell temperature of 20°C, where Q_c is given by: $Q_c = Q_{abs} - P_{mpp} = Q_{abs}(1 - \eta)$. We modify the varying power density by varying the emitter temperature. The ABC has a lower heat load than the planar cell owing to its relatively low OOB absorption and long carrier lifetime. The longer lifetime has two effects, it decreases the amount of (1) heat generated through carrier recombination, and (2) Joule heating for a given power output because of its relatively high voltage.

2.6.2 Air-cooling design

Heat dissipated in the cell (Q_c) is removed by forced air, according to:

$$Q_c * A_{array} = h \cdot n_{ch} \cdot \pi \cdot D \cdot L \cdot (T_{wall} - T_{air}) \quad (2.2)$$

where A_{array} is the area of the cell array (10 cm x 10 cm), h is the internal convection heat transfer coefficient, L is the length of channel (10 cm), D is the diameter of channel, n_{ch} is the number of channels. The heat transfer coefficient is given by[102]:

$$h = \frac{Nu \cdot k_{air}}{D_H} \tag{2.3}$$

where Nu is the Nusselt number, D_H is the hydraulic diameter, and k_{air} is the thermal conductivity of air. The Nusselt number is calculated from the Reynolds number Re and the Prandtl number Pr (which is 0.7 for air), according to:

$$Nu = 0.023 \cdot Re^{0.8} Pr^{0.4} \tag{2.4}$$

$$Re = \frac{\rho \cdot v \cdot D_H}{\mu} \tag{2.5}$$

Here, ρ, v and μ represents the fluid density, fluid velocity and dynamic viscosity respectively. The pumping power, P_{pump}, is given by the following set of equations:

$$P_{pump} = \frac{m \cdot \Delta P}{\rho \cdot \eta_{fan} \cdot \eta_{motor}} \tag{2.6}$$

$$\Delta P = \rho \cdot g \cdot \mathrm{H} \tag{2.7}$$

$$H = \frac{v^2 . f}{2g} \left(\frac{L}{D_H} \right) \tag{2.8}$$

$$f = 0.316 \cdot Re^{-0.25} \tag{2.9}$$

where m is the fluid flow rate, ΔP is the pressure drop, f is the friction factor, g is the gravitational acceleration, H is the head loss, and the product of the fan efficiency η_{fan} and motor efficiency η_{motor} was assumed to be 0.8[102]. From this model, the internal convection resistance of the air-cooled channels represents ~98% of the thermal resistance. Thus, the conductive resistance through the thin cell, including the air gap, and the copper heat sink are negligible.

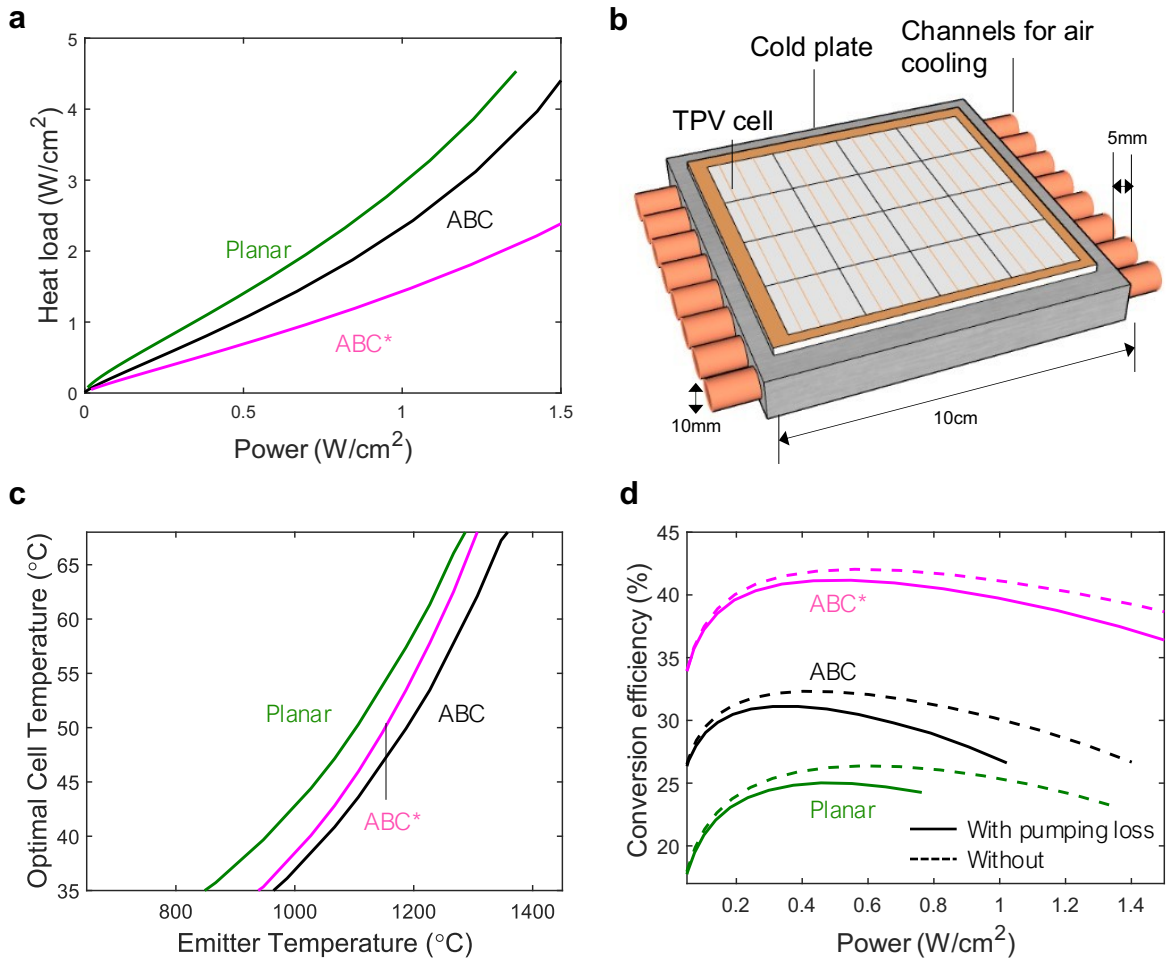

Figure. 2.5 Thermal management of ABCs. (a) Heat load as a function of power produced for the three configurations. **(b)** Schematic showing envisioned air-cooled thermal management design. **(c)** Optimal cell temperatures as a function of emitter temperature. (**d**) Efficiency as a function of power produced when air-cooling is considered.

With the temperature dependence and heat load described above, we design an active cooling system in which a portion of generated power is diverted and used to circulate the coolant. The temperature of the cell and the emitter are coupled through the heat load and the effective heat transfer coefficient between the cell and coolant. For thermal management, we consider an array of parallel channels embedded in a metal block that supports a 10 cm x 10 cm cell array as shown in Fig. 2.5b. An internal convection model is used to describe the heat transfer and estimate the

power requirements for running a fan to circulate air through the channels (see above). Figure 2.5c shows the optimal cell temperature as a function of emitter temperature. For example, an ABC* cell at 40ºC maximizes the efficiency for an emitter temperature of 1027ºC. In this scenario, 2.8% of the cell output power is consumed by the fan. From this analysis, we observe that the optimal cell temperatures of the ABC are generally lower compared to both the planar and ABC* design.

Figure 2.5d shows how cell heating and cooling power affect the efficiency of the overall system. The dashed lines show the power produced at a constant cell temperature of 20ºC without accounting for cooling (same as Fig. 2.4a). The solid lines show the net power produced after diverting some of the generated power to keep the cells at the optimal temperatures in Fig. 2.4c. Notably, thermal effects are significant at high power densities in all three systems. Furthermore, the optimal operating conditions generally shift toward lower power densities when cooling is considered. For example, before cooling, ABC and planar have optimal efficiencies at emitter temperatures of 1107ºC and 1187ºC, respectively. After considering cooling, these temperatures are reduced to 1067ºC and 1147ºC respectively. Despite the thermal penalties, the air-cooled ABC* system is still predicted to achieve a high-power density (0.5 W/cm^2) with >40% efficiency. Beyond air-cooled parallel channels, further improvements to the thermal management design are likely to enable better performance. These include liquid coolants, phase-change heat transfer[103–105], nanostructured surfaces[106,107], and microchannel heat sinks[108,109].

2.7 Conclusions

This chapter provides a deeper understanding of how losses in recently demonstrated InGaAs airbridge cells (ABCs) depend on emitter and cell temperature, which is relevant for use of ABCs

in practical energy systems at elevated power densities. We find that the efficiency is primarily limited by defect-mediated recombination and series resistance. Realizing improved material quality in InGaAs ABCs, addresses both challenges and enables better performance at higher power densities, including efficiencies exceeding 40% at 0.5 W/m^2. Notably, this efficiency takes into consideration the power needed to cool the cells. The work provides additional design guidelines for improving TPV performance including how the optimal emitter temperature decreases when thermal management is considered. For the InGaAs ABC, the optimal emitter temperature is around 1000ºC which is a relatively low temperature for TPV applications. This highlights a promising feature of the ABC design, which is that lowering the emitter temperature reduces the amount of power needed to cool the cells without incurring large spectral management penalties.

Chapter 3: High Efficiency Air Bridge Thermophotovoltaic Cells

This chapter is adapted from Roy-Layinde, B., Lim, J., Arneson, C., Forrest, S. R. & Lenert, A., "High efficiency airbridge thermophotovoltaic cells," under revision.

3.1 Introduction

Recent progress in TPVs has led to efficiencies as high as 41%, albeit using very high emitter temperatures[4,28]. For example, LaPotin *et al.* demonstrated an efficiency of 41% with a III-V semiconductor tandem device using a 2400°C halogen bulb, while Tervo *et al.* reported an efficiency of 39% with a single-junction cell using a 1850°C protected graphite heater. The ultrahigh temperatures (>1800°C) needed to maximize performance in these systems hinders the deployment of TPVs due to challenges in finding stable emitter materials and isolating the cells from contamination[7,64,110,111]. Recent materials screening efforts have identified promising emitters for ultrahigh temperature applications[112,113], however, experiments have revealed lower stability than predicted[113,114]. Furthermore, system-level mitigation strategies to facilitate the use of intrinsically *unstable* emitters at such conditions have not been experimentally verified.

3.2 Need for high performance at stable emitter temperatures

In this context, there is a substantial advantage in engineering TPV cells to maximize performance at emitter temperatures compatible with a wide array of stable materials. Unfortunately, the highest TPV efficiencies reported using emitter temperatures at < 1600°C are currently limited to 37%[19,115–118]. In this chapter, we demonstrate single junction TPV efficiencies approaching 45%

at 1500°C using cells based on InGaAs(P) alloys lattice matched to InP substrates. The high performance is enabled by the recently demonstrated air-bridge back surface reflector with near-unity reflectance of out-of-band photons[19,117,119]. The result, to our knowledge, represents a record-high TPV efficiency regardless of emitter temperature. Moreover, the use of a single junction cell and substantially lower emitter temperatures than in[4,118] should facilitate the widespread implementation of the technology. This chapter also highlights the transferability of the air-bridge architecture with >98% reflectance of out-of-band photons (R_{out}) to a range of semiconductor materials.

3.3 Pairing air-bridge architecture with wider bandgap materials

Conventional TPV cells exhibit rigid trade-offs between the ability to harness the incident spectrum, captured by the product of the spectral efficiency (*SE*) and the internal quantum efficiency (*IQE*), and the ability to generate a high output voltage, whose figure of merit is the product of the fill factor (*FF*) and the voltage factor (*VF*) (i.e., the ratio of the open-circuit voltage to the bandgap). To investigate these effects in air-bridge cells and optimize performance at the target emitter temperatures, we selected the following three materials to implement our cell design: 0.74 eV ($In_{0.53}Ga_{0.47}As$), 0.9 eV ($In_{0.69}Ga_{0.31}As_{0.67}P_{0.33}$) and 1.1 eV ($In_{0.83}Ga_{0.17}As_{0.37}P_{0.63}$). The materials are commercially grown by metalorganic chemical vapor deposition (MOCVD) in the $In_{1-x}Ga_xAs_{1-y}P_y$ (InGaAsP) material system lattice-matched to (100) InP substrates. We note that the high power density of TPVs, which is 50-500X that of solar PV, justifies the use of high quality III-V cells and their corresponding substrates. Also, photolithography typically accounts for a small fraction of the overall cost relative to the growth substrate[120,121].

3.3.1 Material growth

The heterostructure is epitaxially grown by metalorganic chemical vapor deposition on a 600μm thick (100) Zn-doped InP substrate (Microlink Devices Inc., Niles, IL, USA). The epitaxial film consists of a 500nm thick Zn-doped (1×10^{17} cm^{-3}) $In_{0.53}Ga_{0.47}As$ (InGaAs) etch stop layer, 100nm thick Zn-doped (1×10^{17} cm^{-3}) InP etch stop layer, 100nm thick Zn-doped (4×10^{18} cm^{-3}) $In_{0.53}Ga_{0.47}As$ (InGaAs) front contact layer, 300nm Zn-doped (4×10^{18} cm^{-3}) InP front window layer, Te-doped (1×10^{17} cm^{-3}) absorber layer , 50 nm thick Te-doped (3×10^{18} cm^{-3}) InP rear window layer, 1μm thick Te-doped (1×10^{17} cm^{-3}) InP buffer layer, and 100nm thick Te-doped (1×10^{18} cm^{-3}) InGaAs rear contact layer. The 1μm thick Te-doped InP layer serves as an additional buffer layer to strengthen the mechanical structure and minimizing buckling of the air bridge membrane[119]. The thicknesses of the absorber layers are 2μm for 0.74eV ($In_{0.53}Ga_{0.47}As$), 2μm for 0.9 eV ($In_{0.69}Ga_{0.31}As_{0.67}P_{0.33}$), and 1.5 μm thick for 1.1 eV ($In_{0.83}Ga_{0.17}As_{0.37}P_{0.63}$), respectively.

3.3.2 Device fabrication

The epitaxial samples and a Si wafer are plasma cleaned to remove residual organic material and then soaked in buffered HF for 90 seconds to remove the native surface oxides. All layers are photolithographically patterned with SPR 220 3.0 photoresist (Kayaku Advanced Material Inc., Westborough, MA, USA.). The rear contact grids (10nm Ti / 550nm Au) are deposited by electron-beam evaporation in a chamber with a base pressure of $4x10^{-6}$ torr. The devices are 2 mm squares with 20 μm wide on a 60 μm pitch conducting grid lines. The sample is soaked in 1:1:8 H_3PO_4:H_2O_2:H_2O for 20s to remove the 100 nm thick InGaAs rear contact layer between the grid lines. The Au-patterned epitaxial membranes are transferred to a Au-coated Si wafer via cold-weld

bonding using an EVG 510 wafer bonder for 10 minutes under heat (150°C) and pressure (8 MPa). This temperature is precisely designed to maximize material integrity by preventing undesirable Au-Si intermixing, preserve device characteristics (InP sublimation occurs at temperatures above 200°C), reduce thermal stress, and prevent any unwanted alloy formation. The InP substrates are selectively removed by wet etching by soaking in HCl:H_2O (1:1) for 12 h. This method is compatible with non-destructive epitaxial lift-off used to reduce cost (11). Alternating soaks in InGaAs (1:1:8 H_3PO_4:H_2O_2:H_2O) and InP (1:1 HCl:H2O) solutions are used to etch the device mesas. The front contact grids (10 nm Pt / 10 nm Ti / 15 nm Pt / 5000 nm Au) are deposited by electron-beam deposition. Finally, the sample is soaked for 20 s in a 1:1:8 H_3PO_4:H_2O_2:H_2O solution to remove the 100nm thick InGaAs front contact between the grid lines.

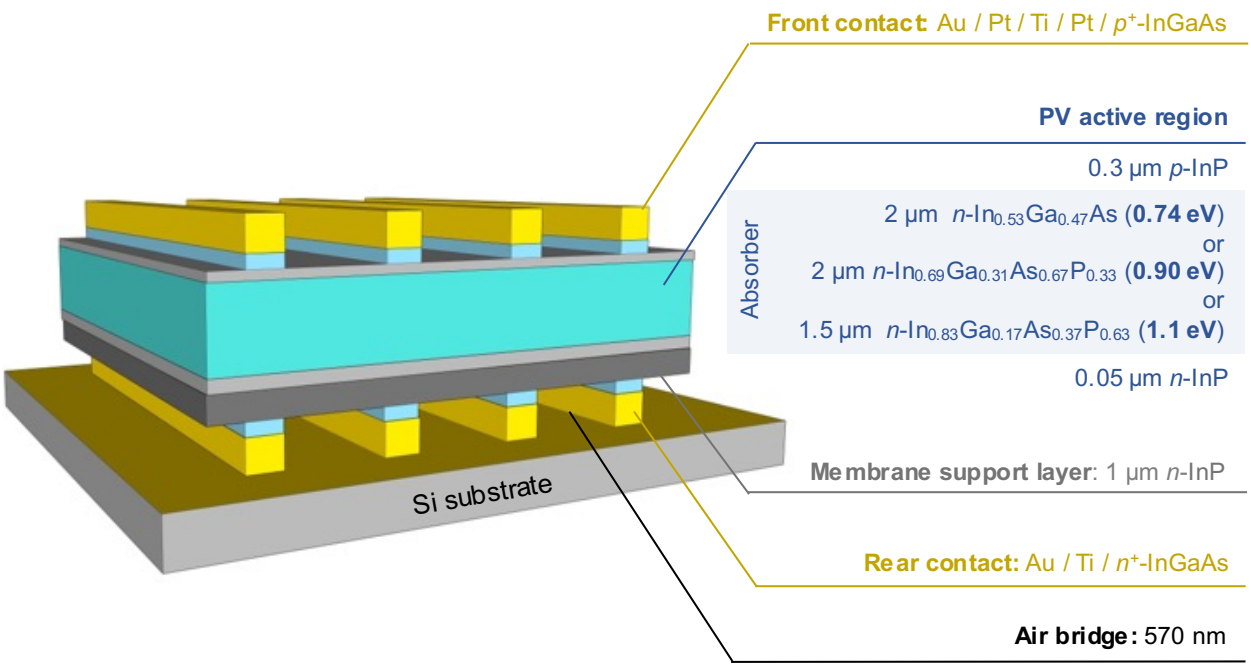

Figure 3.1 High performance cell design in three absorber materials. The absorber layer is 2 µm thick for both the 0.74 eV ($In_{0.53}Ga_{0.47}As$) and the 0.9 eV cells ($In_{0.69}Ga_{0.31}As_{0.67}P_{0.33}$), and 1.5 µm thick for the 1.1 eV ($In_{0.83}Ga_{0.17}As_{0.37}P_{0.63}$) cell. A 570 nm thick air-bridge layer is situated between the active layers of the InP-based PV cell and the rear Au mirror to enhance backside reflectance and the recuperation of out-of-band photons.

3.3.3 Air-bridge device architecture

The cell architecture in Figure 3.1 maximizes both its optical and electrical performance (see *Supporting Information* for details on device structures and fabrication)[122]. The design features a 570 nm thick air gap below the active region that minimizes absorption at the metal electrode[19,117], thus providing near unity out-of-band reflectance. Further, parasitic free carrier absorption (14) of incident radiation is reduced by positioning metal grids with high infrared reflectance (99%) directly over the relatively high-doped contact regions. The combination of a nanoscale air layer and a relatively high coverage of conductive rear electrodes ensures that the air-bridge thermal resistance is small compared to that of the Si substrate[19]. Additionally, we introduce a membrane support layer to minimize the impact of buckling on the free-standing semiconductor membrane[119], ensuring a single cavity mode between the air-bridge and the semiconductor membrane.

3.3.4 Control device

We also made TPV cells without the air bridge, also known as cells with planar Au back surface reflectors (Au-BSR), for all three bandgap materials as shown in Figure 3.2a. These cells are the same size as the air-bridge cells (Figure 3.2b). Figure 3.2c compares the surface profile of the air-bridge cells to the Au-BSR cells, highlighting the flatness of the air-bridge architecture.

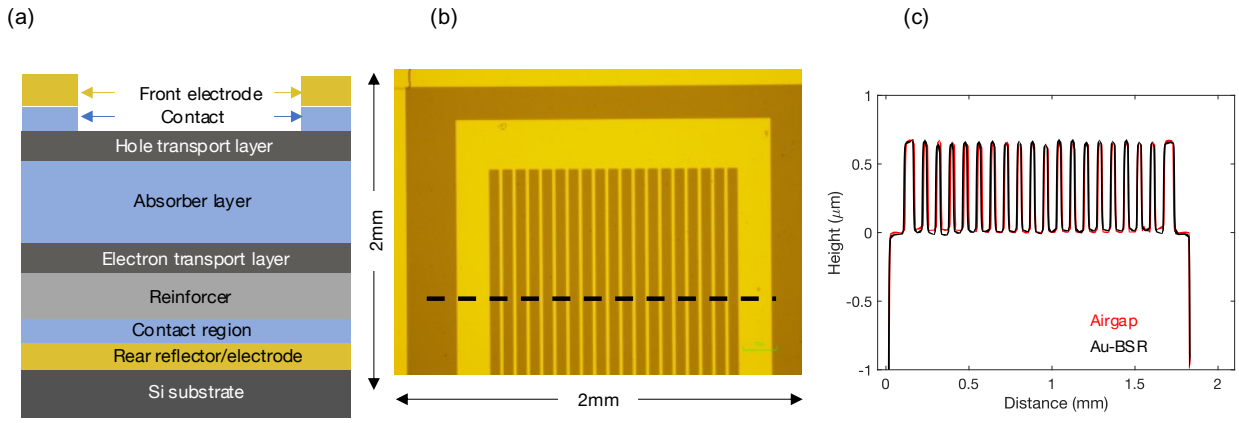

Figure 3.2 Control device. (a) Schematic of the Au-BSR structure. (b) Front surface image of the cell. (c) Surface profilometer scan of the Au-BSR and air-bridge cells highlighting its flatness.

3.4 Spectral management characterization

3.4.1 Experimental optical characterization

The reflectance of each cell is measured using a Cary 670-IR spectrometer equipped with a Cary 620 IR microscope (Agilent Technologies, CA). Near- and mid- IR measurements are taken with quartz and KBr beam splitters, respectively, and a cooled MCT detector. The measurement covers incidence angles ranging from 18 to 41˚. Thermal emission spectra for the SiC emitters (SLS203L, Thorlabs, NJ; White-Rodgers 767A-377) are calibrated to a real blackbody source (IR-564, Infrared Systems Development Corp., FL) whose blackbody emissivity is > 0.99 according to manufacturer specifications. Emission from SiC is collimated by an off-axis parabolic mirror and directed through the external port of the Nicolet iS50 FTIR spectrometer. Linear interpolation removes H_2O and CO_2 absorption in the spectral ranges 2.5-2.8 μm and 5-7.6 μm. The emission spectra are compared to a blackbody curve, resulting in an average thermal emittance of 0.96. Figure 3.3a shows the measured spectral absorptance of the three air-bridge cells at near-normal incidence along with the 1500°C blackbody spectrum. The spectra show features that are

characteristic of free carrier absorption (<0.3 eV), Fabry-Perot cavity modes, and inter-band transitions. When weighted to the blackbody spectrum, the FTIR measurements yield out-of-band reflectances of R_{out} = 97.4 ± 0.1%, 98.3 ± 0.1% and 98.6 ± 0.2% for the 0.74 eV, 0.9 eV and 1.1 eV bandgap InGaAsP cells, respectively. These results represent a 3% to 6% absolute increase in R_{out} compared to control cells without the air bridge (Au-BSR) as shown in Figure 3.3b. The slight increase in R_{out} with increasing bandgap is due to the diminished impact of free carrier absorption when integrating over a wider spectrum. External quantum efficiencies (EQE) for the three airgap cells are also shown in Figure 3.3c. Here we calculate the internal quantum efficiency (IQE) as the ratio of the EQE to the measured absorptance by the cells.

Figure 3.3d shows the spectral management efficiency (SE·IQE) of the air-bridge cells. The three devices (0.74, 0.9 and 1.1 eV) exhibit maximum SE·IQE = 71.3%, 73.3%, and 64.1%, respectively, for emitter temperatures ranging from 900 to 1600ºC. The large fraction of out-of-band radiation in the 1.1 eV cell explains the relatively low spectral efficiency compared to the other cells. Remarkably, the 0.9 eV cell outperforms the already high spectral efficiency of the 0.74 eV cell at temperatures as low as 1200°C. Overall, these results demonstrate that the air-bridge design significantly enhances out-of-band reflectance in a range of thin-film cells, enabling spectral management efficiencies up to 73%.

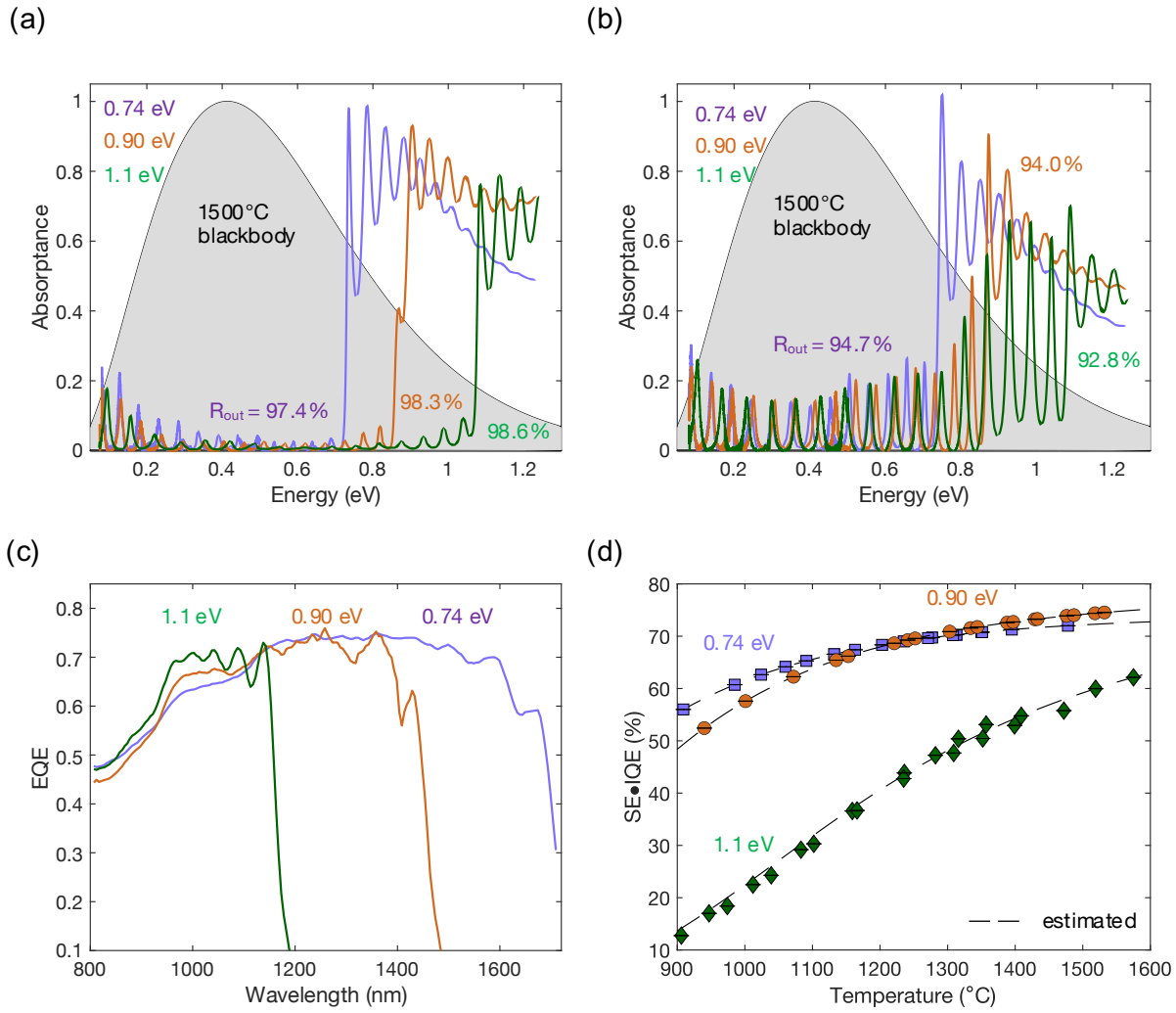

Figure 3.3 Optical characterization of the air-bridge cells. (a) Experimental absorptance (i.e., 1 – reflectance) measured by FTIR for the 0.74 eV (purple), 0.9 eV (orange) and 1.1 eV (green) air-bridge cells. (b) a) Absorptance measured by FTIR for the three bandgap cells without air-bridge called Au-BSR (c) EQE measurements for the three air-bridge devices. (d) Spectral management efficiency (SE·IQE) for the three cells *versus* emitter temperature in the range of 900°C to 1600°C.

3.4.2 Simulated optical characterization

For materials with bandgaps of 0.74 eV, 0.9 eV and 1.1 eV, we use alloy compositions of $In_{0.53}Ga_{0.47}As_1P_0$, $In_{0.69}Ga_{0.31}As_{0.67}P_{0.33}$ and $In_{083}Ga_{0.17}As_{0.37}P_{0.63}$. The absorption coefficients (α) for the cells are modeled using a piece-wise function[123] given by:

$$\alpha = \begin{cases} \alpha_0 \exp\left(\frac{E - E_g}{E_0}\right), E \leq E_g \\ \alpha_0 \exp\left(1 + \frac{E - E_g}{E'}\right), E \geq E_g \end{cases} \quad (3.1)$$

These coefficients used with a transfer matrix model to determine the electric field distribution within the cell[124]. Figure 3.4 shows a comparison of the model predictions to the measured reflectance properties.

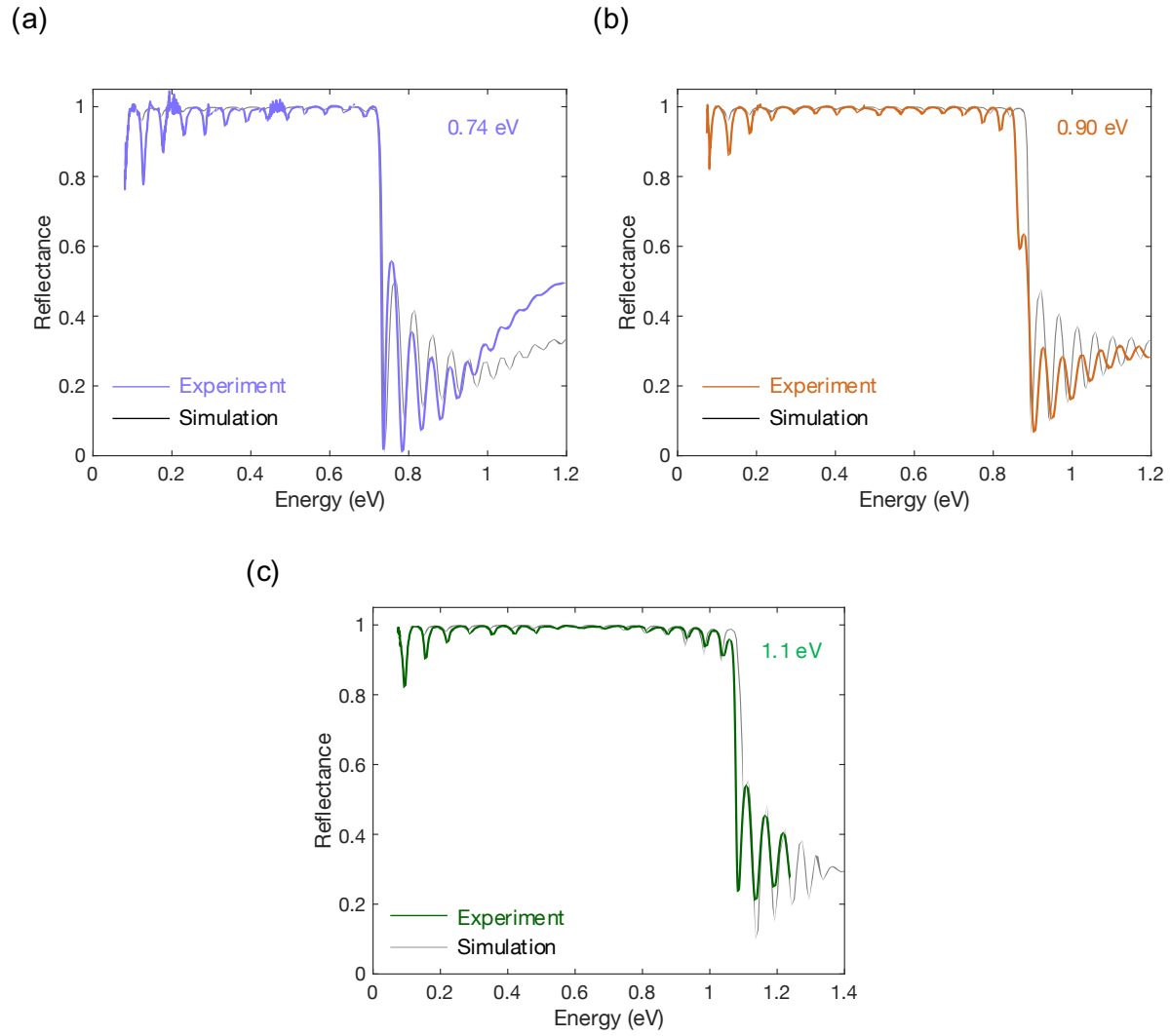

Figure 3.4 Reflectance measurements and simulations for the 0.74 eV (a), 0.9 eV (b) and 1.1 eV (c) air-bridge devices.

3.5 Carrier management characterization

Figure 3.5a shows the dark and illuminated current density-voltage (*J-V*) measurements of the three devices where we extract material properties such as the series resistance (R_s), shunt resistance (R_{sh}), and dark saturation current density in Table 3.1.

Table 3.1 Extracted material properties from dark and illuminated current measurements.

T_h (°C)	J_{01} (mA/cm^2)	J_{02} (mA/cm^2)	R_s (mΩ.cm^2)	R_{sh} (kΩ.cm^2)
0.74 eV	1.47 x 10^{-9}	1.97 x 10^{-6}	30	11
0.9 eV	6.45 x 10^{-12}	3.39 x 10^{-8}	40	825
1.1 eV	9.77 x 10^{-15}	2.04 x 10^{-9}	60	260

The performance generally agrees with calculations based on semi-empirical cell models fit to dark *J-V* measurements[125] as shown in Figure 3.5a. Figure 3.5b highlights the illuminated *J-V* and power density-voltage *(P-V)* characteristics of the three TPVs at their maximum efficiency points. Here, a SiC globar with an ellipsoidal concentrator and a SiC furnace ignitor are used as thermal emitters. The apparent view factors, determined using the measured short-circuit current, are 0.38, 0.37 and 0.33 for the 0.74 eV, 0.9 eV and 1.1 eV air-bridge devices, respectively.

Figure 3.5c shows the relationship between the electrical parameters such as open circuit voltage (V_{OC}), short circuit current density (J_{SC}), the fill factor (*FF*), and output at the maximum power point (P_{mpp}) as functions of emitter temperature. Notably, the bandgap-offset voltage (W_{OC}), which is the difference between V_{OC} and the bandgap voltage E_g, approaches 200 mV for the 0.74 eV and 0.9 eV cells at current densities of 1 A/cm^2. Series resistance losses reduce the fill factor at higher emitter temperatures due to the correspondingly higher current densities. The fill factors are in the range of 65-75% for 0.74 eV cell and 70-85% for the other two. FF generally decreases with emitter temperature due to series resistance losses and increases with bandgap due to higher V_{OC}.

However, the higher series resistance of the 1.1 eV cell, which can be attributed to worse band alignment, produces similar FFs to those of the 0.9 eV cell. The highest power densities demonstrated here are 1.2 W/cm^2 and 0.91 W/cm^2 with the 0.74 eV and 0.9 eV cells, respectively. These results follow the general dependence of measured power density on emitter temperature observed in recent TPV literature.

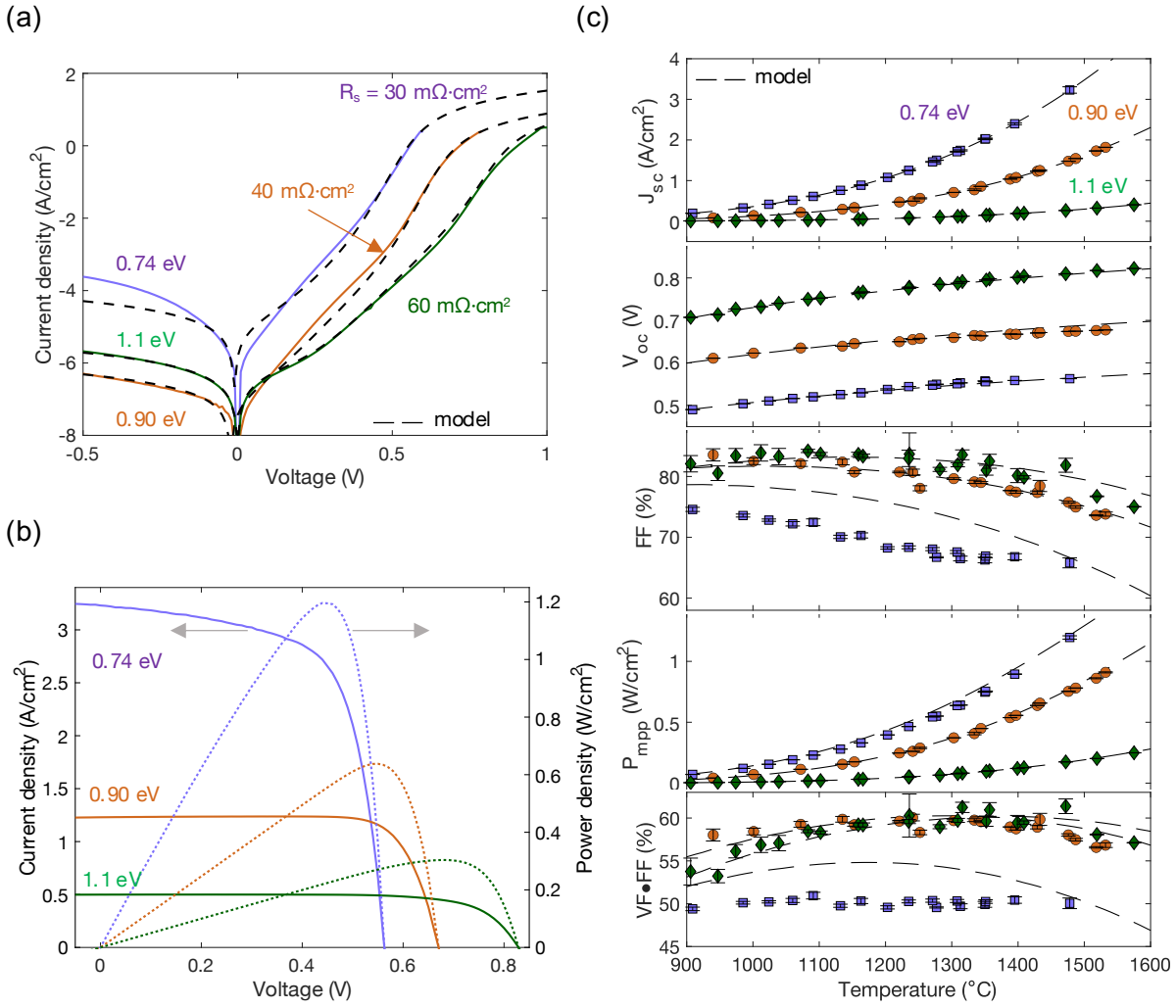

Figure 3.5 Electrical characterization of the air-bridge cells. (a) Dark current density-voltage characteristics for the 0.74 eV (purple), 0.9 eV (orange) and 1.1 eV (green) air-bridge cells. (b) Current and power density *versus* voltage for the three water-cooled cells under illumination at conditions corresponding to their maximum efficiencies. (c) Variation of short circuit current density (J_{SC}), open circuit voltage (V_{OC}), fill factor (FF), maximum power point (P_{mpp}), and carrier management efficiency ($VF{\cdot}FF$) *versus* emitter temperature (from 900 to 1600 °C) for the three

cells. The results of the semi-empirical cell model (dashed curves) generally agree with experiments.

The charge carrier management efficiencies (*VF·FF*) for the 0.9 eV and 1.1 eV cells approach 60% within this range of emitter temperatures, outperforming the 0.74 eV where *VF·FF* = 50.4 ± 0.4% at 1395°C. In comparison, the recently reported 41%-efficient tandem and the 39%-efficient single junction cells exhibited comparable values of *VF·FF* = 63% at 2400°C[4] and 59% at 1850°C (2), respectively. Complete experimental data for the devices are provided in Figure 3.6 and Table A.1 in the appendix.

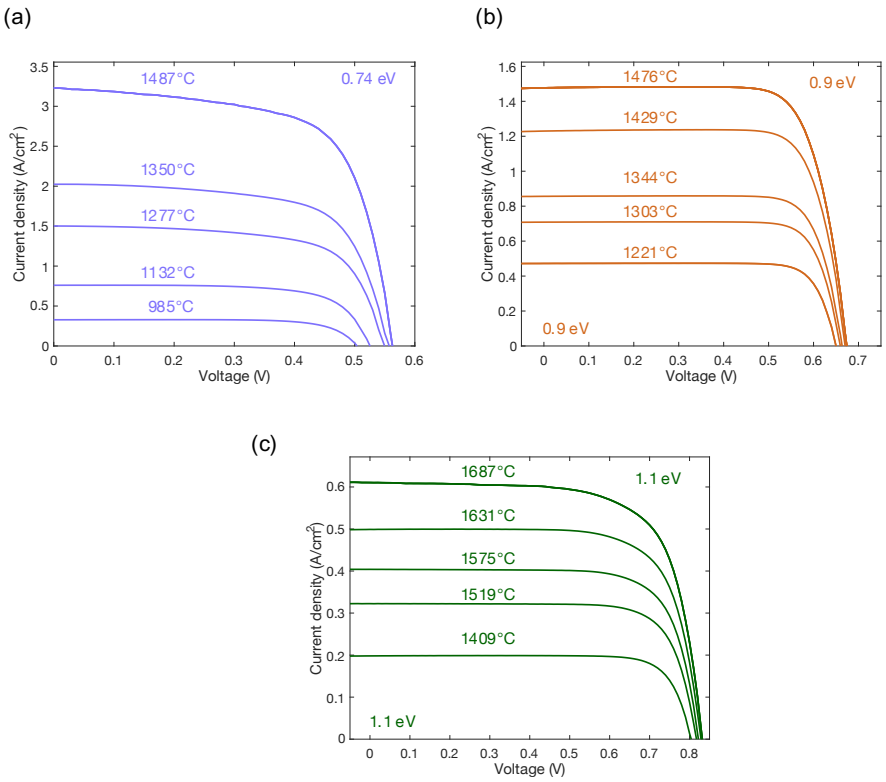

Figure 3.6 Measured electrical properties of the air-bridge cells. (a) Experimental illuminated J-*V* characteristics for the 0.74 eV InGaAs air-bridge cell at representative temperatures. (b) Experimental light J-*V* characteristics for the 0.9 eV InGaAsP air-bridge cell at representative temperatures. (c) Experimental light J-*V* characteristics for the 1.1 eV InGaAsP air-bridge cell at representative temperatures.

3.6 Efficiency characterization techniques

Efficiency is the ratio of P_{mpp} to the power absorbed by the cells (P_{abs}), which is equal to the incident minus the reflected power; our measurements of absorbed power rely on optical characterization of the reflected power, rather than direct calorimetry. Efficiency characterization techniques can be broadly categorized as (A) high view-factor calorimetry (as in Ref. [68,126]), (B) low view-factor calorimetry[4,28], (C) measurement of radiative properties (as in this work and Refs. [4,19,28,116,117]). Each technique has its own general strengths (+) and weaknesses (–) as discussed below. Specific factors and strategies used to mitigate the weaknesses of the technique C used in this chapter are also described.

A) high view-factor (>0.9) calorimetry:

+ captures the angular dependence of radiative exchange, as well as the effects of multiple reflection between the cell and the emitter.
+ accounts for series resistance losses associated with higher photocurrent levels.
+ accounts for possible *in-operando* variations in radiative properties.
– difficult to protect the cell from potential deposition of evaporated emitter material.
– scarcely implemented.

B) low view-factor calorimetry:

+ accounts for possible *in-operando* variations in radiative properties.
+ windows can be used to protect the cell from deposition of evaporated emitter material.
+ has been shown to agree with technique C.

– does not fully capture the angular dependence of the radiative exchange between the cell and the emitter because of the restricted emitter solid angle.

– does not fully account for series resistance losses associated with higher photocurrent levels.

– involves a range of possible sources of error associated with indirect heating of the stage, mixed parasitic heating and cooling effects of the electrical probes, and calibration of the calorimeter (e.g., heat flux sensor[4,72]). Corrections for these potential sources of error have not been consistently applied in the TPV literature.

C) emittance and reflectance measurement:

+ does not require sensor calibration or corrections for parasitic heating/cooling of the experimental apparatus.

+ has been shown to agree with technique B [4,28].

+ readily applied to low TRL cells characteristic of academic research.

– does not fully capture the angular dependence of the radiative exchange between the cell and the emitter because of the restricted solid angle occupied by the emitter. To mitigate this, we use the validated model to show the effect of hemispherical integration on efficiency in.

– does not account for possible in-operando variations in radiative properties. To mitigate this, we (i) measure the spectral emittance of the emitter in-operando, (ii) manage the temperature of cell to between 23 and 32 ºC to minimize the effects of bandgap narrowing, (iii) ensure that the radiative properties before and after testing are consistent.

– does not fully account for series resistance losses associated with higher photocurrent levels. To mitigate this, we use the validated cell model to show the effect of increasing the view factor on efficiency.

3.7 TPV Efficiency

Competition between spectral and carrier management results in a dependence of performance on emitter temperature shown in Figure 3.7a. There, we also show a trend that is fit to recent reports of high-performance TPVs as shown in Figure 3.7b. The efficiency increases with emitter temperature as more incident power shifts to the in-band region, before it gradually decreases due to thermalization and series resistance losses, and cell heating. These effects lead to an optimal operating point that shifts to higher temperatures with increasing bandgap. The 0.9 eV cell shows a peak efficiency of 43.8 ± 0.5% at 1435°C, which represents a 15% absolute improvement compared to a cell without the air bridge. The highest efficiencies measured for the 0.74 and 1.1 eV cells are 36.0 ± 0.3% at 1480°C and 36.1 ± 0.2% at 1630°C, respectively.

Interestingly, the 0.9 eV device matches the spectral efficiency of the 0.74 eV cell at 1250°C while increasing the output voltage from 560 mV to 670 mV, which corresponds to a nearly 20% relative improvement in carrier management (see Figure 3.7d). The 0.9 eV cell shows substantially enhanced spectral performance and comparable carrier management relative to previously reported devices[4,118]. We note that those results were achieved using larger cells and that increasing the cell area without sufficient optimization of the grid architecture may introduce additional losses such as higher series resistance. The view factor in our test station is ~0.37, which limits the measured power density; nonetheless, simulations suggest >40% cell efficiency can be achieved at near-unity view factors as shown in Figure 3.7c. These results demonstrate the advantages of increasing the bandgap to improve carrier utilization while relying on the air-bridge to manage the absorbed spectrum, rather than attempting to harvest a broader range of wavelengths using a lower bandgap device.

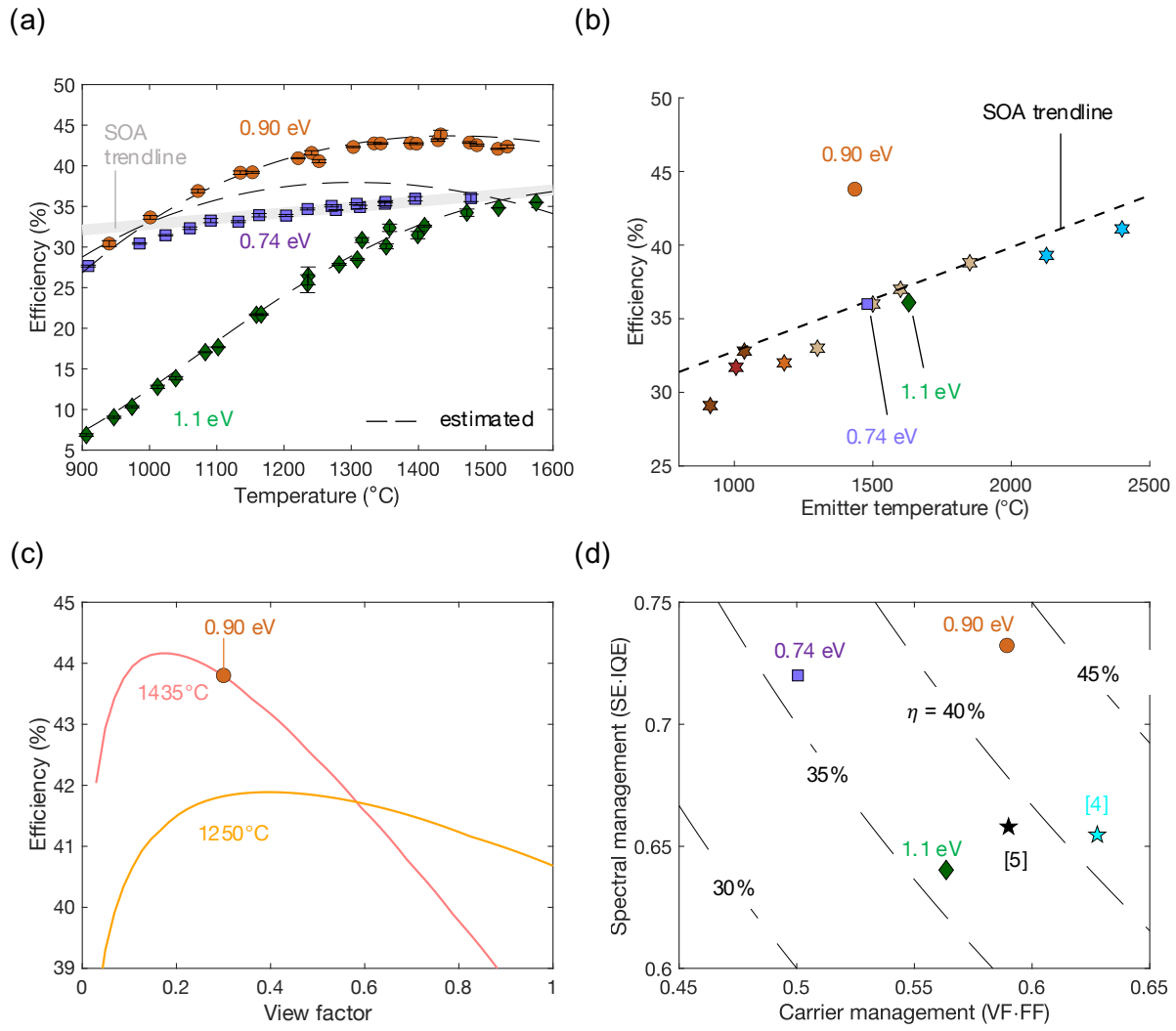

Figure 3.7 Efficiency of the air-bridge cells. (a) Efficiency of air-bridge cells as a function of emitter temperature (T_h). Gray line represents the best fit for different state-of-the-art TPV cells. (b) Efficiency versus emitter temperature showing the state-of-the-art TPV cells (star markers), a trendline for these SOA cells[4,19,28,115,122]and the maximum efficiencies for the three bandgap materials measured in this study. The trendline is a best fit based on the data shown and has been shifted upward to intercept the topmost data points. (c) Simulated efficiency versus view factor for the 0.9 eV cell. At 1250°C, the 0.9 eV cell demonstrates the highest efficiency at near-unity view factors. (d) Spectral management (SE·IQE) vs. carrier management (*VF·FF*) for the air bridge cells at their maximum efficiencies. Dashed curves represent efficiency benchmarks while the star markers signify the best previously reported efficiencies: blue[4] and black [118].

The foregoing demonstrates that >40% TPV efficiency is possible over a wide range of emitter temperatures by using the airbridge design along with an optimized bandgap. Specifically, the 0.9 eV device outperforms the other cells at emitter temperatures from 950 to 1600°C. This feature

benefits a broad array of energy harvesting technologies, ranging from small nuclear reactors to scavenging waste heat in manufacturing processes, to large-scale stationary energy storage. In thermal battery applications, this improvement can benefit both the cost per unit power generated (CPP) and the cost per unit energy stored (CPE)[1]. In particular, the round-trip efficiency of thermal batteries is set by the *average* TPV efficiency over the range of emitter temperatures encountered during the discharge phase. This implies that the cost per unit energy (CPE) approximately scales with the magnitude of the temperature range over which the efficiency exceeds a target threshold . Therefore, the cells demonstrated here can substantially increase the storage capacity of thermal batteries (i.e., more energy can be stored per unit mass of the storage medium), thereby significantly decreasing CPE, and further improving competitiveness with other storage technologies.

3.8 Summary

Single-junction air-bridge cells in three absorber bandgaps ranging from 0.74 eV to 1.1 eV, were demonstrated and characterized at moderate emitter temperatures ranging from 900 to 1600°C. For each material, we demonstrate enhanced spectral efficiency enabled by an air-bridge that offers near unity reflectance of out-of-band radiation. Our results show that increasing the bandgap within this temperature range leads to improved charge carrier utilization while the negative impact on spectral utilization is minimized because of the high out-of-band reflectance. The 0.9 eV cell exhibits the highest efficiency (43.8 ± 0.5% at 1435°C) by combining a charge-carrier management efficiency of 59.8 ± 0.7% and a spectral management efficiency of 73.3 ± 0.1%. To our knowledge, this is the highest efficiency from either single or multiple junction TPVs reported to date.

Chapter 4: Semitransparent Thermophotovoltaics for Efficient Utilization of Moderate Temperature Thermal Radiation

This chapter is adapted from Burger, T., Roy-Layinde, B., Lentz, R., Berquist, Z. J., Forrest, S. R. & Lenert, A., "Semitransparent thermophotovoltaics for efficient utilization of moderate temperature thermal radiation," *Proceedings of the National Academy of Sciences* 119, e2215977119 (2022).

4.1 Motivation

The performance of thermophotovoltaic (TPV) cells has increased substantially over the last several years, with reports of TPV efficiency surpassing 30% using single-junction cells[127–131], and 40% using tandems[132]. These gains have been demonstrated using group III-V semiconductors (*e.g.*, $In_{0.53}Ga_{0.47}As$ lattice matched to InP) with wider bandgaps compared to conventional Sb-based TPV cells. Although these materials exhibit advantageous optical and charge carrier collection properties, they typically require emitter temperatures (T_h) above 1200°C[133]. Applications in stationary energy storage using thermal batteries may support extreme emitter temperatures as high as 2400°C, however, a wide range of thermal sources are at temperatures below 1100°C, including waste[134–136], concentrating solar thermal[137–144], and nuclear[145] heat.

4.2 Challenges associated with lower emitter temperatures

Translating recent improvements in cell performance to waste, solar and nuclear applications is challenging since lower temperatures introduce substantial spectral (photon) and charge carrier losses[63]. This can be appreciated by noting that TPV efficiency (η_{TPV}) is a product of spectral

management (*SE·IQE*) and charge management (*VF·FF*) efficiencies[63]. Here, *SE*, *IQE, VF* and *FF* are the spectral and internal quantum cell efficiencies, and the voltage and fill factors, respectively. Lower temperature emitters radiate a larger fraction of power at energies below the cell bandgap, resulting in lower *SE*. The conventional solution to this problem is to decrease the cell bandgap using Sb-based III-Vs; however, the voltage penalties associated with non-radiative recombination are prohibitively large in these materials, which results in poor charge management. Alternatively, light management techniques that suppress below-bandgap (i.e., out-of-band) absorptance (A_{OOB}) can enable the use of highly efficient III-V absorbers, such as $In_{0.53}Ga_{0.47}As$ (bandgap of 0.74 eV), by maintaining high spectral efficiency at lower emitter temperatures.

4.2.1 Conventional techniques for mitigating spectral challenges

Existing techniques for suppressing below-bandgap radiative transfer in TPVs can be broadly categorized as emissive and reflective. Figure 4.1 shows the spectral efficiency corresponding to the best measured $In_{0.53}Ga_{0.47}As$ (InGaAs) TPV efficiencies at moderate-to-low emission temperatures. The lowest *SE* region corresponds to selective emitters[63] that are designed to preferentially emit above-bandgap radiation while suppressing below-bandgap emission[55,146]. Although these emitters have demonstrated A_{OOB} as low as 7% at room temperature[147], the emissive properties are generally much higher (>14%) when characterized at the appropriate operating temperature[63,148–150]. In contrast, cells with conventional rear mirrors exhibit A_{OOB} as low as 5%[47,48,132,151–154]. These cells reflect below-bandgap radiation back to the emitter, which re-heats the emitter and facilitates recuperation of otherwise unusable power. Beyond conventional rear mirrors, cells that feature a low-index layer separating the absorber from the rear metal, including patterned dielectric back contact[45] and air-bridge cells[128], have enabled A_{OOB} as low as 2%

(integrated from 0° to 90° incidence angle). Despite these recent advances in spectral management, a device that suppresses below-bandgap transfer with $A_{OOB} < 1.5\%$ has yet to be demonstrated. Accessing this regime would enable TPV cells based on InGaAs to maintain high efficiencies at temperatures relevant to conversion of waste, solar thermal, and nuclear heat.

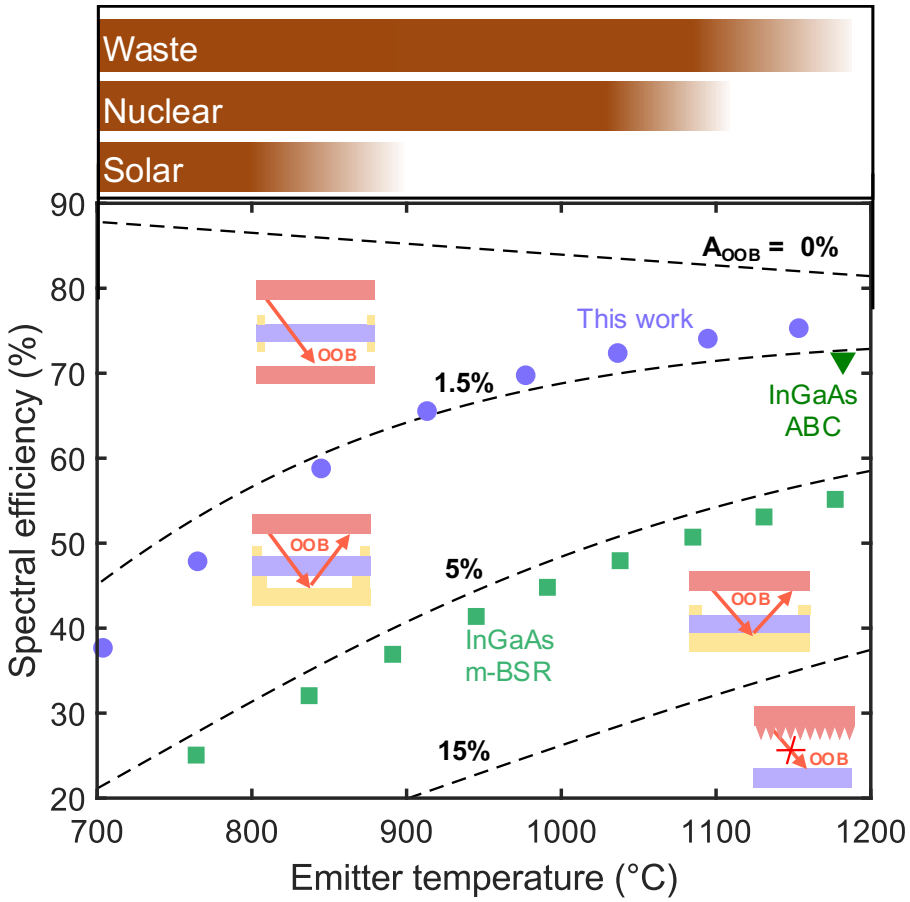

Figure 4.1 Current performance in spectral control at moderate-to-low emitter temperatures. Spectral efficiency as a function of emitter temperature in a range which is relevant to applications in conversion of waste, solar, and nuclear (WSN) heat. Out-of-band absorptance $A_{OOB} > 15\%$, $5 > A_{OOB} > 15\%$ and $1 > A_{OOB} > 2\%$, are characteristic of spectral performance achieved through use of selective emitters, metallic BSRs (m-BSRs) and metal-dielectric BSRs, respectively. ABC refers to an air-bridge cell. Spectral control strategies are depicted as inset schematics. $A_{OOB} < 1.5\%$ indicates the target range for the semitransparent cells described in this work. The black top curve indicates *SE* in the radiative limit ($A_{OOB} = 0$). *SE* curves are generated for $E_g = 0.74$ eV and in-band absorptance (A_{IB}) of 0.7.

4.2.2 Our unique approach relying on semitransparency

In this chapter, we demonstrate the concept of transmissive spectral control that enables wavelength-selective radiative transfer with $A_{OOB} < 1.5\%$ and high TPV efficiency at moderate-to-low emission temperatures. The concept features a symmetric infrared-transparent photovoltaic cell that is situated between two thermal emitters and is thermally grounded by heat sinks on either edge, as shown in Figure 4.2. Surrounding the cell by the emission source is possible in TPVs, unlike in solar cells, because the heat source is local (though, this unique feature has not been explored in prior TPV work). In this configuration, emitted below-bandgap photons transmit through the cell and are absorbed by the thermal emitter on the opposite side, and vice versa. Due to this symmetry, the net movement of photons is zero along the centerline of the cells. This implies that the centerlines act as perfect broadband reflectors, unlike dielectric and metal mirrors which are limited by bandwidth or intrinsic absorption (associated with finite electrical conductivity), respectively.

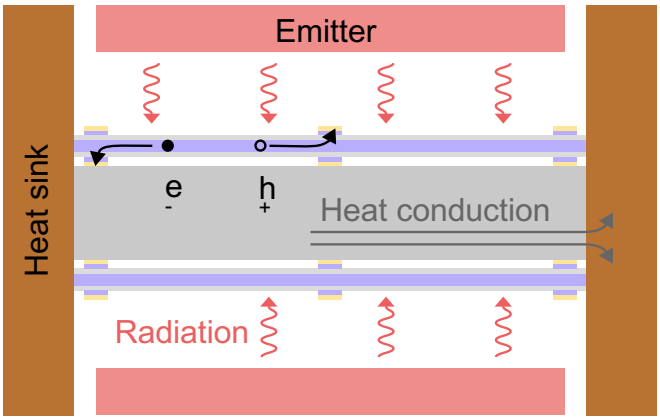

Figure 4.2 The semitransparent cell concept. Heat flows and carrier transport depicted in a two-dimensional projection of a semitransparent TPV system: absorption of IB radiation excites electron-hole pairs in the absorber, which are separated and extracted at the contacts; OOB radiation transmits through the cell and is absorbed by the thermal emitter on the opposite side; waste heat is conducted laterally along the length of the transparent substrate to the conductive heat sinks.

We demonstrate the concept by fabricating a semitransparent TPV cell consisting of a thin InGaAs/InP heterojunction membrane supported by an infrared-transparent heat-conducting substrate.The device builds upon our recent demonstration of air-bridge TPV cells that achieved power conversion efficiencies of 32% at an emitter temperature of ~1200°C[128]. The air-bridge cell, however, exhibited $A_{OOB} \approx 2\%$ when integrated over all incidence angles, mainly due to relatively high absorption in the Au mirror at oblique angles. To overcome this limitation, the semitransparent device eliminates the Au mirror and retains a transparent substrate ("fin") that allows transmission of thermal radiation. Owing to minimal photon loss (~1%), the InGaAs cell demonstrated here achieves 72.2 ± 0.2% spectral efficiency and 32.5 ± 0.1% TPV efficiency at an emitter temperature of 1036°C. The latter result represents an 8% absolute improvement (~33% relative) over previously measured cells at comparable temperatures[48]. We expect that the device architecture introduced here could be broadly deployed to minimize optical losses and enable the use of wider bandgap cells, with key applications in clean energy and industrial waste heat recovery.

4.3 Design considerations and fabrication

To reach high TPV efficiency at lower emitter temperatures, the semitransparent device must combine efficient electrical and thermal management with near-zero photon losses. To this end, the design of the cell, gridlines, and substrate should minimize absorption of below-bandgap photons without degrading other performance characteristics.

4.3.1 Material growth

The heterostructure was epitaxially grown on a 300μm thick (100) InP substrate using metalorganic chemical vapor deposition (University Wafer Inc., South Boston, MA, USA). The epitaxial film consists of a 200nm thick Mg-doped (1 x 10^{18} cm^{-3}) $In_{0.53}Ga_{0.47}As$ (InGaAs) front contact layer, 300nm Mg-doped (1 x 10^{18} cm^{-3}) InP front window layer, 1.4μm thick Si-doped (1 x 10^{17} cm^{-3}) InGaAs absorber layer, 100 nm Si-doped (1 x 10^{18} cm^{-3}) InP rear window layer, and 100nm thick Si-doped (1 x 10^{18} cm^{-3}) InGaAs rear contact layer.

4.3.2 Fabrication

All layers are photolithographically patterned using SPR 220 3.0 photoresist (Kayaku Advanced Material Inc., Westborough, MA, USA.). Metal layers are patterned using LOR 10B (Kayaku Advanced Material Inc., Westborough, MA, USA.) and SPR 220 3.0 bilayer photoresist. The epitaxial sample and a Si wafer are soaked in buffered HF for 90s to remove the native surface oxides. The cathode contact grid (10nm Ti / 225nm Au) is deposited by electron-beam evaporation in a chamber with a base pressure of $4x10^{-6}$ torr. Grid lines are 10 μm wide on a 64 μm pitch. The epitaxial sample is soaked in 1:1:8 H_3PO_4:H_2O_2:H_2O for 20s to remove the 100 nm thick InGaAs rear contact layer in the area between grid lines, while the contact layer beneath the grid lines is protected. Parallel Au patterns on the epitaxial sample and Si wafer (the substrate) are spatially aligned and cold-weld bonded using a flip chip bonder (Finetech) by applying heat (150°C) and pressure (2 MPa) for 5 min. The bond strength is increased at the same temperature and higher pressure (8 MPa) for 10 min using an EVG 510 wafer bonder. The bonded sample is soaked in HCl for 90 min to remove the InP substrate. This process is compatible with non-destructive epitaxial lift-off techniques, which may preserve the expensive InP growth substrate for additional

growths[155]. The device mesa is etched by alternating soaks in InGaAs (1:1:8 H_3PO_4:H_2O_2:H_2O) and InP (1:1 HCl:H_2O) etchant solutions. The anode contact grid (10 nm Ti / 30 nm Pt / 560 nm Au) is deposited by electron-beam evaporation. The anode contact grid is spatially aligned to the buried cathode contact grid epitaxial layer to shade the absorptive InGaAs contact layers. Lastly, the sample is soaked in 1:1:8 H_3PO_4:H_2O_2:H_2O 60s to remove the 300nm thick InGaAs front contact between the grid lines.

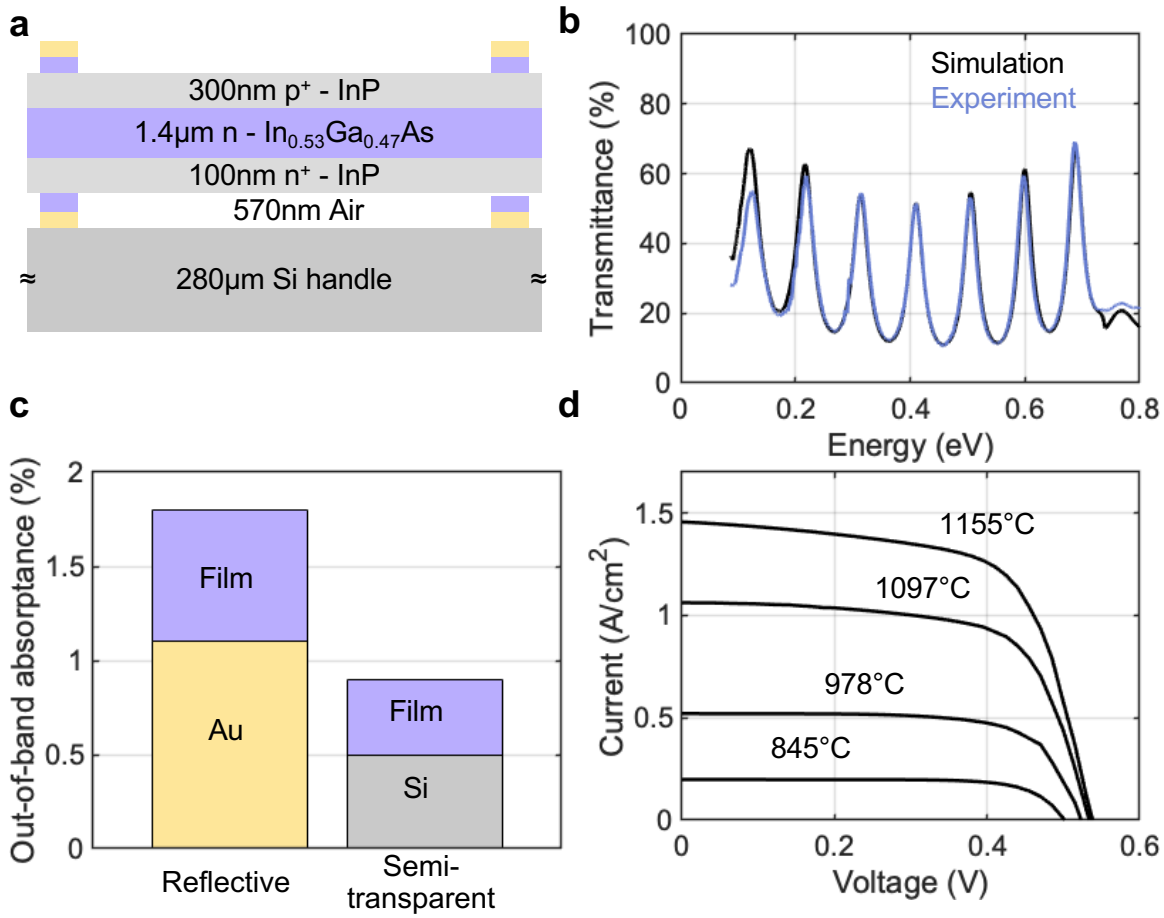

Figure 4.3 Optical and electrical characterization of the semitransparent cell. (a) Schematic of the fabricated semitransparent cell. This cell consists of a 280μm thick IR-transparent Si substrate supporting an InGaAs/InP heterojunction PV cell. (b) Transmittance of the semitransparent cell. Experimental transmittance (blue), measured by FTIR, matches the simulated transmittance (black) for energies > 0.13eV. (c) Contributions of active and inactive layers to the total OOB absorptance in the reflective (left) and semitransparent (right) cells. (d) Example illuminated *J-V* characteristics for the semitransparent cell.

4.4 Results

We demonstrate a semitransparent TPV cell consisting of a thin InGaAs/InP heterojunction with a Au electrode grid matched to a similar grid on the Si substrate, as shown in Figure 4.3a. The Au patterns are aligned and cold-weld bonded using a flip chip and wafer bonding tool (see Methods). The process retains a 570 nm air-gap while allowing light to transmit through the substrate between the grid lines. To minimize parasitic absorption, the n-type InGaAs absorber and InP layer are 1.7 μm thick with a dopant concentration of 1 x 10^{17} cm^{-3}, whereas the heavily p-doped InGaAs (1 x 10^{18} cm^{-3}) contact layers are shaded by the metal gridlines. For the substrate, we use double-side polished Si that is chemically compatible with the III-V processing protocol[128,156] and has a high thermal conductivity of 130 W/m/K at 25°C. Use of intrinsic, float zone Si minimizes free carrier and impurity absorption leading to a low mid-IR extinction coefficient.

4.4.1 Optical characterization

Reflectance properties of the semitransparent and air-bridge control cells are measured using an Agilent Cary 620 FTIR microscope with incidence angles in the range of 18-41°. Figure 4.3b depicts the spectral transmittance of the cell at normal incidence as measured by Fourier transmission IR spectrometry. Experimental transmittance is observed to marginally deviate from simulation for energies less than 0.13eV. This measurement is paired with the spectral reflectance of the semitransparent cell (as shown in Figure 4.4a) to yield A_{OOB} = 0.9%, as weighted by emission from a blackbody at 1227°C (1500 K). For reference, a reflective air-bridge control fabricated using the same epitaxial growth exhibits a measured A_{OOB} = 1.8% (see Figure 4.4b).

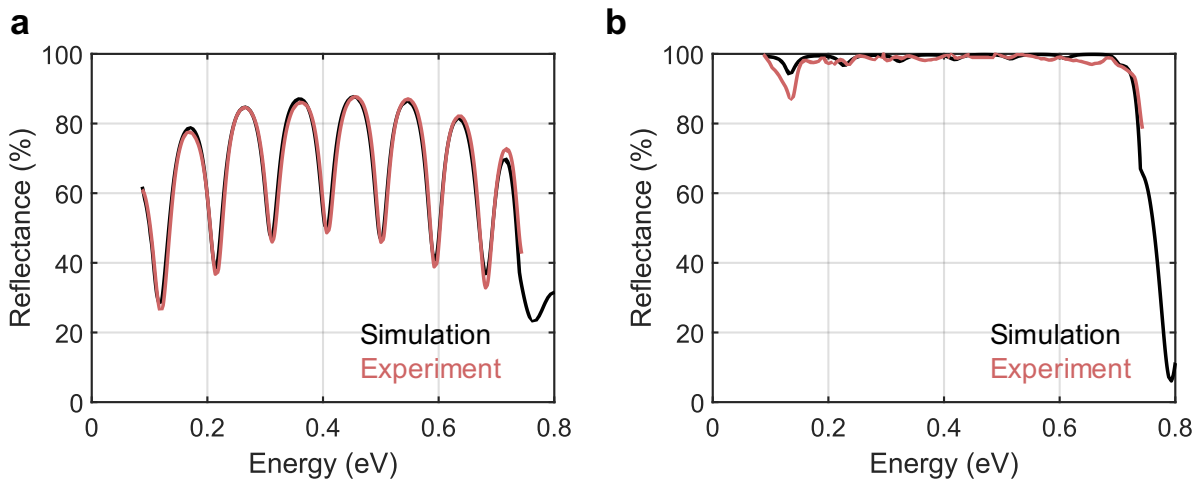

Figure 4.4 Reflectance measurements and simulations for the semitransparent (left) and reflective air-bridge control (right).

We further utilize transfer matrix optical modeling[157] to estimate the contributions of the Au reflector and the Si substrate in the reflective and semitransparent cells. Figure 4.3c shows the contributions of the active and inactive layers of each cell to the total below-bandgap absorptance. The Au absorbs 1.1% and the heterostructure absorbs 0.7% in the reflective air-bridge cell. In contrast, the polished Si substrate only absorbs 0.5%. We assign the remaining parasitic absorption (0.4%) to the InGaAs/InP heterostructure. This film is slightly more absorptive than that in previous work[128], which may be attributed to differences in the growth process (metallorganic chemical vapor deposition vs. molecular beam epitaxy) and/or layer thickness differences. Nonetheless, results show that by removing the Au reflector, absorption is substantially reduced, thus demonstrating the fabrication of semitransparent TPV devices with $A_{OOB} < 1.5\%$.

4.4.2 Electrical characterization

To characterize the power output and efficiency of the cells, voltage sweeps were performed under illumination by a SiC globar with an ellipsoidal concentrator, as previously[128]. Figure 4.3d depicts a set of illuminated current density-voltage (*J-V*) characteristics for the semitransparent cell, with T_h ranging from 700°C to 1215°C. Complete experimental data are provided on table 4.1 below. Short-circuit current densities, J_{sc}, are in the range of a realistic TPV system (view factor of ~0.75). The voltage factors are higher than our previous work, which is attributed to improved wafer quality. The series resistance and saturation dark currents, extracted from fitting both illuminated and dark measurements, show that patterning the rear Au layer slightly increases series resistance. Although not shown, thicker Au gridlines can be used to mitigate this effect.

Table 4.1 Measured *J-V* properties of the semitransparent cell vs. emitter temperature.

T_h (°C)	J_{SC} (mA/cm^2)	V_{OC} (mV)	FF (%)
704	54.72	470.28	75.96
765	99.61	485.88	76.01
845	255.46	508.07	73.84
913	369.57	515.65	72.37
978	516.52	522.74	70.84
1036	710.84	529.05	69.20
1097	1062.17	534.75	66.72
1155	1457.11	538.62	64.81
1212	1959.57	541.76	63.57

4.4.3 Thermal management:

Figure 4.5a (left) depicts the anticipated temperature profile along the length of a semitransparent cell for an emitter temperature of 1200°C and a view factor of 100%. The temperature of the active region is expected to be slightly higher (+0.5°C) than the substrate temperature due to thermal resistance across the air gap. The average cell (junction) temperature for this illumination condition is 29°C. Figure 4.5b (right) shows that a 500 μm thick substrate may provide better heat conduction, therefore mitigating cell heating losses at high emitter temperatures. However, this also increases parasitic absorptance at long wavelengths, resulting in lower efficiencies at moderate temperatures, for which more OOB power is emitted and the thermal load is reduced. This result depends on the heat conduction path length of the cell.

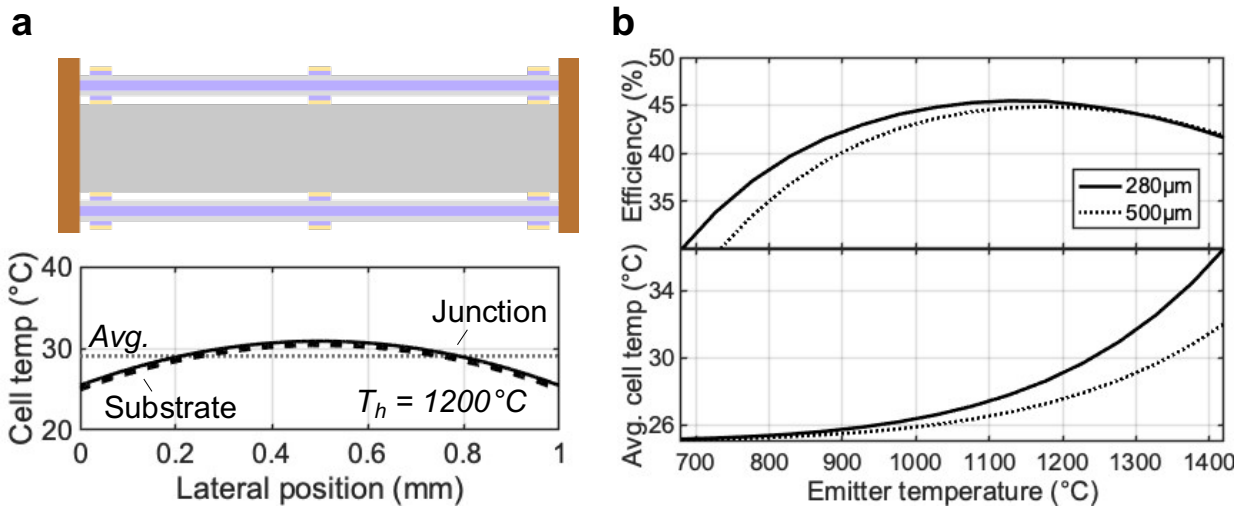

Figure 4.5 Substrate geometry effects on cell temperature, optical loss, and efficiency. (a) Anticipated temperature profile of a 1-cm long semitransparent cell illuminated by a 1200°C blackbody emitter. Junction temperature (solid curve) is slightly higher than substrate temperature (dashed curve) because of the thermal resistance of the air gap. (b) Average cell temperature and predicted efficiency as a function of emitter temperature for a semitransparent cell with a 280μm (solid curve) and a 500μm (dashed curve) Si substrate.

4.4.4 Cell heating effects

Cell heating effects for the semitransparent cell assume a temperature coefficient of β_η = -0.16%/K, based on the anticipated T_c at the given T_h. The temperature coefficient of the semitransparent cell is determined through characterization of the cell power output for a range of cell temperatures, as previously[158]. The temperature profile is calculated from the anticipated thermal load at each T_h using a one-dimensional heat conduction model with a volumetric heat generation term.

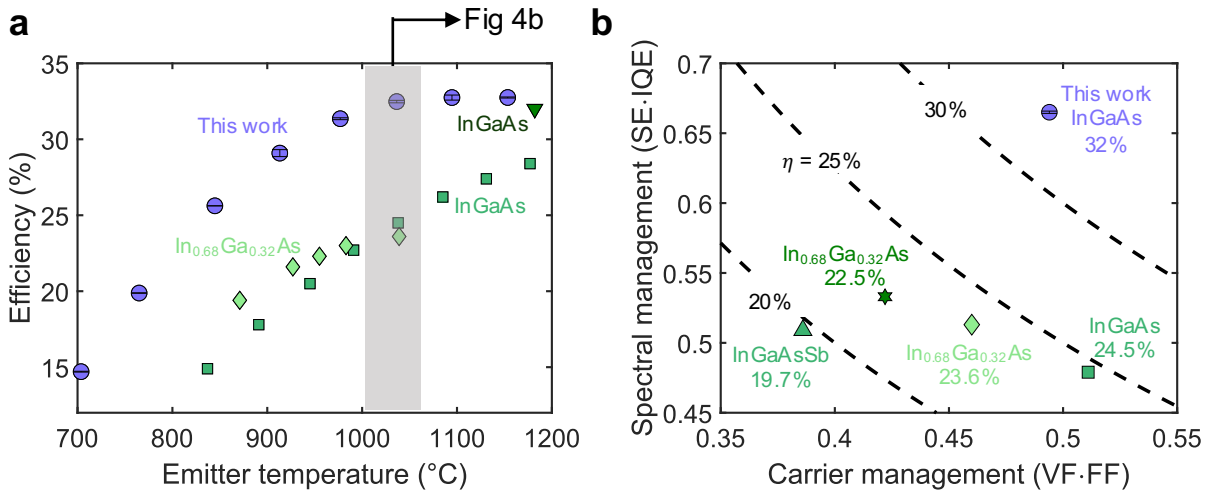

Figure 4.6 Efficiency of the semitransparent cell. (a) TPV efficiency of the semitransparent (purple) cell as a function of variable emitter temperature (T_h). The best previously reported measured efficiencies within this T_h range are depicted by the green squares[48], diamonds[159] and downward triangle[128]. (b) Spectral management (*SE·IQE*) as a function of carrier management (*VF·FF*) for TPV cells in the temperature range of 1000°C-1050°C. Dashed curves represents efficiency benchmarks: square[48], diamond[159], star[160], and upward triangle[161].

4.5 Power conversion efficiency

Figure 4.6a shows the TPV efficiency (η_{TPV}) vs. T_h for the semitransparent cell compared to the best previously reported measured efficiencies within this T_h range[48,128,159]. η_{TPV} is defined as the ratio of power generated to the radiative heat absorbed by the cell[128]. The efficiency decreases with

decreasing emitter temperature due to the red-shifted emission spectrum, which increases spectral losses at photon energies < 0.13 eV. *PCE* also decreases with increasing emitter temperature due to cell heating (see *Supporting Information*). We note that the semitransparent geometry requires lateral heat conduction along the substrate to moderate cell temperature, whereas a reflective cell can be directly cooled from the back. Despite these losses, the semitransparent cell achieves *PCE* = 32.5 ± 0.1 % at ~1036°C. This represents an 8% absolute (~33% relative) improvement compared to the prior highest efficiency of 24.5%[48] (at the time of publication) at comparable emitter temperatures of 1000-1050°C. We also note that the semitransparent cell exhibits a ~6% relative improvement compared to the reflective air-bridge control at ~1036°C as shown in Figure 4.7. This efficiency gap narrows with decreasing T_h, however, because the Si substrate absorbs at energies below 0.13eV.

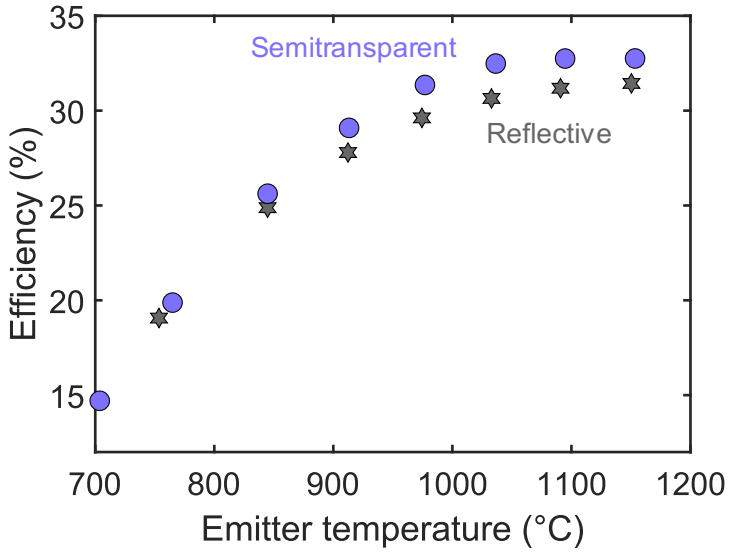

Figure 4.7 Power conversion efficiency of the semitransparent (purple) and reflective air-bridge control (gray) cells as a function of variable emitter temperature.

To further highlight the improvements relative to state-of-the-art approaches, we separate contributions to the TPV efficiency due to the spectral management and carrier management efficiencies, as shown in Figure 4.6b. The improved spectral management of the semitransparent design is captured by the relative position of the purple data point along the vertical axis. In addition, the semitransparent device exhibits a high carrier management efficiency, comparable to the best InGaAs devices using conventional metallic reflectors[48]. Overall, this result demonstrates that the semitransparent architecture does not compromise carrier management, while providing a substantial gain in spectral management of moderate temperature emission.

4.6 Near term improvements

Here, we use optical and electronic simulations[128,158] to optimize the design of a symmetric, bifacial semitransparent cell based on the demonstrated device characteristics. The effects of material quality and gridline optimization are modeled by assuming a Shockley-Read-Hall recombination lifetime of τ_{SRH} = 47μs, which to our knowledge is the longest reported for InGaAs[162], and a series resistance R_s = 10 mΩ cm^2, which has been attained for similar patterned dielectric back contact devices[45]. The cell is assumed to be 1 cm in length and supported at both ends by a 25°C heat sink. Figure 4.8a shows the dependence of TPV efficiency on these carrier management assumptions. Notably, the efficiency of a bifacial semitransparent cell with a 280 μm thick Si substrate is expected to exceed 40% with a 1000°C emitter. Figure 4.8a further shows the dependence on substrate thickness, which affects both cell temperature and optical performance. The model predicts that thinner substrates (*e.g.*, 100 μm) improve performance at lower emitter temperatures, at which thermal management via heat conduction does not limit performance. In contrast, a 500 μm thick substrate may provide better heat conduction, but it leads to increased

parasitic absorptance at long wavelengths, resulting in lower efficiencies within this temperature range.

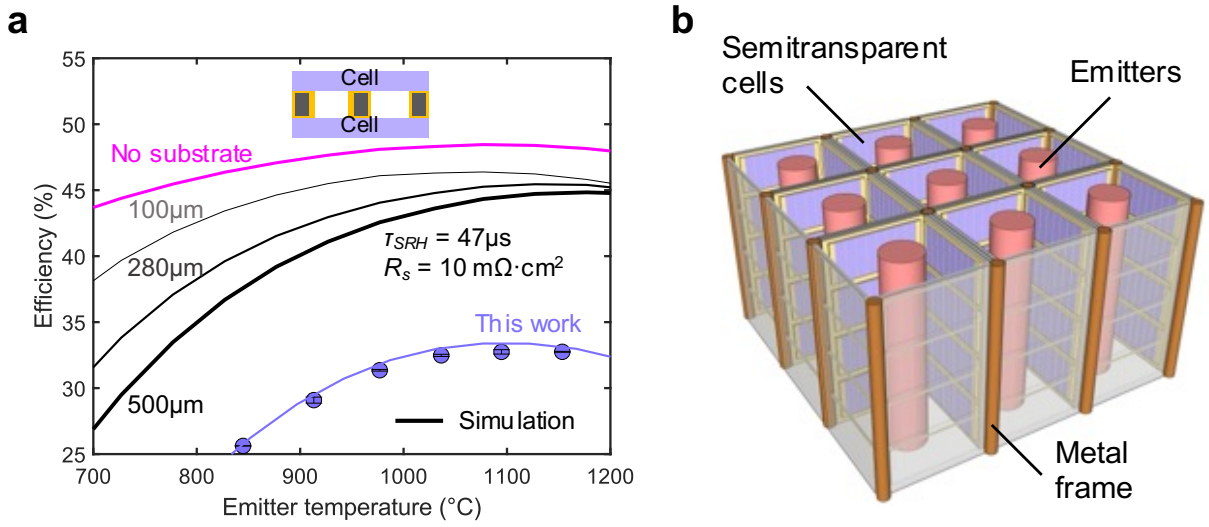

Figure 4.8 Opportunities in transmissive control. (a) The dashed lines highlight near-term improvements (InGaAs with R_s = 10mΩ.cm^2 and τ_{SRH} = 47μs[89]) with no substrate (in magenta) and with Si substrate of thicknesses 100μm, 280μm and 500μm (in black). The simulation predicts the highest efficiency when the substrate is altogether replaced by mechanically supportive, heat-conducting gridlines, which may enable $A_{OOB} < 0.5\%$ and negligible temperature gradients. Purple circles represent the experimental *PCE* for semitransparent cell demonstrated in this study while the purple dashed line is a simulation of our experimental work. (b) Proposed modular design for interfacing semitransparent cells and emitters. In this geometry, an array of metal fins supports and manages the temperature of the semitransparent cells, which are illuminated by an interlocked array of cylindrical emitters

Lastly, we explore a design consisting of mechanically supportive, heat conducting grid lines in place of the Si substrate. The gridlines may comprise highly conductive materials such as copper, graphite, or other emerging materials such as cubic boron arsenide[163], and can be coated with Au to reduce optical loss. This configuration has the potential to reduce A_{OOB} to below 0.5% and enable a peak efficiency of 48.5% at 1000°C, provided that the active semiconductor membrane is the only source of parasitic absorption.

Although beyond the scope of this chapter, we expect that the risks associated with temperature rise of the cell can be mitigated through optimization of geometrical parameters such as aspect ratio and fin thickness. Specifically, the metallic frame can be optimized to remove waste heat and maintain cell temperatures. In Figure 4.8b, we show that the semitransparent cells can be interdigitated with multiple hot emitters in a cross-flow geometry. Thermally grounding the fins along two edges decreases the heat diffusion path length by a factor of two compared to an open-ended fin, which in turn, decreases temperature rise by a factor of four.

4.7 Conclusions

In this chapter, we demonstrated transmissive spectral control as an approach for achieving wavelength-selective radiative transfer in thermophotovoltaic systems that has the potential to overcome the limitations of emissive and reflective methods. The approach features a symmetric device that captures transmitted below-bandgap photons using a secondary thermal emitter situated at the rear, thereby recovering the large amount of power carried by these photons. We fabricated a semitransparent cell with a single, thin InGaAs/InP heterojunction membrane, supported by an intrinsic, float zone Si wafer. Experimental spectral analysis is paired with simulation to decouple contributions to parasitic absorptance in the semitransparent cell. In the temperature range relevant to conversion of waste, solar, and nuclear generated heat, we demonstrated a 33% relative improvement compared to previously reported efficiencies. Our simulations show that efficiencies as high as 48% could be achieved at 1000°C by optimizing material quality and thermal management within the framework of transmissive spectral control. Overall, we show that this approach to photon management may expand the use of TPVs into a wider range of applications with significant potential to reduce greenhouse gas emissions.

Chapter 5: Ultrahigh Spectral Efficiency in Multi-Junction Thermophotovoltaics Enabled by Dual Air-Bridge Cells

Portions of this chapter are adapted from a manuscript by Roy-Layinde, B., Lim, J., Forrest, S. R. & Lenert, A., "Integrated air-bridge tandem thermophotovoltaics with high efficiency over a broad heat source temperature range" under revision.

5.1 Introduction

Realizing efficient photon recovery in multijunction cells has the potential to maximize the performance of TPVs for renewable energy applications such as in grid-scale energy storage (thermal batteries). Recently, 1.4/1.2 eV and 1.2/1.0 eV bandgap multijunction cells reported by LaPotin *et al* demonstrated 41% and 39% TPV efficiency under 2000°C illumination[4]. This cell uses a highly doped semiconductor tunnel junction for series connection of the top and bottom cell within the tandem as shown in Figure 5.1a. Unfortunately, conventional tunnel junctions introduce substantial parasitic absorption below the bandgap due to optical response of free carriers and ionized donors/acceptors, which significantly degrades R_{OOB}[164–166]. Furthermore, the current matching constraint imposed by such tunnel junctions limits the range of emitter temperatures over which high performance is maintained. Temperature sensitivity is particularly important in thermal batteries where larger temperature swings can produce higher specific capacities and concomitantly lower energy storage costs.

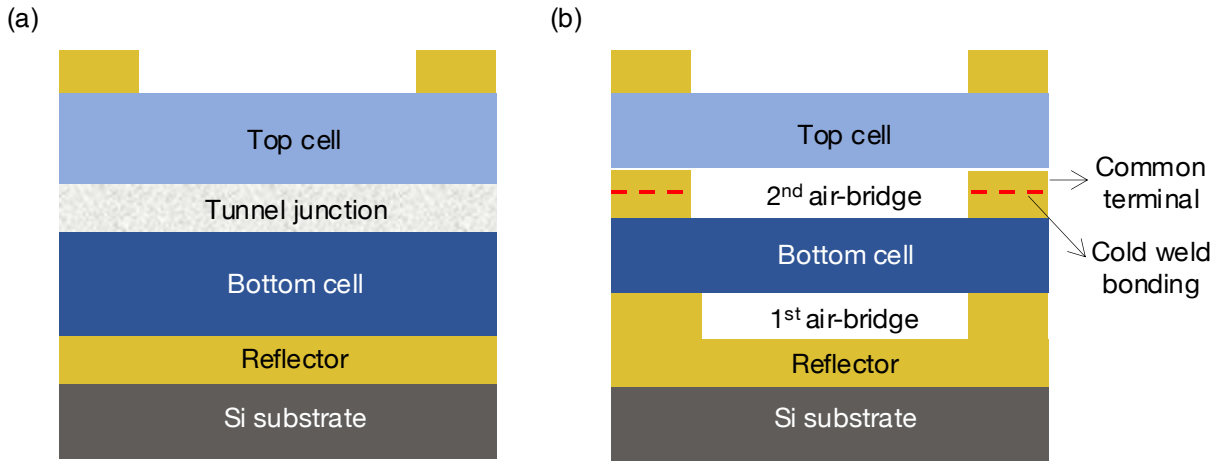

Figure 5.1 Multijunction TPV. (a) Conventional multijunction cell utilizes a highly doped tunnel junction for series interconnection of subcells thus introducing parasitic absorption (b) Proposed tandem cell eliminates tunnel junction through sequential bonding of subcells.

5.2 Tandem cell without tunnel junction

To address these challenges, this work demonstrates tandem TPV cells with optical performance that exceeds that of their single-junction air-bridge counterparts[19,115,117,119]. The tandems shown here are fabricated by stacking individual air-bridge cells via a cold-welding process as shown in Figure 5.1b. Instead of uniform tunnel junctions, as used in conventional, monolithic III-V multi-junction cells, a patterned metal grid is used as the junction between the top and bottom subcells. This middle grid also serves to bond the subcells together using a low-temperature Au-Au thermo-compression step and can be readily used as a common terminal in a multi-terminal configuration to overcome the limitations of two-terminal multi-junction devices. It is important to note that the tandem cells in this study differ from the ones realized through mechanical stacking technique, which connects subcells using glues, transparent conductive oxides (TCO), or metal nanoparticles[167–172]. Compared to the air-bridge integration, those techniques introduce parasitic absorption of both in-band and out-of-band photons and lead to increased series resistance, poor heat tolerance, and debonding owing to UV radiation deterioration of the adhesive material[167–172].

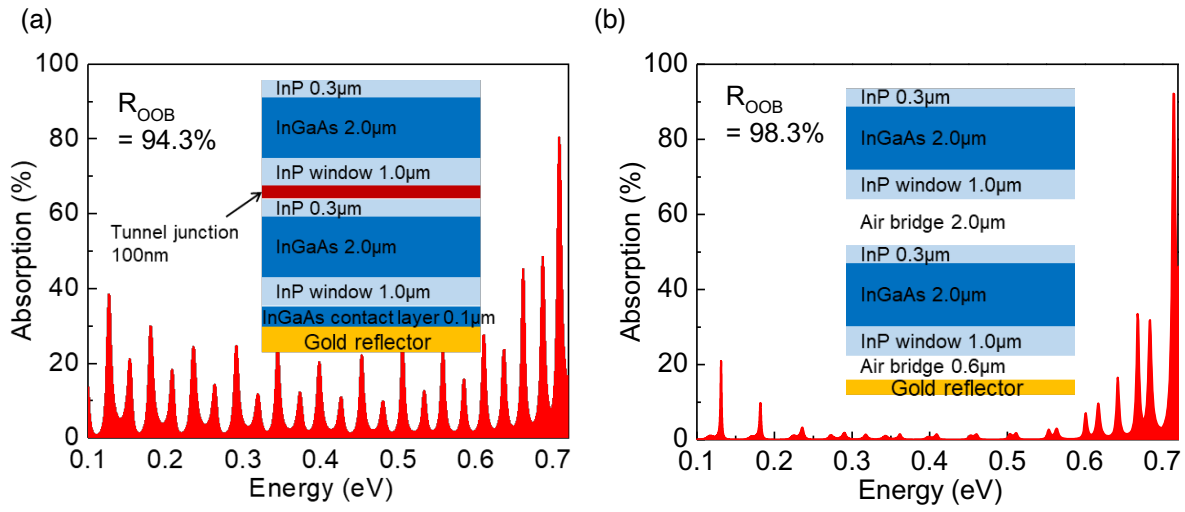

Figure 5.2 Optical simulation of (a) conventional and (b) dual air-bridge tandem TPV.

Using preliminary optical simulation that assumes no photon loss in semiconductors as shown in Figure 5.2, we show that the tandem cells with tunnel junction (TJ) experience losses from photon dissipation through free carrier absorption (FCA). This leads to an out-of-band reflectance of 94.3% (Figure 5.2a) which is similar to experimentally demonstrated tandems in literature[4,27,28,173]. This compromise undermines the potential benefits associated with a tandem setup designed for high output power. Notably, the absorption model in the TJ uses the Drude model for computation of extinction coefficients in heavily-doped III-V semiconductors[122]. By eliminating the tunnel junction, we can circumvent a loss in R_{OOB} exceeding 4% (Figure 5.2b), leading to an enhanced spectral efficiency approaching 80%.

Overall, this dual air-bridge architecture offers several advantages over existing multi-junction TPV cells. One advantage is that it reflects nearly all the radiation that is not absorbed within the active layers of the top and bottom cell. Another important advantage is that a multi-terminal configuration mitigates the current-matching constraint which limits performance as the spectrum

shifts[17,18]. Together, these two advantages combine to allow the emission temperature to shift by 600ºC while maintaining an average efficiency within 37% of the peak efficiency. The third advantage is that sequential bonding allows straightforward integration of dissimilar materials (e.g., III-Vs and Silicon) or materials grown on different substrates (e.g., GaAs and InP)[174], which provides additional flexibility when optimizing tandems for cost and/or performance.

5.3 Fabrication of dual air-bridge tandems

Figure 5.3 illustrates the iterative steps of cold welding and epilayer liftoff (ELO) employed in the fabrication of a dual air-bridge tandem. The air-bridge bottom cell is prepared through a cold welding (2) and ELO processes (3), in accordance with our prior work[19,117,119]. The top epilayer is transferred by repeating the cold welding (5) and ELO (6) processes. To mitigate the susceptibility of the thin-film membrane in the bottom cell to cracking, a relatively low weld bonding temperature (150°C) and a bonding pressure of 3 MPa are applied. Specifically, this second level of cold weld bonding requires optical alignment of the metal gridlines on the subcells using a flip-chip bonder. The metal grid layer comprises adhesive metal (Titanium), where the distinct thermal expansion coefficients of materials disrupt the formation of a uniformly bonded gold surface. Thus, we minimize the thickness of the adhesive layer to 10 nm. After the bonding, the middle metal grid has a double metal stack of Ti(10 nm)/Au(300 nm)/Au(300 nm)/Ti(10 nm).

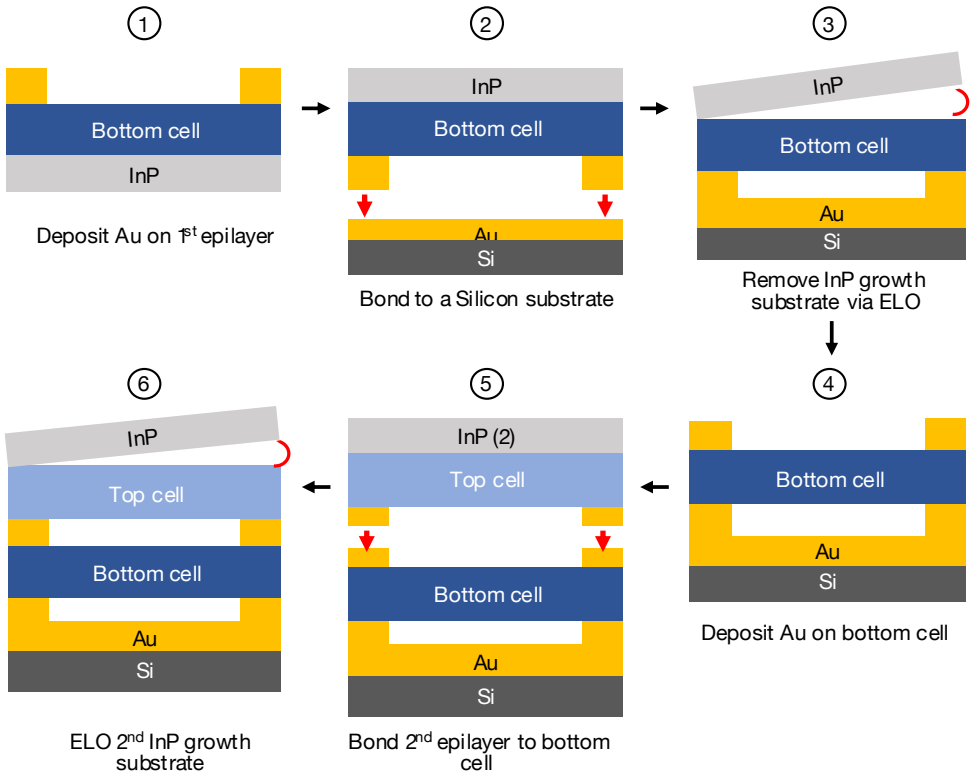

Figure 5.3 Illustrations of the cold-welding and epilayer liftoff (ELO) processes for bottom and top cells.

Importantly, the gold surfaces are meticulously preserved to ensure they remain free from oxidation, thereby ensuring the success of the welding process. Finally, the dual air-bridge tandem shown in Figure 5.4a is achieved through the wet-etching process employed for TPV mesa patterning. In the tandem configuration, the bottom cell consists of a 2-µm-thick 0.74 eV InGaAs absorber layer. The bandgap of the top cell is varied to showcase two configurations: 0.74 eV/0.74 eV InGaAs homo-tandem and 0.9 eV/0.74 eV InGaAsP/InGaAs hetero-tandem cells, respectively. It is important to note that the chemical wet etchant differs between InGaAsP and InGaAs, while maintaining consistency in other fabrications procedures. Detailed information on the epilayer is described in chapter 3 of this dissertation.

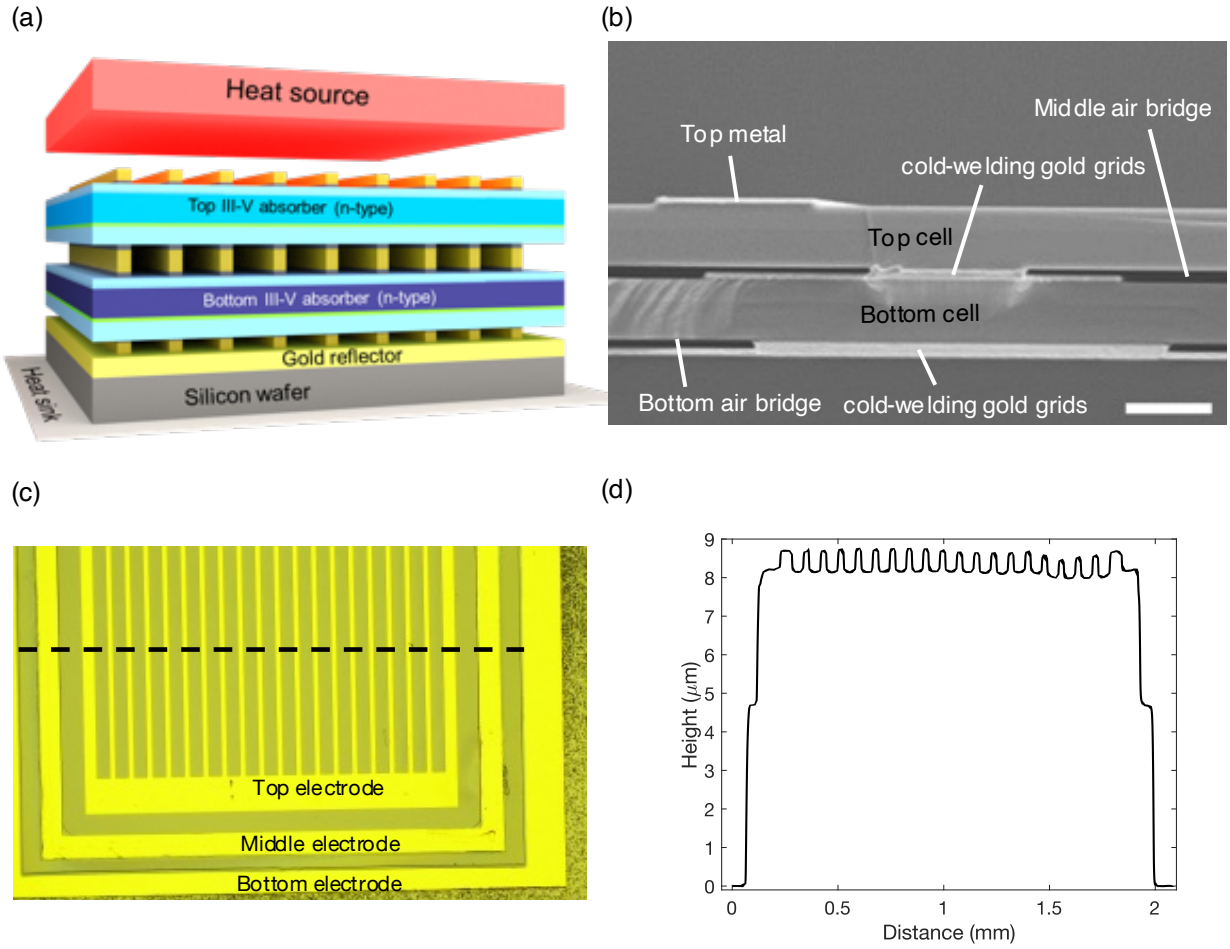

Figure 5.4 Dual air-bridge TPV structure enabled by sub-cell cold-welding. (a) Schematic of the tandem TPV system consisting of a heat source and an air-bridge tandem TPV cell attached to a heatsink. The top and bottom cells are cold-welded using the middle grid (b) Cross-sectional scanning electron microscope (SEM) image of a dual air-bridge tandem TPV cell. Scale bar, 5 μm. (c) Optical microscopy image of a fabricated tandem cell (d) Measured profilometry across the surface of the tandem cell (black line in c).

Figure 5.4a shows the general architecture of a dual air-bridge tandem. In place of a tunnel junction, the metal grid in the middle layer serves as a junction between the top and bottom subcells, obviating the need for lattice-matching for tandem partners. The three layers of gridlines are optically aligned, optimizing the geometrical fill factor (GFF), defined as the ratio of the metal gridline area to the total device area. Moreover, the three metal layers can operate independently, offering the flexibility to choose either 2T or multi-terminal configurations. The dual air bridges

are integrated within the tandem structure, with the middle air bridge facilitating lossless heat transfer between subcells. In Figure 5.4b, the cross-section scanning electron microscope (SEM) image of a dual air-bridge tandem cell shows that the semiconductor membranes are mechanically supported by gold gridlines with no discernible compressive deformation or buckling[119]. Figure 5.4c shows an optical microscopy view of the tandem cell's surface, including the top, bottom, and common (middle) electrodes. We further highlight the relative flatness of the gridlines with a profilometry measurement, as shown in Figure 5.4d.

5.4 Performance quantification of tandem cell

5.4.1 Spectral splitting in TPV subcells

The in-band (IB) absorption in the top cell is calculated using the following equation:

$$A_{\mathrm{IB,Top}} = \int_{E_{\mathrm{g,Top}}}^{\infty} \alpha_{\mathrm{Top}} \times E \times \Phi_{\mathrm{B}}(E, T_{\mathrm{h}}) \mathrm{d}E, \tag{5.1}$$

where α_{Top} is the top cell absorption coefficient calculated by the transfer method matrix and Φ_{B} the spectral photon flux of the heat source. The absorption in the bottom cell follows by:

$$A_{\mathrm{IB,Bot}} = \int_{E_{\mathrm{g,Bot}}}^{\infty} \alpha_{\mathrm{Bop}} \times E \times \Phi_{\mathrm{B}}(E, T_{\mathrm{h}}) \times \frac{\Theta_{\mathrm{in},2}}{\Theta_{\mathrm{in},1}} \mathrm{d}E, \tag{5.2}$$

where α_{Bot} is the bottom cell absorption coefficient and $\Theta_{\mathrm{in},1}$ and $\Theta_{\mathrm{in},2}$ are the input powers to the top and bottom cells, respectively. The $\Theta_{\mathrm{in},2}$ is identical to the heat energy transmitted through the top cell. The $\Theta_{\mathrm{out},2}$ generates additional absorption in the top cell, but the amount is much less than 1%, so it is negligible. The absorption is calculated by:

$$A_{\mathrm{IB,Top2}} = \int_{E_{\mathrm{g,Top}}}^{\infty} \alpha_{\mathrm{Bop}} \times E \times \Phi_{\mathrm{B}}(E, T_{\mathrm{h}}) \times \frac{\Theta_{\mathrm{out},3}}{\Theta_{\mathrm{in},1}} \mathrm{d}E. \tag{5.3}$$

The boundary between the in-band (IB) and out-of-band (OOB) regions indicates the band edge of an absorber material, estimated to be 0.02 eV away from the nominal bandgap of 0.74 eV.

5.4.2 Spectral efficiency in tandem TPV cell

The spectral efficiency is calculated using the following equation:

$$\mathrm{SE} = \frac{E_{\mathrm{g,top}} \int_{E_{\mathrm{g,top}}}^{\infty} \varepsilon_{\mathrm{eff,top}}(E) \times \Phi_{\mathrm{B}}(E, T_{\mathrm{h}}) \mathrm{d}E + E_{\mathrm{g,bot}} \int_{E_{\mathrm{g,bot}}}^{\infty} \varepsilon_{\mathrm{eff,bot}}(E) \times \Phi_{\mathrm{B}}(E, T_{\mathrm{h}}) \mathrm{d}E}{\int_{0}^{\infty} \varepsilon_{\mathrm{eff,T}}(E) \times E \times \Phi_{\mathrm{B}}(E, T_{\mathrm{h}}) \mathrm{d}E}, \tag{5.4}$$

where $\varepsilon_{\mathrm{eff,T}}(E) = \frac{(1-R_{\mathrm{e}})A_{\mathrm{c,T}}}{1-R_{\mathrm{e}}(1-A_{\mathrm{c,T}})}$ is the effective emissivity of the cavity formed by the emitter and the tandem cell, where R_{e} and $R_{\mathrm{c,T}}$ are the spectral reflectance of the emitter and the tandem cell, respectively. In the same manner, $\varepsilon_{\mathrm{eff,top}}(E) = \frac{(1-R_{\mathrm{e}})A_{\mathrm{c,top}}}{1-R_{\mathrm{e}}(1-A_{\mathrm{c,top}})}$ and $\varepsilon_{\mathrm{eff,bot}}(E) = \frac{(1-R_{\mathrm{e}})A_{\mathrm{c,bot}}}{1-R_{\mathrm{e}}(1-A_{\mathrm{c,bot}})}$, where $A_{\mathrm{c,top}}$ and $A_{\mathrm{c,bot}}$ are the absorptance for the top and bottom cells in the tandem structure, respectively.

5.4.3 Fourier transform infrared measurements

Microscopic reflectance measurements on the TPV samples were performed using a Cary 670-IR spectrometer with a Cary 620 IR microscope (Agilent Technologies, CA), equipped with globar near- and mid-IR sources and a 15× objective. The samples were measured with the liquid nitrogen-cooled detector of a 128 × 128 MCT focal plane array. All data were collected at a 1 cm^{-1} spectral resolution.

5.4.4 External quantum efficiency measurements

EQE measurements are conducted with monochromatic illumination, chopped at 200 Hz, and directed into a multimode SMA fiber connector to a bare fiber optic patch cable (M118L02, Thorlabs) set at a 15° angle to the TPV cells. The output signal is monitored and collected by a SR830 lock-in amplifier. Calibration of the illumination power is performed using a 818-UV/DB Si detector (Newport) from 400 nm to 900 nm, a 818-IG InGaAs detector (Newport) from 900 nm to 1,650 nm, and a FDG03 Ge detector (Thorlabs) from 1,650 nm to 1,800 nm.

5.4.5 View factor calibration

The view factor F_v is determined from the measured J_{ph} according to:

$$J_{ph} = F_v \cdot q \cdot \int_{E_g}^{\infty} \varepsilon_{eff}(E)/\varepsilon_c(E) \cdot EQE(E) \cdot \Phi_{\mathrm{B}}(E,T_{\mathrm{h}})\, dE \tag{5.5}$$

where EQE is the measured external quantum efficiency in Fig 2, $\varepsilon_{eff}(E) = \frac{\varepsilon_h \varepsilon_c}{\varepsilon_h + \varepsilon_c - \varepsilon_h \varepsilon_c}$ is the effective emissivity of the emitter-cell pair (ε_h is the emissivity of the emitter, and ε_c is the emissivity/absorptivity of the cell). The calculated apparent view factors are 0.34 and 0.33 for the homo- and heterotandem devices, respectively.

5.4.6 Electrical characterization

The TPV samples were mounted on a copper plate coupled with a closed-loop water chiller, maintaining the temperature at 20°C[19,125]. Using a three-axis translational stage, a SiC globar emitter (SLS203, Thorlabs Inc.) was centered on the sample and moved up and down to control the distance. The emitter spectral emissivity (ε_e) is calibrated by referencing to a true blackbody

source (IR-564, Infrared Systems Development Corp.). The black body shows $\varepsilon_e > 0.99$, whereas the ε_e of the SiC emitter was measured to be 0.96. Finally, the current density-voltage curves were characterized using a Keithley 2401 Source Measure Unit in the 4-wire sensing mode.

5.5 Photon recovery and utilization in tandem cells

Figure 5.5a depicts the measured optical properties of the homo-tandem cell, obtained using Fourier transform infrared radiation (FTIR) spectroscopy and weighted to a 1500K blackbody radiation. The FTIR measurement yields a R_{OOB} of 96.4% yielding a loss of 3.6%. Notably, out-of-band losses (yellow region), exceeding those predicted by the simulations discussed above, are attributed to FCA arising from scattering sources of phonons and ionized impurities[175]. Absorption by defects near the band edge (assume the band tail 25 meV below from the band edge) is less than 0.3%. On the other hand, FCA by free charges and impurities contributes significantly, accounting for 3.3%. The calculated spectral efficiency (*SE*) for this cell is 68.4%. In contrast, for a comparable monolithic tandem featuring a tunnel junction and a planar back surface reflector, the theoretical R_{OOB} is 93.2% with a *SE* of 62.3%. These simulations are consistent with experiments[4,27,28,176] on monolithic tandems with highly doped tunnel junctions.

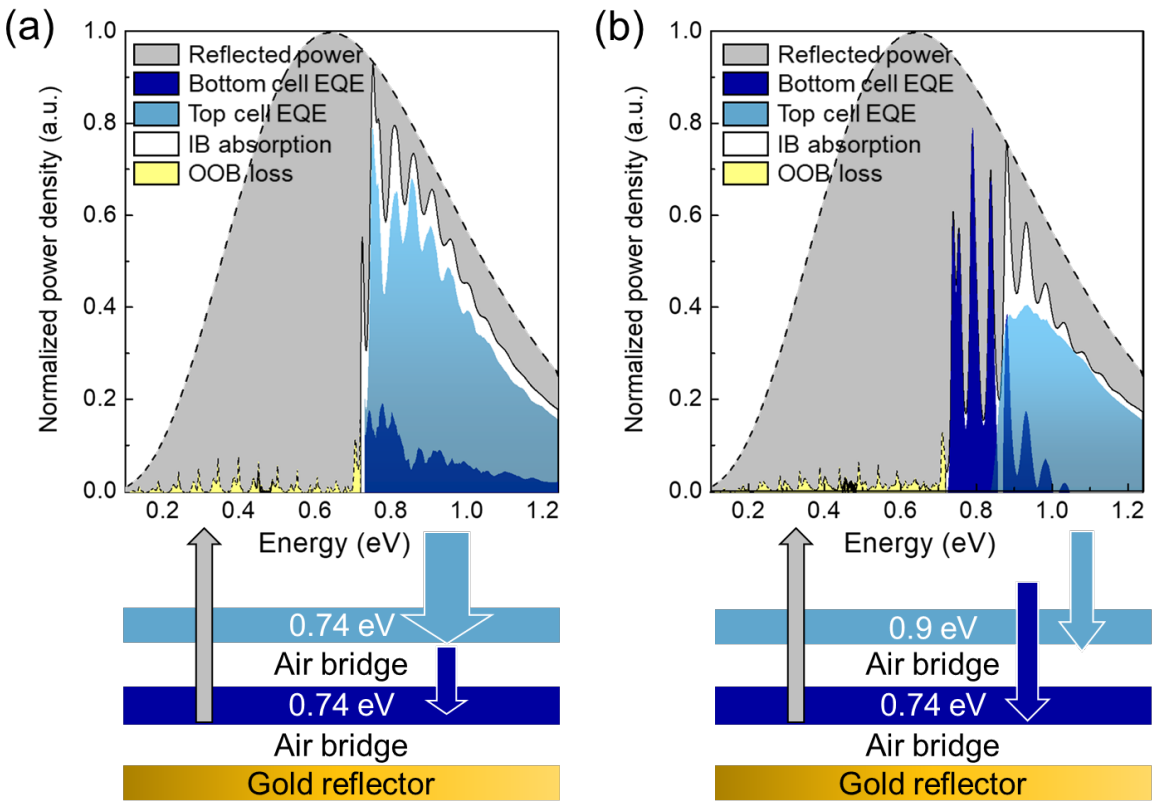

Figure 5.5 Photon utilization in the homo- and hetero-tandem TPV cells. a. and b. Spectral power breakdown in the homo- and heterotandem cell, respectively. The dashed line denotes the incident 1223°C blackbody spectrum. EQE measurements for individual subcells reveal spectral splitting in each tandem cell. In-band (IB) absorption and out-of-band (OOB) loss are characterized via FTIR spectroscopy at wavelengths of 1.0–15.5 µm. The optical cavities formed by the semiconductor membranes, the Au reflector, and two air gaps lead to the interference features.

Figure 5.5a shows the measured absorption spectrum and external quantum efficiency (EQE) of the InGaAs homotandem cell. The top and bottom cells absorb 61% and 10% of the incident in-band light, respectively. When weighted to a 1223°C blackbody illumination source, the out-of-band reflectance is 96.4%, which corresponds to a parasitic out-of-band absorption of $A_{OOB} = 3.6\%$. Out-of-band losses (depicted by the yellow shaded region), exceeding those predicted by simulations, are mostly attributed to FCA stemming from residual background carriers[175].

Absorption by defects near the band edge contributes $A_{OOB} < 0.3\%$, while FCA by free charges and impurities accounts for 1.4%. The calculated spectral efficiency (*SE*) for this tandem is 68.4% which is comparable to its single-junction counterpart. For context, a representative monolithic tandem featuring a tunnel junction and gold back surface reflector (AuBSR) as in Fig. 5.2a shows a calculated $SE = 62.3\%$. The measured absorption and EQE of the heterotandem cell are presented in Figure 5.5b. The use of two different bandgaps leads to more balanced absorption than in the homotandem. For example, under 1223°C illumination, the top and bottom subcells absorb 33% and 38% of the in-band spectrum, respectively. The cell achieves $R_{OOB} = 97.2\%$, which is 0.8% higher than for the homotandem, consistent with the simulation. Absorption by defects near the band edge contributes $A_{OOB} = 0.1\%$, while FCA accounts for 1.4%. The combination of high R_{OOB} and lower thermalization losses yields a simulated $SE = 78\%$ at 1223°C. Considering the increased parasitic absorption observed in the experiment, the *SE* decreases to 74%. Nonetheless, the addition of the 0.9 eV top cell enhances the *SE* by >4% relative to both the 0.74 eV single-junction and homotandem air-bridge cells. Overall, these results highlight the photon-utilization advantages offered by the dual air-bridge tandem design.

5.6 Conversion efficiency of homo-tandem device

In addition to the traditional series-connected two-terminal (2T) configuration, the dual air-bridge cells can be operated in a multi-terminal configuration when the metal-grid junction is used as an additional electrode. Figure 5.6a shows the current-density *versus* voltage (*J-V*) characteristics for the 2T homo-tandem cell and for the top and bottom subcells individually at a representative temperature of 1120°C. Figure 5.6b shows that the short-circuit current rises with increasing emitter temperature, with the top cell producing more at all irradiations. This is because, in a homo-

tandem device, the top cell absorbs the majority of the incident radiation, resulting in significant disparities in current output. This also causes the top cell to produce more output voltage than the bottom cell at the same emitter temperature, as illustrated in Figure 5.6c. However, at the same photocurrent, the top and bottom cells yield similar output voltages, implying similar material and fabrication quality. The open circuit voltage in the 2T tandem is equivalent to the sum of the voltages generated in the individual subcells. Complete experimental data and electrical parameters such as the fill factor (FF) and maximum power point (P_{MPP}) are provided in appendix B of this dissertation.

The TPV efficiencies shown in Figure 5.6d are calculated by taking the ratio of the maximum power produced to the heat absorbed by the cell (incident minus reflected). The power outputs and efficiencies are presented for the 2T configuration and the multi-terminal arrangement (ΣT) which is the sum of the individual power outputs of the top and bottom cells. ΣT represents an upper bound for what can be achieved in a multi-terminal configuration[177–179] since demonstration of 3T and 4T arrays is beyond the scope of this dissertation. The efficiency of the 2T homo-tandem cell peaks at 18.2 ± 0.1% under 1120°C irradiation. The large current mismatch between the individual subcells produces substantial electrical losses. The ΣT configuration, in comparison, allows each cell to operate at its respective maximum power point, resulting in a peak efficiency of 37.8 ± 0.2% under 1265°C irradiation. This result also represents a 2% absolute improvement over a 0.74 eV single-junction air-bridge cell at comparable emitter temperatures. At higher emitter temperatures, the efficiency drops off due to series resistance (R_s) losses, which decreases the fill factor (see appendix B). The relatively high R_s for the bottom cell is attributed to the unoptimized contact resistance within the middle grid. Future iterations will include Pt[180] in the p-type contact

layer to lower contact resistance of the intermediate gridlines. Predictions show that improvements to series resistance can lead to an efficiency of 46% at higher emitter temperatures for the ΣT homo-tandem.

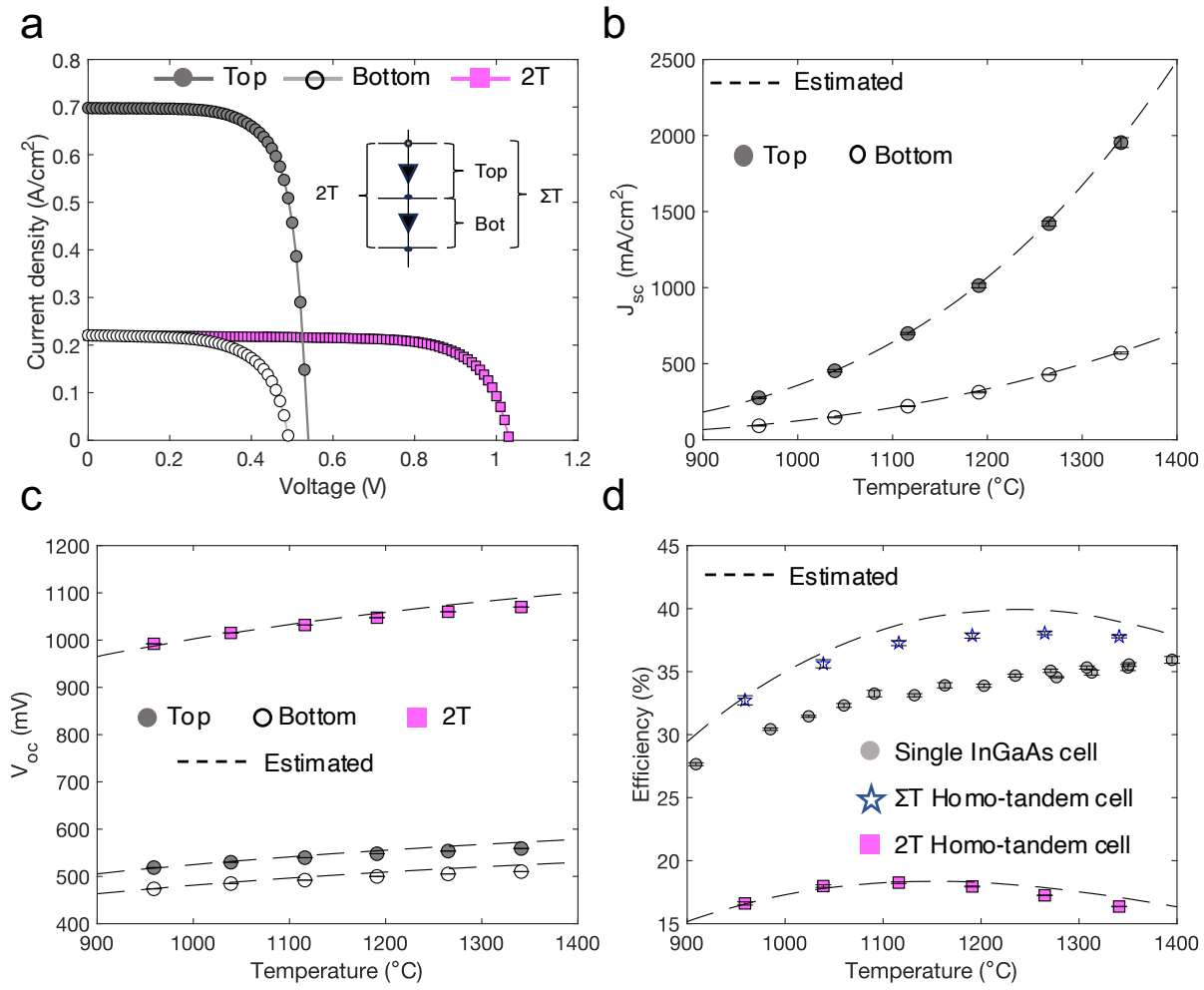

Figure 5.6 Performance quantification of the homo-tandem device. a, Current-voltage measurements under 1120°C irradiation. **b,** Short-circuit current density (J_{sc}) produced and **c,** Open-circuit voltage (V_{oc}) of the tandem and subcells as a function of emitter temperatures. **d,** Power conversion efficiency as a function of emitter temperatures in both 2T and multi-terminal configuration.

5.7 Conversion efficiency of hetero-tandem device

Figures 5.7a shows the *J-V* characteristics for the 2T hetero-tandem and its subcells individually at a representative temperature of 1155°C. Figure 5.7b highlights the short-circuit current produced by the top and bottom cells of the hetero-tandem. Unlike the homo-tandem, the subcells operate in different spectral bands. This results in comparable short-circuit current density, thus minimizing spectral mismatch. The open-circuit voltage of the 0.9 eV top cell is ~100 mV larger than that of the 0.74 eV bottom cell at the same emitter temperatures as shown in Figure 5.7c. At higher emitter temperatures, the individual sub-cells have comparable bandgap-offset voltages (*i.e.*, the difference between the bandgap and V_{oc}), approaching 220 mV. The V_{oc} in the 2T configuration is equivalent to the sum of the V_{oc} in the top and bottom subcell leading to an offset voltage of ~450 mV. Differences between the experimental markers and the model predictions (called estimated) at high temperatures may be attributed to cell heating effects.

The efficiencies of the 2T and ΣT hetero-tandem, shown in Figure 5.7d, are comparable at emitter temperatures above 1300°C. At those temperatures, the incident spectrum is almost evenly split between the absorption bands of the top and bottom cells, which minimizes current mismatch and reduces the benefits of the multi-terminal configuration. Both the 2T and multi-terminal arrangement of the hetero-tandem have a peak efficiency of 39.1 ± 0.2% at 1330°C.

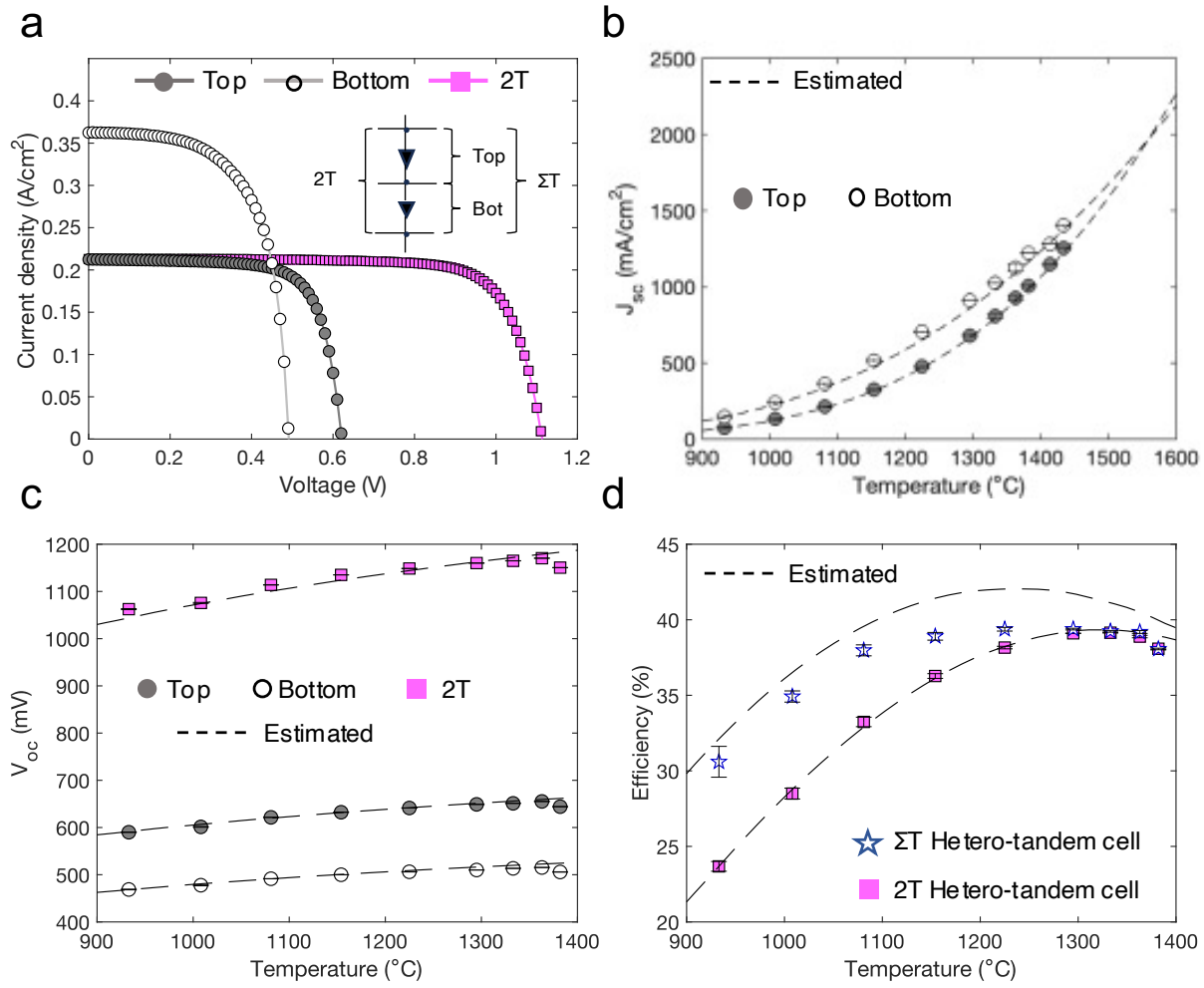

Figure 5.7 Performance quantification of the hetero-tandem device. a, Current-voltage measurements under 1155°C irradiation. **b,** Short-circuit current density (J_{sc}) produced and **c,** Open-circuit voltage (V_{oc}) of the tandem and subcells as a function of emitter temperatures. **d,** Power conversion efficiency as a function of emitter temperatures in both 2T and multi-terminal configuration.

5.8 Sensitivity to emission temperatures

Figure 5.8a illustrates that realistic improvements to series resistance (R_s = 15 mΩ-cm^2) can lead to efficiencies >45% for the ΣT heterotandem, at the same time shifting the performance towards higher emitter temperatures. We emphasize that the reduced sensitivity to emitter temperature is achieved by the combination of high R_{OOB} and the multiterminal configuration enabled by the dual

air-bridge tandem as shown in Figure 5.8b. A low temperature sensitivity is significant in the context of grid-scale electrical storage employing thermal batteries since it allows grid operators to widen the temperature differential within the storage medium, enabling actions such as discharging the thermal battery temperature to as low as 1000°C during periods of high demand, while incurring only marginal efficiency losses. This capability, in turn, has the potential to reduce the required amount of storage material.

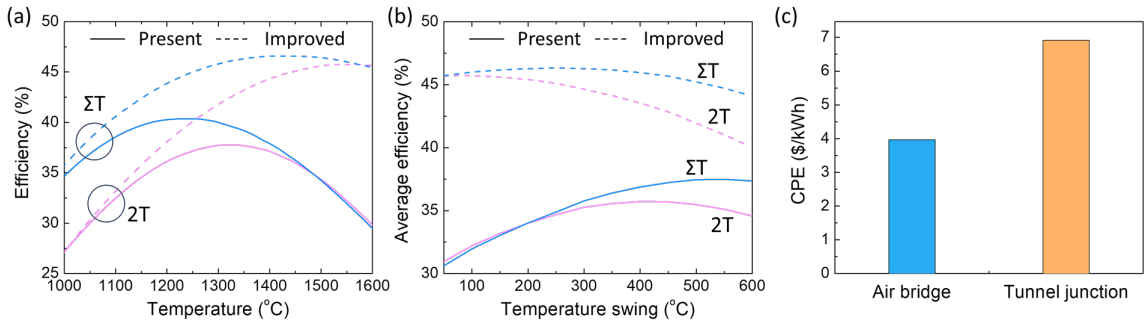

Figure 5.8 Power conversion efficiency in a thermal battery. a, Present day efficiency of the air-bridge heterotandem (solid lines) versus emitter temperature, and that expected with reduction in cell series resistance to 15 mΩ-cm^2 (dashed lines). **b,** Average efficiency as a function of temperature swing during the cooling phase, assuming an initial storage temperature of 1600°C. The multi-terminal configuration has lower sensitivity to spectral variations during the wide temperature discharge of thermal batteries. **c,** Estimated cost of graphite per unit energy (CPE), comparing the air-bridge heterotandem to an analogous tunnel-junction tandem device. This calculation assumes a 600°C temperature swing with a $0.5/kg cost of graphite.

To illustrate the impact of the extended temperature range, we calculate the cost per unit energy (CPE) of the graphite energy storage medium. The CPE is the cost per kg of graphite (US $0.5/kg[181]) divided by the energy stored per mass, which is given by the integral of the graphite heat capacity and the TPV efficiency over the range of emitter temperatures encountered during the cooling/discharge phase. Figure 5.8c shows that the use of an air-bridge tandem lowers the CPE by approximately 50% compared to an analogous tunnel-junction tandem, from 6.91/kWh to $3.96/kWh at a temperature swing of 600°C. These CPE reductions should translate to other

energy storage components of thermal batteries, including insulation, since the cells govern the denominator of the CPE. The calculation assumes a 600ºC graphite temperature swing and that the cells have the same electrical cell parameters (*i.e.*, shunt and series resistances, dark current densities). Although the tandem air-bridge process requires separate wafers to grow each sub-cell, the differential cost associated with this approach can almost entirely be mitigated using non-destructive epitaxial lift-off which allows for multiple reuses of the growth wafer[182–184]. Therefore, the potential to substantially lower the overall CPE, while maintaining comparable cost per power (CPP), suggests that air-bridge tandems can play a key role in the broad deployment of economical thermal batteries for long-duration grid-scale electrical storage.

5.9 Conclusions

In summary, we have successfully demonstrated air-bridge III-V tandem TPV cells fabricated through low-temperature cold welding engineering using individual III-V single cells, eliminating the need for tunnel junctions. Through the incorporation of two air bridges and a multiterminal configuration, these tandem cells achieve lossless power transmission between subcells, thereby optimizing electrical output power. We experimentally achieved a total R_{OOB} of 97.2%, accompanied by a higher P_{MPP} when operated in a multi-terminal configuration compared to a two-terminal tandem operation. As a result, a single 0.74 eV InGaAs air-bridge cell showed 36.0% efficiency, while the air-bridge tandem cells achieved 37.8% for the 0.74/0.74 eV and 39.3% for the 0.90/0.74 eV tandem cells, respectively. This innovative approach to the air-bridge tandem structure is anticipated to stimulate further cell optimization with a low temperature sensitivity, paving the way for the development of cost-effective, high-power density, and highly efficient TPV cells.

Chapter 6: Conclusions and Future Directions

To realize large improvements in TPV efficiencies, the key is to have efficient recuperation of unusable low-energy photons. This thesis explores the use of new cell-side architectures to recycle/recuperate these low-energy photons to improve the performance of TPVs for different emerging power generation technologies. The first work seeks to experimentally understand the limitations of an air-bridge architecture, which leverages refractive index mismatch to achieve near-perfect reflectance of low-energy photons. The second work utilizes the air-bridge architecture with three absorber bandgaps ranging from 0.74 eV to 1.1 eV to demonstrate a record high efficiency. The third work demonstrates transmissive spectral control as an approach for achieving wavelength-selective radiative transfer in thermophotovoltaic systems that has the potential to overcome the limitations of emissive and reflective methods. Lastly, this thesis introduces a new approach to realizing tandem TPV cells with high photon management. This approach eliminates the need for a tunnel junction by using highly reflective metal grids that covers ~10% of the area to connect the top and bottom cells.

This closing chapter outlines numerous potential approaches for enhancing the adoption of TPVs in various energy generation applications, including thermal energy storage, waste heat recovery, and combined heat and power generation.

6.1 Si-based tandem TPV

As mentioned in chapter 5 of this thesis, the utilization of III-V multijunction cells presents a viable approach to optimizing the performance of thermophotovoltaic systems. Nevertheless, the cost of III-V semiconductors is significantly higher than materials like silicon. From a cost perspective, replacing one or more of the sub-cells in the tandem stack with more affordable materials such as Si and Ge would be desirable. Silicon stands out as a highly promising material with a wide bandgap, significant technological advancements, and cost-effectiveness.

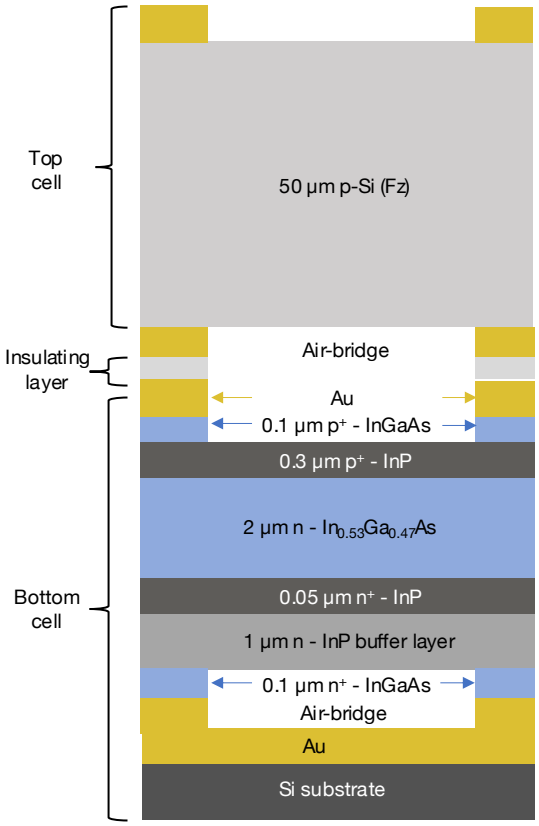

Figure 6.1 Silicon based multijunction cell. The top (Si) cell and bottom (InGaAs) cell will be prepared separately and the sequentially bonded to form the proposed structure.

In a recent study, my colleagues, Byungjun Lee and Rebecca Lentz, successfully demonstrated an air-bridge single junction Si TPV with an out-of-band reflectance of 98.0% when weighted to a

1500K blackbody emitter[117]. This led to a maximum conversion efficiency approaching 20%. With near-term improvements, Si TPV can attain a conversion efficiency of 40%. By incorporating Si into one of the sub-cells, as depicted in Figure 6.1, it becomes feasible to reduce the cost of the multi-junction by approximately 50% while preserving its high spectral management and conversion efficiency. This stack includes a float-zone double side polished silicon as the top cell, which allows unabsorbed photons to pass through to the bottom InGaAs cell. With preliminary analysis using transfer matrix methods, it is evident from Figure 6.2a that we can still maintain a high out-of-band reflectance exceeding 98%. Figure 6.2b also illustrates the spectral splitting between the Si top cell and InGaAs bottom cell, indicating a similar distribution of photons across various wavelengths. Additional work should focus on optimizing the electrical performance of the Si top cell to maximize conversion efficiency.

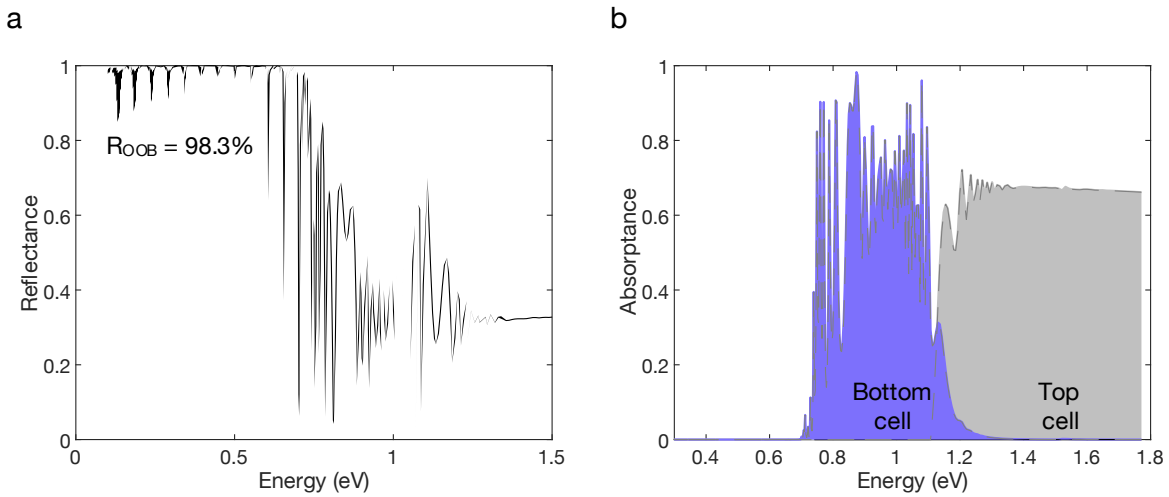

Figure 6.2 Optical performance of a silicon based tandem cell. (a) Modeled reflectance of the proposed Si-InGaAs tandem showing an out-of-band reflectance of 98.3%. **(b)** Simulated spectral utilization in the tandem structure.

6.2 Improving fabrication

It is critical to optimize yield during the fabrication process of thermophotovoltaic cells in order to enhance overall efficiency, reduce cost, promote advancement in technology, minimize environmental impacts, guarantee market competitiveness, and improve the dependability of TPV systems. A few potential avenures to improve fabrication yield are described below.

6.2.1 Variation in bonding scheme

A conventional wafer-bonder is used to complete the bonding process. Preliminary testing has shown that this procedure can provide placement accuracy within acceptable tolerances (<3 μm). However, the use of a flip-chip bonder is not ideal for process scale-up and can lead to non-negligible sample-to-sample variability (~30 μm tolerance). In the presence of lateral misalignment ≥10μm, the 10 μm grid lines will not come into sufficient contact as shown in Figure 6.3. In the presence of lateral misalignment exceeding 10μm, the 10μm wide grid lines on each surface will not come into sufficient contact for bonding, resulting in suspension failure.

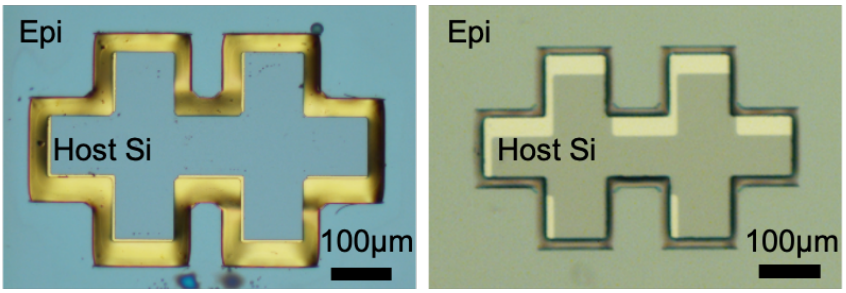

Figure 6.3 Top view image of fiducial marks on sample surface indicating spatial misalignment during flip chip bonding. The left (right) image shows tolerable (intolerable) misalignment for the described fabrication procedure.

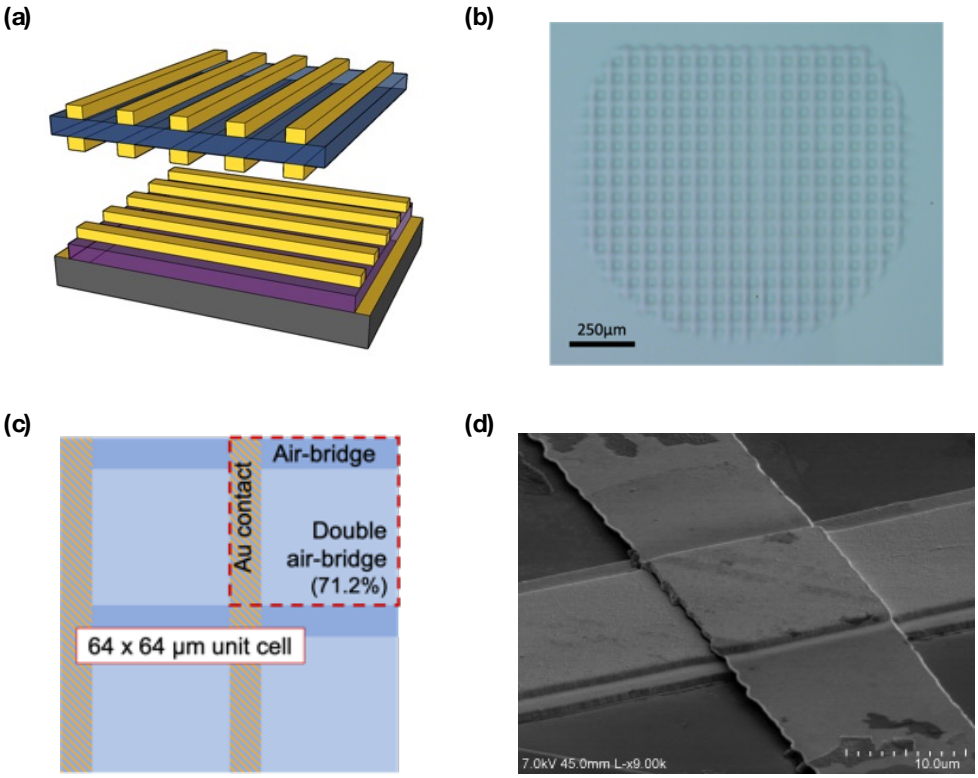

Figure 6.4 Perpendicular intermediate grid is formed by bonding top gridlines at 90º w.r.t. bottom gridlines. (a) Bonding schematic. (b) Top-view image of an InGaAs epilayer supported by a perpendicular grid on top of a Si handle, demonstrating a key step in the fabrication of dual-ABCs. (c) Schematic of 2D intermediate grid enabling double air-bridge design. (d) SEM showing demonstrated bonding region of the perpendicular grid.

To mitigate the misalignment risk and enable process scale-up, we have developed an alternative design where the grid lines on the top cell are rotated by 90º with respect to those on the bottom, allowing for the use of a conventional wafer bonder. As shown Figure 6.4a and 6.4b, vertically oriented Au-insulator-Au lines are deposited on the bottom cell, while horizontally oriented Au lines are deposited on the top cell. Au-Au bonding occurs at the intersections of these orthogonal gridlines. Preliminary testing shows that the resulting suspension exhibits excellent mechanical stability. The perpendicular intermediate grid design can tolerate much larger misalignments (on the order of ~100 µm) without impacting performance. Such tolerances can be achieved in a simple

and high-throughput way by dicing the substrate (carrying the top cell) and Si handle (carrying the bottom cell) to specification and then aligning them along two edges. Although the perpendicular grid shades a portion of the bottom cell as in Figure 6.4c (~10-15%), those areas effectively function as efficient single-junction top ABCs that convert high energy photons into power and reflect/recycle ~99% of the low energy photons back to the heat source. Thus, shadowing is expected to have a negligible impact on the total cell efficiency. In fact, in high temperature regimes where series resistance losses dominate, some shadowing can improve efficiency because it lowers the current density while preserving the incident spectrum.

6.2.2 Alternative mechanical supports

The air-bridge is made of a free-standing semiconductor with thickness in the order of a wavelength. These thin-film membranes are susceptible to strain (buckling), which causes mechanical distortion and structural failures such as cracks[119]. This buckling not only causes failures, but it also supports a variety of optical modes, which increases parasitic absorption. My collaborator, Jihun Lim, introduced a transparent InP epitaxial layer to mitigate this problem by stiffening the membrane, resulting in flat cavities that can only support one mode[119]. Alternative stiffening methods may involve the use of less expensive transparent dielectric materials with similar or better mechanical stiffness compared to InP as shown in Figure 6.5a. Candidate dielectric materials may include high quality SiO2, MgF2, parylene-C, ZnSe and many others. Preliminary optical modeling (see Figure 6.5b) shows that the addition of these materials has negligible effect on the out-of-band reflectance. However, future work should investigate the trade-off between mechanical robustness and high reflectivity in the out-of-band range.

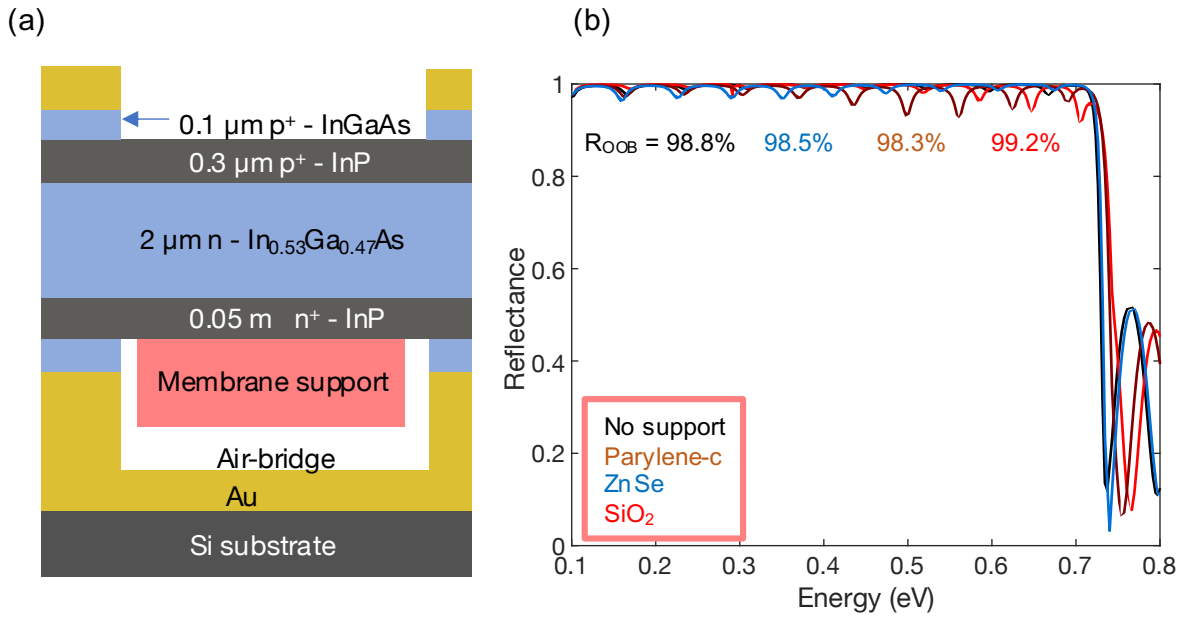

Figure 6.5 Dielectric materials as mechanical support. (a) Schematic of a single junction air-bridge cell with a membrane layer for mechanical support (b) Optical simulation demonstrates that the addition of various high-quality dielectric layers, such as ZnSe, SiO2, and parylene-c, has no substantial influence on out-of-band reflectance (R_{OOB}) when compared to a cell without membrane support.

6.3 Modules

In order to achieve high volume production of TPVs, it would be necessary to connect individual cells into modules in a series configuration. Manufacturing TPV modules at a higher volume than present lab-scale manufacturing can lead to cost advantages[58]. The incorporation of these individual cells into modules will result in extra inefficiencies associated with series resistance, non-functional cell area, parasitic absorption, wire losses, and thermal management. Here, a preliminary modularization scheme is proposed to mitigate these challenges. To form modules, strings of cells can be connected using the scheme in Figure 6.6 (shown here is a 2-by-4 cm array suitable for testing). This 4T interconnection scheme provides independent series-interconnection of top and bottom cells and utilizes all the sub-cells with no end losses (unlike the 3T scheme).

The interconnects (ICs) can be deposited and lithographically patterned directly on the Si handle as shown in Figure 6.6T,B using standard, high-volume semiconductor tools. The Si handles can be attached to high-thermal conductivity Direct Bond Copper (DBC) substrates, which are in turn soldered onto copper heat sinks. DBCs are a reliable platform because they have a similar coefficient of thermal expansion as Si. A key feature of the proposed modules is that all radiation-facing surfaces have very high IR reflectance (≥98%). This makes it possible to achieve a module-level efficiency that is close to the cell efficiency and minimize parasitic heating. In a scaled-up product consisting of many cell strings, two top strings could be connected in parallel with three bottom strings such that their outputs are voltage-matched.

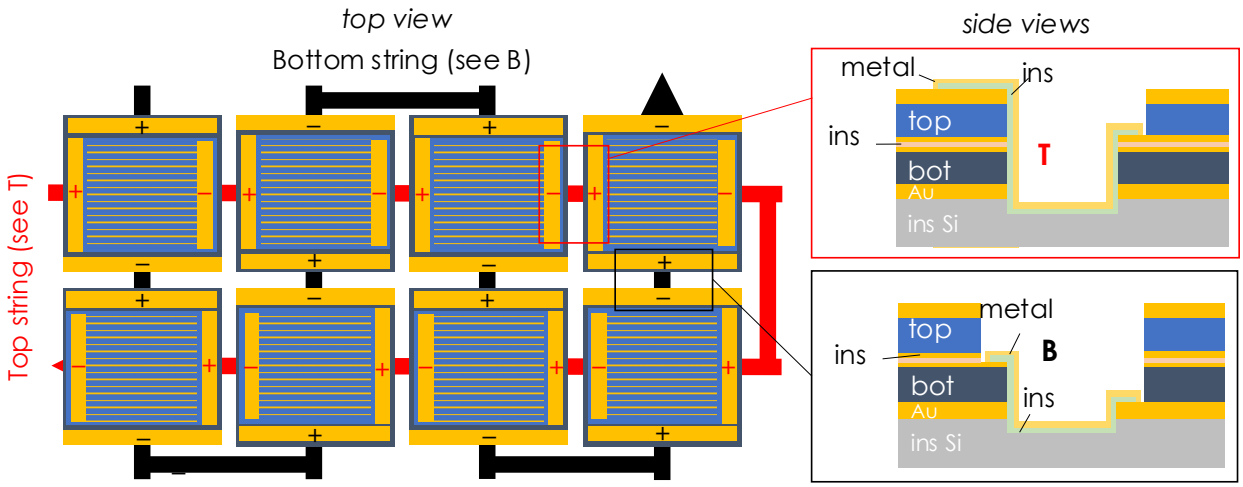

Figure 6.6 4T independent series interconnection of top and bottom cells. Top (T) and bottom (B) interconnects are lithographically defined and integrated on the insulating handle (Si).

6.4 Techno-economic analysis

Technoeconomic analysis (TEA) is important for assessing the feasibility and economic viability of thermophotovoltaic (TPV) cells. It is vital to assess the cost competitiveness of these cells in comparison to the most advanced technologies in its field of application. For example, the use of TPV in thermal energy storage applications would necessitate competition with grid level energy

storage like pumped hydro storage and lithium-ion batteries. In designing thermal grid storage systems that are economically viable, a key area of development is high-efficiency thermophotovoltaics, which enables solid state conversion of thermal energy to electricity. Novel iterations using III-V semiconductor materials have achieved much higher conversion efficiencies and power densities. This performance, however, generally mandates extremely high emitter temperatures, incurring significant heat storage, insulation, and heat transfer costs. Future work should develop a systematic method of evaluating the total cost of a grid storage system as a function of the chosen TPV technology. This model could be adapted to other applications of TPV including waste heat recovery and cogeneration of heat and power.

References

1. Amy, C., Seyf, H. R., Steiner, M. A., Friedman, D. J. & Henry, A. Thermal energy grid storage using multi-junction photovoltaics. *Energy Environ Sci* **12**, 334–343 (2019).
2. Datas, A., López-Ceballos, A., López, E., Ramos, A. & del Cañizo, C. Latent heat thermophotovoltaic batteries. *Joule* **6**, 418–443 (2022).
3. Datas, A., Ramos, A., Martí, A., del Cañizo, C. & Luque, A. Ultra High Temperature Latent Heat Energy Storage and Thermophotovoltaic Energy Conversion. *Energy* **107**, 542 (2016).
4. LaPotin, A. *et al.* Thermophotovoltaic efficiency of 40%. *Nature* **604**, 287–291 (2022).
5. Qiu, K. & Hayden, A. C. S. Performance of low bandgap thermophotovoltaic cells in a small cogeneration system. *Solar Energy* **74**, 489–495 (2003).
6. Fraas, L. M., Avery, J. E. & Huang, H. X. Thermophotovoltaic Furnace-Generator for the Home Using Low Bandgap GaSb Cells. *Semicond. Sci. Technol.* **18**, S247 (2003).
7. Licht, A., Pfiester, N., DeMeo, D., Chivers, J. & Vandervelde, T. E. A Review of Advances in Thermophotovoltaics for Power Generation and Waste Heat Harvesting. *MRS Adv* **4**, 2271–2282 (2019).
8. Utlu, Z. Thermophotovoltaic applications in waste heat recovery systems: example of GaSb cell. *International Journal of Low-Carbon Technologies* **15**, 277–286 (2020).
9. Bierman, D. M. *et al.* Enhanced photovoltaic energy conversion using thermally based spectral shaping. *Nat Energy* **1**, (2016).
10. Maghanki, M. M., Ghobadian, B., Najafi, G. & Galogah, R. J. Micro combined heat and power (MCHP) technologies and applications. *Renewable and Sustainable Energy Reviews* **28**, 510–524 (2013).
11. Fraas, L. M., Avery, J. E. & Huang, H. X. Thermophotovoltaic furnace-generator for the home using low bandgap GaSb cells. *Semicond Sci Technol* **18**, (2003).
12. Bianchi, M., Ferrari, C., Melino, F. & Peretto, A. Feasibility study of a Thermo-Photo-Voltaic system for CHP application in residential buildings. *Appl Energy* **97**, 704–713 (2012).
13. Seyf, H. R. & Henry, A. Thermophotovoltaics: A potential pathway to high efficiency concentrated solar power. *Energy Environ Sci* **9**, 2654–2665 (2016).
14. Smallbone, A., Jülch, V., Wardle, R. & Roskilly, A. P. Levelised Cost of Storage for Pumped Heat Energy Storage in comparison with other energy storage technologies. *Energy Convers Manag* **152**, 221–228 (2017).
15. Datas, A., Ramos, A., Martí, A., del Cañizo, C. & Luque, A. Ultra high temperature latent heat energy storage and thermophotovoltaic energy conversion. *Energy* **107**, 542–549 (2016).
16. Amy, C., Seyf, H. R., Steiner, M. A., Friedman, D. J. & Henry, A. Thermal energy grid storage using multi-junction photovoltaics. *Energy Environ Sci* **12**, 334–343 (2019).
17. Narayan, T. C. *et al.* Platform for Accurate Efficiency Quantification of > 35% Efficient Thermophotovoltaic Cells. in *2021 IEEE 48th Photovoltaic Specialists Conference (PVSC)* 1352–1354 (2021). doi:10.1109/PVSC43889.2021.9518588.

18. Narayan, T. C. *et al.* World record demonstration of > 30% thermophotovoltaic conversion efficiency. in *2020 47th IEEE Photovoltaic Specialists Conference (PVSC)* 1792–1795 (2020). doi:10.1109/PVSC45281.2020.9300768.
19. Fan, D. *et al.* Near-perfect photon utilization in an air-bridge thermophotovoltaic cell. *Nature* **586**, 237–241 (2020).
20. Omair, Z. *et al.* Ultraefficient thermophotovoltaic power conversion by band-edge spectral filtering. (2019) doi:10.1073/pnas.1903001116.
21. Siergiej, R. R. *et al.* 20\% Efficient InGaAs/InPAs Thermophotovoltaic Cells. *AIP Conf Proc* **653**, 414–423 (2003).
22. Wernsman, B. *et al.* Greater Than 20\% Radiant Heat Conversion Efficiency of a Thermophotovoltaic Radiator/Module System Using Reflective Spectral Control. *IEEE Trans. Electron Devices* **51**, 512 (2004).
23. Woolf, D. N. *et al.* High-efficiency thermophotovoltaic energy conversion enabled by a metamaterial selective emitter. *Optica* **5**, 213 (2018).
24. Arulanandam, M. K. *et al.* GaAs thermophotovoltaic patterned dielectric back contact devices with improved sub-bandgap reflectance. *Solar Energy Materials and Solar Cells* **238**, 111545 (2022).
25. Yu, Y. Z. *et al.* High-Efficiency Multi-Cell TPV Module Fabrication and Performance. *AIP Conf Proc* **653**, 335–343 (2003).
26. Dashiell, M. W. *et al.* Quaternary InGaAsSb Thermophotovoltaic Diodes. *IEEE Trans Electron Devices* **53**, 2879–2891 (2006).
27. Schulte, K. L. *et al.* Inverted metamorphic AlGaInAs/GaInAs tandem thermophotovoltaic cell designed for thermal energy grid storage application. *J Appl Phys* **128**, 143103 (2020).
28. Tervo, E. J. *et al.* Efficient and scalable GaInAs thermophotovoltaic devices. *Joule* **6**, 2566–2584 (2022).
29. Schlegl, T. TPV Modules Based On GaSb Structures. **285**, 285–293 (2004).
30. Bitnar, B., Durisch, W., Meyer, A. & Palfinger, G. New Flexible Photocell Module for Thermophotovoltaic Applications. *AIP Conf. Proc.* **653**, 465 (2002).
31. Ferguson, L. G. & Dogan, F. A highly efficient NiO-Doped MgO matched emitter for thermophotovoltaic energy conversion. *Materials Science and Engineering: B* **83**, 35–41 (2001).
32. Bitnar, S. *et al.* Practical thermophotovoltaic generators. *Semiconductors* **38**, 941–945 (2004).
33. Rinnerbauer, V. *et al.* High-temperature stability and selective thermal emission of polycrystalline tantalum photonic crystals. *Opt Express* **21**, 11482–11491 (2013).
34. Yeng, Y. X. *et al.* Enabling high-temperature nanophotonics for energy applications. *Proc Natl Acad Sci U S A* **109**, 2280–2285 (2012).
35. Nakagawa, N., Ohtsubo, H., Waku, Y. & Yugami, H. Thermal emission properties of Al2O3/Er3Al5O12 eutectic ceramics. *J Eur Ceram Soc* **25**, 1285–1291 (2005).
36. Arpin, K. A., Losego, M. D. & Braun, P. V. Electrodeposited 3D Tungsten Photonic Crystals with Enhanced Thermal Stability. *Chemistry of Materials* **23**, 4783–4788 (2011).
37. Hassan, S., Doiron, C. F. & Naik, G. V. Optimum selective emitters for efficient thermophotovoltaic conversion. *Appl Phys Lett* **116**, 023903 (2020).
38. Huang, T. C., Wang, B. X. & Zhao, C. Y. A novel selective thermophotovoltaic emitter based on multipole resonances. *Int J Heat Mass Transf* **182**, 122039 (2022).

39. Wang, Z. *et al.* Selective emitter materials and designs for high-temperature thermophotovoltaic applications. *Solar Energy Materials and Solar Cells* **238**, 111554 (2022).
40. Fernández, J., Dimroth, F., Oliva, E., Hermle, M. & Bett, A. W. Back-surface optimization of Germanium TPV cells. *AIP Conf Proc* **890**, 190–197 (2007).
41. Burger, T., Fan, D., Lee, K., Forrest, S. & Lenert, A. Thin-Film Thermophotovoltaic Cells with High Spectral Selectivity. (2018).
42. Wang, C. A. *et al.* Wafer Bonding and Epitaxial Transfer of GaSb-Based Epitaxy to GaAs for Monolithic Interconnection of Thermophotovoltaic Devices. *J Electron Mater* **33**, 213–217 (2004).
43. Wu, X. *et al.* A study of contacts and back-surface reflectors for 0.6-eV Ga0.32In0.68As/InAs0.32P0.68 thermophotovoltaic monolithically interconnected modules. *AIP Conf Proc* **460**, 517–524 (1999).
44. Burger, T., Fan, D., Lee, K., Forrest, S. R. & Lenert, A. Thin-Film Architectures with High Spectral Selectivity for Thermophotovoltaic Cells. *ACS Photonics* **5**, 2748–2754 (2018).
45. Arulanandam, M. K. *et al.* GaAs thermophotovoltaic patterned dielectric back contact devices with improved sub-bandgap reflectance. *Solar Energy Materials and Solar Cells* **238**, 111545 (2022).
46. Swanson, R. M. Recent developments in thermophotovoltaic conversion. *1980 International Electron Devices Meeting* 186–189 (1980) doi:10.1109/IEDM.1980.189789.
47. Wernsman, B. *et al.* Greater than 20% radiant heat conversion efficiency of a thermophotovoltaic radiator/module system using reflective spectral control. *IEEE Trans Electron Devices* **51**, 512–515 (2004).
48. Omair, Z. *et al.* Ultraefficient thermophotovoltaic power conversion by band-edge spectral filtering. *Proceedings of the National Academy of Sciences* **116**, 15356–15361 (2019).
49. Burger, T., Fan, D., Lee, K., Forrest, S. R. & Lenert, A. Thin-Film Architectures with High Spectral Selectivity for Thermophotovoltaic Cells. *ACS Photonics* **5**, (2018).
50. Burger, T., Fan, D., Lee, K., Forrest, S. R. & Lenert, A. Thin Films for Enhanced Photon Recycle in Thermophotovoltaics. in *2018 IEEE 7th World Conference on Photovoltaic Energy Conversion, WCPEC 2018 - A Joint Conference of 45th IEEE PVSC, 28th PVSEC and 34th EU PVSEC* (2018). doi:10.1109/PVSC.2018.8547905.
51. Ferguson, L. G. & Dogan, F. A highly efficient NiO-doped MgO matched emitter for thermophotovoltaic energy conversion. *Mater Sci Eng B Solid State Mater Adv Technol* **83**, 35–41 (2001).
52. Rinnerbauer, V. *et al.* High-temperature stability and selective thermal emission of polycrystalline tantalum photonic crystals. *Opt Express* **21**, 11482 (2013).
53. Woolf, D. N. *et al.* High-efficiency thermophotovoltaic energy conversion enabled by a metamaterial selective emitter. *Optica* **5**, 213 (2018).
54. Fourspring, P. M., DePoy, D. M., Jr., T. D. R., Lazo-Wasem, J. E. & Gratrix, E. J. Optical coatings for thermophotovoltaic spectral control. *Appl. Opt.* **45**, 1356–1358 (2006).
55. Sakakibara, R. *et al.* Practical emitters for thermophotovoltaics: a review. *J Photonics Energy* **9**, 1–20 (2019).
56. Lenert, A. *et al.* A nanophotonic solar thermophotovoltaic device. *Nat Nanotechnol* **9**, (2014).
57. Fan, D. *et al.* Near-perfect photon utilization in an air-bridge thermophotovoltaic cell. *Nature* **586**, 237–241 (2020).

58. Burger, T., Sempere, C., Roy-Layinde, B. & Lenert, A. Present Efficiencies and Future Opportunities in Thermophotovoltaics. *Joule* **4**, 1660–1680 (2020).
59. Burger, T., Sempere, C. & Lenert, A. Thermophotovoltaic energy conversion: materials and device engineering. in *Nanoscale Energy Transport* 17–1 to 17–26 (IOP Publishing, 2020). doi:10.1088/978-0-7503-1738-2ch17.
60. Ferrari, C., Melino, F., Pinelli, M., Spina, P. R. & Venturini, M. Overview and status of thermophotovoltaic systems. *Energy Procedia* **45**, 160–169 (2014).
61. Lenert, A. *et al.* A nanophotonic solar thermophotovoltaic device. *Nat Nanotechnol* **9**, (2014).
62. Datas, A. & Martí, A. Thermophotovoltaic energy in space applications: Review and future potential. *Solar Energy Materials and Solar Cells* **161**, 285–296 (2017).
63. Burger, T., Sempere, C., Roy-Layinde, B. & Lenert, A. Present Efficiencies and Future Opportunities in Thermophotovoltaics. *Joule* **4**, 1660–1680 (2020).
64. Burger, T., Sempere, C., Roy-Layinde, B. & Lenert, A. Present Efficiencies and Future Opportunities in Thermophotovoltaics. *Joule* **4**, 1660 (2020).
65. Fan, D. *et al.* Near-perfect photon utilization in an air-bridge thermophotovoltaic cell. *Nature* (2020) doi:10.1038/s41586-020-2717-7.
66. Mahorter, R. G., Wernsman, B., Thomas, R. M. & Siergiej, R. R. Thermophotovoltaic system testing. *Semicond Sci Technol* **18**, (2003).
67. Wernsman, B. *et al.* Greater than 20% radiant heat conversion efficiency of a thermophotovoltaic radiator/module system using reflective spectral control. *IEEE Trans Electron Devices* **51**, 512–515 (2004).
68. López, E., Artacho, I. & Datas, A. Thermophotovoltaic conversion efficiency measurement at high view factors. *Solar Energy Materials and Solar Cells* **250**, 112069 (2023).
69. Swanson, R. M. Recent developments in thermophotovoltaic conversion. *1980 International Electron Devices Meeting* 186–189 (1980) doi:10.1109/IEDM.1980.189789.
70. Narayan, T. C. *et al.* Platform for Accurate Efficiency Quantification of >35% Efficient Thermophotovoltaic Cells. in *2021 IEEE 48th Photovoltaic Specialists Conference (PVSC)* 1352–1354 (IEEE, 2021). doi:10.1109/PVSC43889.2021.9518588.
71. Bierman, D. M. *et al.* Enhanced photovoltaic energy conversion using thermally based spectral shaping. *Nat Energy* **1**, (2016).
72. Cabrera, A. *et al.* Thermophotovoltaic efficiency measurement : design and analysis of a novel experimental method. 1–4 (2018).
73. Forrest, S. R. Performance of InxGa1-xAsyP1-y Photodiodes with Dark Current Limited by Diffusion, Generation Recombination, and Tunneling. *IEEE J Quantum Electron* **17**, 217–226 (1981).
74. Zhao, Y. *et al.* InGaAs--InP avalanche photodiodes with dark current limited by generation-recombination. *Opt. Express* **19**, 8546–8556 (2011).
75. Maeda, T. *et al.* Shockley-Read-Hall lifetime in homoepitaxial p-GaN extracted from recombination current in GaN p-n+ junction diodes. *Jpn J Appl Phys* **58**, (2019).
76. Cuevas, A. The Recombination Parameter J0. *Energy Procedia* **55**, 53–62 (2014).
77. Goetz, K. H. *et al.* Optical and crystallographic properties and impurity incorporation of Ga (x) In (1-x) As(with x between 0. 44 and 0. 49) grown by liquid phase epitaxy, vapor phase epitaxy, and metal organic chemical vapor deposition. *J Appl Phys* **54**, 4543–4552 (1983).
78. Ahrenkiel, R. K., Ellingson, R., Johnston, S. & Wanlass, M. Recombination lifetime of In0.53Ga0.47As as a function of doping density. *Appl Phys Lett* **72**, 3470–3472 (1998).

79. Chen, K., Zhao, B. & Fan, S. MESH: A free electromagnetic solver for far-field and near-field radiative heat transfer for layered periodic structures. *Comput Phys Commun* **231**, 163–172 (2018).
80. Quero, J. M., Perdigones, F. & Aracil, C. 11 - Microfabrication technologies used for creating smart devices for industrial applications. in *Smart Sensors and MEMs (Second Edition)* (eds. Nihtianov, S. & Luque, A.) 291–311 (Woodhead Publishing, 2018). doi:https://doi.org/10.1016/B978-0-08-102055-5.00011-5.
81. Yilbas, B. S., Al-Sharafi, A. & Ali, H. Chapter 3 - Surfaces for Self-Cleaning. in *Self-Cleaning of Surfaces and Water Droplet Mobility* (eds. Yilbas, B. S., Al-Sharafi, A. & Ali, H.) 45–98 (Elsevier, 2019). doi:https://doi.org/10.1016/B978-0-12-814776-4.00003-3.
82. Tsau, C. H., Spearing, S. M. & Schmidt, M. A. Fabrication of wafer-level thermocompression bonds. *Journal of Microelectromechanical Systems* **11**, 641–647 (2002).
83. Reinert, W., Kulkarni, A., Vuorinen, V. & Merz, P. Chapter 32 - Metallic Alloy Seal Bonding. in *Handbook of Silicon Based MEMS Materials and Technologies (Second Edition)* (eds. Tilli, M. et al.) 626–639 (William Andrew Publishing, Boston, 2015). doi:https://doi.org/10.1016/B978-0-323-29965-7.00032-4.
84. Amy, C. *et al.* Pumping liquid metal at high temperatures up to 1,673 kelvin. *Nature* **550**, 199–203 (2017).
85. Datas, A., Chubb, D. L. & Veeraragavan, A. Steady state analysis of a storage integrated solar thermophotovoltaic (SISTPV) system. *Solar Energy* **96**, 33–45 (2013).
86. Seyf, H. R. & Henry, A. Thermophotovoltaics: A potential pathway to high efficiency concentrated solar power. *Energy Environ Sci* **9**, 2654–2665 (2016).
87. Durisch, W. & Bitnar, B. Novel thin film thermophotovoltaic system. *Solar Energy Materials and Solar Cells* **94**, 960–965 (2010).
88. Fraas, L. M., Avery, J. E. & Huang, H. X. Thermophotovoltaic furnace-generator for the home using low bandgap GaSb cells. *Semicond Sci Technol* **18**, (2003).
89. Ahrenkiel, R. K., Ellingson, R., Johnston, S. & Wanlass, M. Recombination lifetime of In0.53Ga0.47As as a function of doping density. *Appl Phys Lett* **72**, 3470–3472 (1998).
90. Talghader, J. & Smith, J. S. Thermal dependence of the refractive index of GaAs and AlAs measured using semiconductor multilayer optical cavities. *Appl Phys Lett* **335**, 335 (1995).
91. Bertolotti, M. *et al.* Temperature dependence of the refractive index in semiconductors. *J. Opt. Soc. Am. B* **7**, 918–922 (1990).
92. Shockley, W. & Queisser, H. J. Detailed balance limit of efficiency of p-n junction solar cells. *J Appl Phys* **32**, 510–519 (1961).
93. Burger, T., Sempere, C. & Lenert, A. Thermophotovoltaic energy conversion: materials and device engineering. in *Nanoscale Energy Transport* 17–26 (IOP Publishing, 2020). doi:10.1088/978-0-7503-1738-2ch17.
94. Dupré, O. *et al.* A Thermal Model for the Design of Photovoltaic Devices. in *Thermal Behavior of Photovoltaic Devices* 75–103 (Springer International Publishing, 2017). doi:10.1007/978-3-319-49457-9_3.
95. Kersten, F. *et al.* Degradation of multicrystalline silicon solar cells and modules after illumination at elevated temperature. *Solar Energy Materials and Solar Cells* **142**, 83–86 (2015).

96. Kaaya, I., Ascencio-Vásquez, J., Weiss, K.-A. & Topič, M. Assessment of uncertainties and variations in PV modules degradation rates and lifetime predictions using physical models. *Solar Energy* **218**, 354–367 (2021).
97. Dupré, O., Vaillon, R. & Green, M. A. Physics of the temperature coefficients of solar cells. *Solar Energy Materials and Solar Cells* **140**, 92–100 (2015).
98. Makrides, G., Zinsser, B., Georghiou, G. E., Schubert, M. & Werner, J. H. Temperature behaviour of different photovoltaic systems installed in Cyprus and Germany. *Solar Energy Materials and Solar Cells* **93**, 1095–1099 (2009).
99. Singh, P. & Ravindra, N. M. Temperature dependence of solar cell performance - An analysis. *Solar Energy Materials and Solar Cells* **101**, 36–45 (2012).
100. Martín, D. & Algora, C. Temperature-dependent GaSb material parameters for reliable thermophotovoltaic cell modelling. *Semicond Sci Technol* **19**, 1040–1052 (2004).
101. Wang, Z., Zhang, H., Zhao, W., Zhou, Z. & Chen, M. The Effect of Concentrated Light Intensity on Temperature Coefficient of the InGaP / InGaAs / Ge Triple-Junction Solar Cell. 106–111 (2015).
102. Tonui, J. K. & Tripanagnostopoulos, Y. Air-cooled PV / T solar collectors with low cost performance improvements. **81**, 498–511 (2007).
103. Huang, M. J., Eames, P. C. & Norton, B. Chapter 454 - The Application of Computational Fluid Dynamics to Predict the Performance of Phase Change Materials for Control of Photovoltaic Cell Temperature in Buildings. in *World Renewable Energy Congress VI* (ed. Sayigh, A. A. M.) 2123–2126 (Pergamon, Oxford, 2000). doi:https://doi.org/10.1016/B978-008043865-8/50454-2.
104. Emam, M. & Ahmed, M. Cooling concentrator photovoltaic systems using various configurations of phase-change material heat sinks. *Energy Convers Manag* **158**, 298–314 (2018).
105. Khanna, S., Reddy, K. S. & Mallick, T. K. Optimization of finned solar photovoltaic phase change material (finned pv pcm) system. *International Journal of Thermal Sciences* **130**, 313–322 (2018).
106. Khanjari, Y., Pourfayaz, F. & Kasaeian, A. B. Numerical investigation on using of nanofluid in a water-cooled photovoltaic thermal system. *Energy Convers Manag* **122**, 263–278 (2016).
107. Al-Waeli, A. H. A. *et al.* Modeling and experimental validation of a PVT system using nanofluid coolant and nano-PCM. *Solar Energy* **177**, 178–191 (2019).
108. Reddy, K. S., Lokeswaran, S., Agarwal, P. & Mallick, T. K. Numerical Investigation of Micro-channel based Active Module Cooling for Solar CPV System. *Energy Procedia* **54**, 400–416 (2014).
109. Yang, K. & Zuo, C. A novel multi-layer manifold microchannel cooling system for concentrating photovoltaic cells. *Energy Convers Manag* **89**, 214–221 (2015).
110. Sakakibara, R. *et al.* Practical emitters for thermophotovoltaics: A review. *J Photonics Energy* **9**, (2019).
111. Vaidhyanathan Krishnamurthy, G. *et al.* Iridium-Based Selective Emitters for Thermophotovoltaic Applications. *Advanced Materials* **n/a**, 2305922.
112. Dias, M. R. S. *et al.* Photonics roadmap for ultra-high-temperature thermophotovoltaics. *Joule* (2023) doi:https://doi.org/10.1016/j.joule.2023.08.015.
113. McSherry, S. *et al.* Nanophotonic control of thermal emission under extreme temperatures in air. *Nat Nanotechnol* **17**, 1104–1110 (2022).

114. Gong, T., Duncan, M. A., Karahadian, M., Leite, M. S. & Munday, J. N. Broadband Superabsorber Operating at 1500 °C Using Dielectric Bilayers. *ACS Applied Optical Materials* **1**, 1615–1619 (2023).
115. Burger, T. *et al.* Semitransparent thermophotovoltaics for efficient utilization of moderate temperature thermal radiation. *Proceedings of the National Academy of Sciences* **119**, e2215977119 (2022).
116. Omair, Z. *et al.* Ultraefficient Thermophotovoltaic Power Conversion by Band-Edge Spectral Filtering. *Proc. Natl. Acad. Sci. U. S. A.* **116**, 15356 (2019).
117. Lee, B. *et al.* Air-Bridge Si Thermophotovoltaic Cell with High Photon Utilization. *ACS Energy Lett* **7**, 2388–2392 (2022).
118. Tervo, E. J. *et al.* Efficient and Scalable GaInAs Thermophotovoltaic Devices. (2022) doi:https://doi.org/10.48550/arXiv.2207.00565.
119. Lim, J., Roy-Layinde, B., Liu, B., Lenert, A. & Forrest, S. R. Enhanced Photon Utilization in Single Cavity Mode Air-Bridge Thermophotovoltaic Cells. *ACS Energy Lett* **8**, 2935–2939 (2023).
120. Horowitz, K. A., Remo, T. W., Smith, B. & Ptak, A. J. *A Techno-Economic Analysis and Cost Reduction Roadmap for III-V Solar Cells*. https://www.osti.gov/biblio/1484349 (2018) doi:10.2172/1484349.
121. Ward, J. S. *et al.* Techno-economic analysis of three different substrate removal and reuse strategies for III-V solar cells. *Progress in Photovoltaics: Research and Applications* **24**, 1284–1292 (2016).
122. Lim, J. & Forrest, S. R. Limits to the Energy-Conversion Efficiency of Air-Bridge Thermophotovoltaics. *Phys Rev Appl* **19**, 34099 (2023).
123. Jurczak, P., Onno, A., Sablon, K. & Liu, H. Efficiency of GaInAs thermophotovoltaic cells: the effects of incident radiation, light trapping and recombinations. *Opt Express* **23**, A1208 (2015).
124. Deng, X.-H., Liu, J.-T., Yuan, J.-R., Liao, Q.-H. & Liu, N.-H. A new transfer matrix method to calculate the optical absorption of graphene at any position in stratified media. *Europhys Lett* **109**, 27002 (2015).
125. Roy-Layinde, B. *et al.* Sustaining efficiency at elevated power densities in InGaAs airbridge thermophotovoltaic cells. *Solar Energy Materials and Solar Cells* **236**, 111523 (2022).
126. Swanson, R. M. Recent Developments in Thermophotovoltaic Conversion. in *Photovoltaic Solar Energy Conference* (ed. Palz, W.) 1097 (Springer Netherlands, Dordrecht, 1981).
127. Narayan, T. C. *et al.* World record demonstration of >30% thermophotovoltaic conversion efficiency. in *2020 47th IEEE Photovoltaic Specialists Conference (PVSC)* 1792–1795 (2020). doi:10.1109/PVSC45281.2020.9300768.
128. Fan, D. *et al.* Near-perfect photon utilization in an air-bridge thermophotovoltaic cell. *Nature* (2020) doi:10.1038/s41586-020-2717-7.
129. Narayan, T. C. *et al.* Platform for Accurate Efficiency Quantification of >35% Efficient Thermophotovoltaic Cells. in *2021 IEEE 48th Photovoltaic Specialists Conference (PVSC)* 1352–1354 (IEEE, 2021). doi:10.1109/PVSC43889.2021.9518588.
130. Arulanandam, M. K. *et al.* GaAs thermophotovoltaic patterned dielectric back contact devices with improved sub-bandgap reflectance. *Solar Energy Materials and Solar Cells* **238**, 111545 (2022).
131. Tervo, E. J. *et al.* Efficient and Scalable GaInAs Thermophotovoltaic Devices. (2022) doi:https://doi.org/10.48550/arXiv.2207.00565.

132. LaPotin, A. *et al.* Thermophotovoltaic efficiency of 40%. *Nature* **604**, 287–291 (2022).
133. Tervo, E. J. *et al.* Efficient and Scalable GaInAs Thermophotovoltaic Devices. (2022) doi:https://doi.org/10.48550/arXiv.2207.00565.
134. Licht, A., Pfiester, N., DeMeo, D., Chivers, J. & Vandervelde, T. E. A Review of Advances in Thermophotovoltaics for Power Generation and Waste Heat Harvesting. *MRS Adv* **4**, 2271–2282 (2019).
135. Tang, L., Fraas, L. M., Liu, Z., Xu, C. & Chen, X. Performance Improvement of the GaSb Thermophotovoltaic Cells with n-Type Emitters. *IEEE Trans Electron Devices* **62**, 2809–2815 (2015).
136. McMillan, C. *Manufacturing Thermal Energy Use in 2014*. (2019) doi:https://doi.org/10.7799/1570008.
137. Lenert, A. *et al.* A nanophotonic solar thermophotovoltaic device. *Nat Nanotechnol* **9**, 126–130 (2014).
138. Harder, N.-P. & W rfel, P. Theoretical limits of thermophotovoltaic solar energy conversion. *Semicond Sci Technol* **18**, S151–S157 (2003).
139. Ungaro, C., Gray, S. K. & Gupta, M. C. Solar thermophotovoltaic system using nanostructures. *Opt Express* **23**, A1149–A1156 (2015).
140. Rephaeli, E. & Fan, S. Absorber and emitter for solar thermo-photovoltaic systems to achieve efficiency exceeding the Shockley-Queisser limit. *Opt Express* **17**, 15145 (2009).
141. Zhou, Z., Sakr, E., Sun, Y. & Bermel, P. Solar thermophotovoltaics: reshaping the solar spectrum. *Nanophotonics* **5**, 1–21 (2016).
142. Wang, Y., Liu, H. & Zhu, J. Solar thermophotovoltaics: Progress, challenges, and opportunities. *APL Mater* **7**, 080906 (2019).
143. Bierman, D. M. *et al.* Enhanced photovoltaic energy conversion using thermally based spectral shaping. *Nat Energy* **1**, 16068 (2016).
144. Bhatt, R., Kravchenko, I. & Gupta, M. High-efficiency solar thermophotovoltaic system using a nanostructure-based selective emitter. *Solar Energy* **197**, 538–545 (2020).
145. Wilt, D., Chubb, D., Wolford, D., Magari, P. & Crowley, C. Thermophotovoltaics for Space Power Applications. *AIP Conf Proc* **890**, 335–345 (2007).
146. Gupta, M. C., Ungaro, C., Foley, J. J. & Gray, S. K. Optical nanostructures design, fabrication, and applications for solar/thermal energy conversion. *Solar Energy* **165**, 100–114 (2018).
147. Shimizu, M., Kohiyama, A. & Yugami, H. Evaluation of thermal stability in spectrally selective few-layer metallo-dielectric structures for solar thermophotovoltaics. *J Quant Spectrosc Radiat Transf* **212**, 45–49 (2018).
148. Bitnar, S. *et al.* Practical thermophotovoltaic generators. *Semiconductors* **38**, 941–945 (2004).
149. McSherry, S. *et al.* Nanophotonic control of thermal emission under extreme temperatures in air. *Nat Nanotechnol* (2022) doi:10.1038/s41565-022-01205-1.
150. Chirumamilla, M. *et al.* Thermal stability of tungsten based metamaterial emitter under medium vacuum and inert gas conditions. *Sci Rep* **10**, 3605 (2020).
151. Swanson, R. M. Recent developments in thermophotovoltaic conversion. *1980 International Electron Devices Meeting* 186–189 (1980) doi:10.1109/IEDM.1980.189789.
152. Burger, T., Fan, D., Lee, K., Forrest, S. & Lenert, A. Thin-Film Thermophotovoltaic Cells with High Spectral Selectivity. (2018).

153. Narayan, T. C. *et al.* World record demonstration of >30% thermophotovoltaic conversion efficiency. in *2020 47th IEEE Photovoltaic Specialists Conference (PVSC)* 1792–1795 (2020). doi:10.1109/PVSC45281.2020.9300768.
154. Narayan, T. C. *et al.* Platform for Accurate Efficiency Quantification of >35% Efficient Thermophotovoltaic Cells. in *2021 IEEE 48th Photovoltaic Specialists Conference (PVSC)* 1352–1354 (IEEE, 2021). doi:10.1109/PVSC43889.2021.9518588.
155. Lee, K., Zimmerman, J. D., Hughes, T. W. & Forrest, S. R. Non-Destructive Wafer Recycling for Low-Cost Thin-Film Flexible Optoelectronics. 4284–4291 (2014) doi:10.1002/adfm.201400453.
156. Burger, T., Fan, D., Lee, K., Forrest, S. & Lenert, A. Thin-Film Thermophotovoltaic Cells with High Spectral Selectivity. (2018).
157. Deng, X.-H., Liu, J.-T., Yuan, J.-R., Liao, Q.-H. & Liu, N.-H. A new transfer matrix method to calculate the optical absorption of graphene at any position in stratified media. *Europhys Lett* **109**, 27002 (2015).
158. Roy-Layinde, B. *et al.* Sustaining efficiency at elevated power densities in InGaAs airbridge thermophotovoltaic cells. *Solar Energy Materials and Solar Cells* **236**, 111523 (2022).
159. Wernsman, B. *et al.* Greater than 20% radiant heat conversion efficiency of a thermophotovoltaic radiator/module system using reflective spectral control. *IEEE Trans Electron Devices* **51**, 512–515 (2004).
160. Woolf, D. N. *et al.* High-efficiency thermophotovoltaic energy conversion enabled by a metamaterial selective emitter. *Optica* **5**, 213–218 (2018).
161. Dashiell, M. W. *et al.* Quaternary InGaAsSb Thermophotovoltaic Diodes. *IEEE Trans Electron Devices* **53**, 2879–2891 (2006).
162. Ahrenkiel, R. K., Ellingson, R., Johnston, S. & Wanlass, M. Recombination lifetime of In 0 . 53 Ga 0 . 47 As as a function of doping density. **72**, 3470–3472 (1998).
163. Yue, S. *et al.* High ambipolar mobility in cubic boron arsenide revealed by transient reflectivity microscopy. *Science (1979)* **377**, 433–436 (2022).
164. Schulte, K. L. *et al.* Inverted metamorphic AlGaInAs/GaInAs tandem thermophotovoltaic cell designed for thermal energy grid storage application. *J Appl Phys* **128**, 143103 (2020).
165. Feldmann, F. *et al.* Carrier-selective contacts for Si solar cells. *Appl Phys Lett* **104**, 181105 (2014).
166. D'Rozario, J. R., Polly, S. J., Nelson, G. T., Wilt, D. & Hubbard, S. M. Modeling free-carrier absorption in ultrathin III-V solar cells with light management. *Opt Express* **30**, 7096–7109 (2022).
167. Shoji, Y., Oshima, R., Makita, K., Ubukata, A. & Sugaya, T. Pd-mediated mechanical stack of III–V solar cells fabricated via hydride vapor phase epitaxy. *Solar Energy* **224**, 142–148 (2021).
168. Kao, Y.-C. *et al.* Performance comparison of III–V//Si and III–V//InGaAs multi-junction solar cells fabricated by the combination of mechanical stacking and wire bonding. *Sci Rep* **9**, 4308 (2019).
169. Han, S. *et al.* Integration of Subcells in III-V//Si Tandem Solar Cells. *Transactions on Electrical and Electronic Materials* **24**, 132–139 (2023).
170. Makita, K. *et al.* III-V//CuxIn1−yGaySe2 multijunction solar cells with 27.2% efficiency fabricated using modified smart stack technology with Pd nanoparticle array and adhesive material. *Progress in Photovoltaics: Research and Applications* **29**, 887–898 (2021).

171. Makita, K. *et al.* Mechanical stacked GaAs//CuIn1−yGaySe2 three-junction solar cells with 30% efficiency via an improved bonding interface and area current-matching technique. *Progress in Photovoltaics: Research and Applications* **31**, 71–84 (2023).
172. Zhao, L., Flamand, G. & Poortmans, J. Recent Progress and Spectral Robustness Study for Mechanically Stacked Multi-junction Solar Cells. *AIP Conf Proc* **1277**, 284–289 (2010).
173. Dawidowski, W. *et al.* Tunnel junction limited performance of InGaAsN/GaAs tandem solar cell. *Solar Energy* **214**, 632–641 (2021).
174. Hagar, B. G., Sayed, I., Colter, P. C., El-Masry, N. A. & Bedair, S. M. A new approach for Multi junction solar cells from off the shelf individual cells: GaAs/Si. in *2019 IEEE 46th Photovoltaic Specialists Conference (PVSC)* 994–997 (2019). doi:10.1109/PVSC40753.2019.8980696.
175. Johnson, E. J. & Fan, H. Y. Impurity and Exciton Effects on the Infrared Absorption Edges of III-V Compounds. *Physical Review* **139**, A1991–A2001 (1965).
176. Wehrer, R. *et al.* InGaAs series-connected, tandem, MIM TPV converters. in *3rd World Conference onPhotovoltaic Energy Conversion, 2003. Proceedings of* vol. 1 892-895 Vol.1 (2003).
177. Schnabel, M. *et al.* Equivalent Performance in Three-Terminal and Four-Terminal Tandem Solar Cells. *IEEE J Photovolt* **8**, 1584–1589 (2018).
178. Warren, E. L. *et al.* Maximizing tandem solar cell power extraction using a three-terminal design. *Sustainable Energy Fuels* **2**, 1141–1147 (2018).
179. Warren, E. L. *et al.* A Taxonomy for Three-Terminal Tandem Solar Cells. *ACS Energy Lett* **5**, 1233–1242 (2020).
180. Lin, J. C., Yu, S. Y. & Mohney, S. E. Characterization of low-resistance ohmic contacts to n- and p-type InGaAs. *J Appl Phys* **114**, 044504 (2013).
181. Kelsall, C. C., Buznitsky, K. & Henry, A. *Technoeconomic Analysis of Thermal Energy Grid Storage Using Graphite and Tin*.
182. Lee, B., Fan, D. & Forrest, S. R. A high throughput, linear molecular beam epitaxy system for reduced cost manufacturing of GaAs photovoltaic cells: will GaAs ever be inexpensive enough? *Sustain Energy Fuels* **4**, 2035–2042 (2020).
183. Lee, K., Zimmerman, J. D., Hughes, T. W. & Forrest, S. R. Non-Destructive Wafer Recycling for Low-Cost Thin-Film Flexible Optoelectronics. *Adv Funct Mater* **24**, 4284–4291 (2014).
184. Lee, K., Shiu, K. T., Zimmerman, J. D., Renshaw, C. K. & Forrest, S. R. Multiple growths of epitaxial lift-off solar cells from a single InP substrate. *Appl Phys Lett* **97**, 10–12 (2010).

APPENDIX A: Complete Electrical Measurements for Quaternary TPV

Table A.1 Variation in measured open-circuit voltage (V_{OC}), short-circuit current (J_{SC}), fill factor (FF), and power density (P_{mpp}) versus emitter temperature (T_h) for the (a) 0.74 eV, (b) 0.9 eV, and (c) 1.1 eV air-bridge cells.

(a) 0.74 eV

T_h (°C)	J_{SC} (mA/cm^2)	V_{OC} (mV)	FF (%)	P_{mpp} (mW/cm^2)
745	51.30	449.53	72.96	16.83
830	107.73	472.74	74.85	38.12
909	196.49	490.06	74.59	71.82
985	327.80	504.02	73.58	121.56
1024	416.99	510.26	72.82	154.94
1060	514.95	516.21	72.22	191.97
1091	610.84	520.2	72.47	230.27
1132	759.76	525.52	70.07	279.76
1163	887.62	529.57	70.31	330.48
1203	1079.33	537.52	68.24	395.92
1235	1250.00	544.23	68.35	464.97
1277	1501.83	549.73	66.71	550.78
1313	1743.41	552.99	66.51	641.2
1350	2023.82	557.41	66.8	747.66
1271	1460.51	547.55	68.06	544.27
1308	1711.39	550.93	67.59	637.22
1351	2030.00	555.62	66.92	754.82
1395	2399.14	558.55	66.80	895.19
1478	3230.20	562.85	65.80	1196.30

(b) 0.9 eV

T_h (°C)	J_{SC} (mA/cm^2)	V_{OC} (mV)	FF (%)	P_{mpp} (mW/cm^2)
856	47.99	595.66	81.67	23.34
940	82.55	611.02	83.56	42.15
1001	139.20	623.05	82.52	71.57
1072	217.91	635.06	82.12	113.65
1135	294.42	639.35	82.38	155.08

1153	335.99	645.56	80.73	175.10
1221	472.20	650.00	80.73	247.79
1241	494.79	654.93	80.69	261.49
1252	563.17	657.43	78.06	289.02
1303	708.55	659.63	79.65	372.26
1334	774.00	664.61	79.12	407.00
1344	856.32	663.61	79.01	448.96
1388	1037.03	667.83	77.69	538.01
1397	1076.50	667.55	77.44	556.47
1429	1229.81	670.27	77.37	637.7
1433	1248.00	671.36	78.44	657.24
1476	1476.74	673.98	75.76	754.01
1487	1543.80	674.54	75.00	780.73
1518	1729.90	676.30	73.62	861.28
1532	1818.90	677.59	73.81	909.72

(c) 1.1 eV

T_h (°C)	J_{SC} (mA/cm^2)	V_{OC} (mV)	*FF* (%)	P_{mpp} (mW/cm^2)
869	4.67	688.44	82.98	2.67
906	6.75	707.19	82.10	3.92
947	9.45	713.20	82.57	5.67
974	12.47	726.75	83.41	7.56
1012	17.07	732.25	83.88	10.48
1039	21.15	740.19	83.28	13.04
1083	29.40	749.85	84.20	18.56
1102	33.79	752.56	83.69	21.28
1159	49.56	764.45	83.64	31.69
1166	51.90	766.95	83.35	33.17
1235	78.98	775.65	82.98	50.83
1236	79.79	778.15	83.68	51.96
1282	103.47	784.88	81.16	65.913
1309	120.01	787.33	81.93	77.41
1316	124.50	791.51	83.57	82.35
1352	149.34	794.82	81.03	96.18
1357	154.81	797.83	82.50	101.90
1399	188.15	801.13	80.15	120.81
1409	198.07	804.22	79.87	127.22
1472	263.32	809.85	81.85	174.54

1519	322.43	817.40	76.73	202.23
1575	403.99	822.18	75.03	249.21
1631	499.00	828.78	73.43	303.67
1687	610.43	831.93	70.53	358.16

APPENDIX B: Electrical Performance of Homotandem

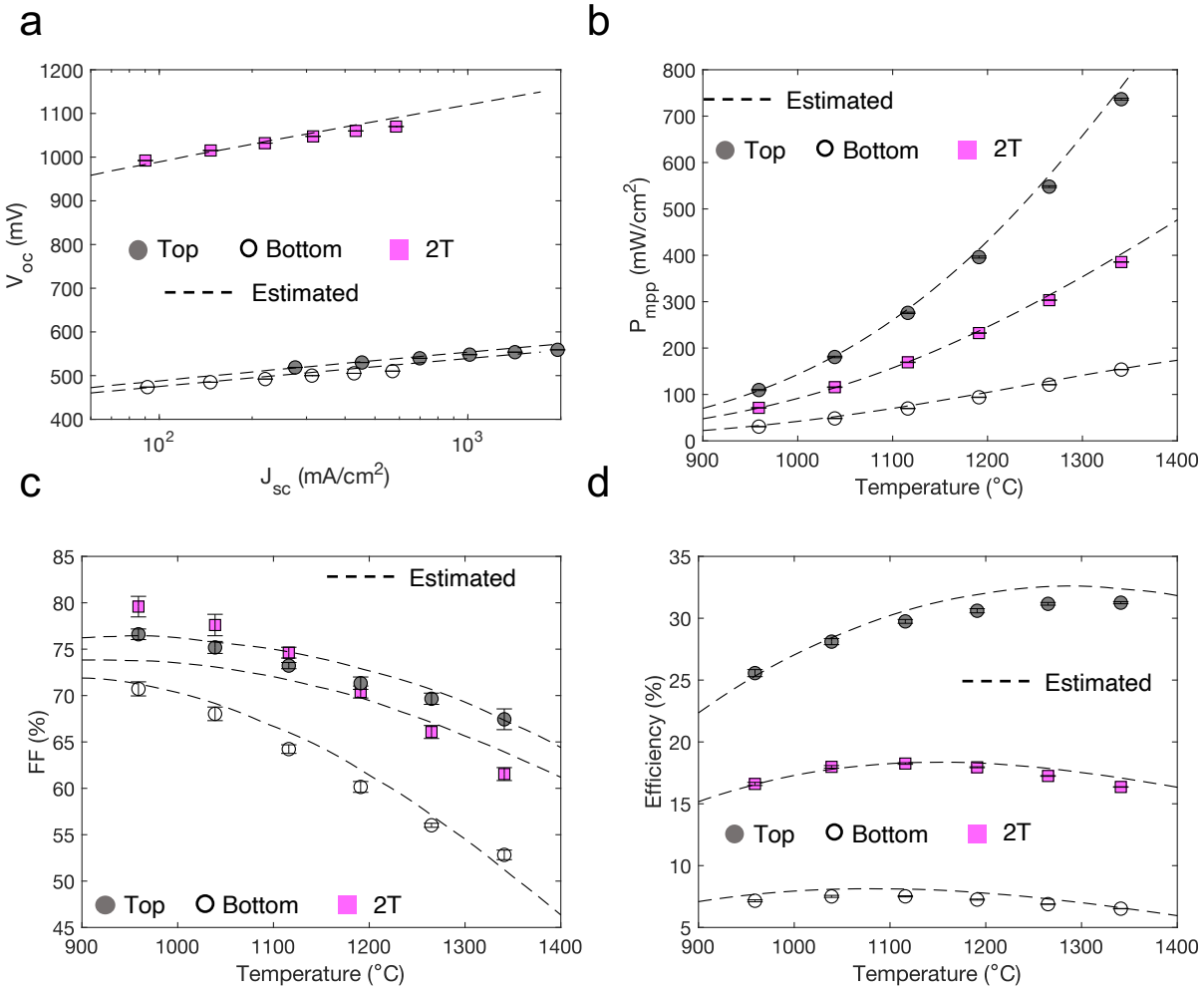

Figure B.1 0.74 eV/0.74 eV InGaAs Homo-tandem cell characterization. a. Open circuit voltage (V_{oc}) versus short-circuit current density (J_{sc}). b. Max-power point (P_{mpp}) versus emitter temperature. c. Fill factor (FF) versus emitter temperature. d. TPV efficiency versus emitter temperature.

Table B.1 Variation in measured open-circuit voltage (V_{OC}), short-circuit current (J_{SC}), fill factor (FF), and power density (P_{mpp}) versus emitter temperature (T_h) for the (a) top cell, (b) bottom cell, and (c) two-terminal operation in the homo-tandem configuration.

(a) Top cell

T_h (°C)	J_{SC} (mA/cm^2)	V_{OC} (mV)	FF (%)	P_{mpp} (mW/cm^2)
959	275.75	518.69	76.605	109.57
1039	453.53	529.99	75.187	180.73
1116	698.18	539.63	73.228	275.89
1191	1013.4	548.01	71.333	396.13
1265	1421	553.65	69.654	548.01
1341	1953.5	559.06	67.442	736.57

(b) Bottom cell

T_h (°C)	J_{SC} (mA/cm^2)	V_{OC} (mV)	FF (%)	P_{mpp} (mW/cm^2)
959	91.583	473.72	70.719	30.681
1039	146.44	484.87	68.028	48.303
1116	220.55	492.12	64.23	69.713
1191	312.26	499.99	60.151	93.911
1265	427.76	505.24	56.016	121.06
1341	569.98	510.26	52.826	153.64

(c) Two-terminal homo-tandem

T_h (°C)	J_{SC} (mA/cm^2)	V_{OC} (mV)	FF (%)	P_{mpp} (mW/cm^2)
959	90.124	992.21	79.586	71.167
1039	146.77	1015.2	77.603	115.64
1116	219.82	1032	74.624	169.29
1191	315.16	1047.5	70.381	232.34
1265	433.06	1060	66.072	303.29
1341	585.44	1070	61.536	385.47

APPENDIX C: Electrical Performance of Heterotandem

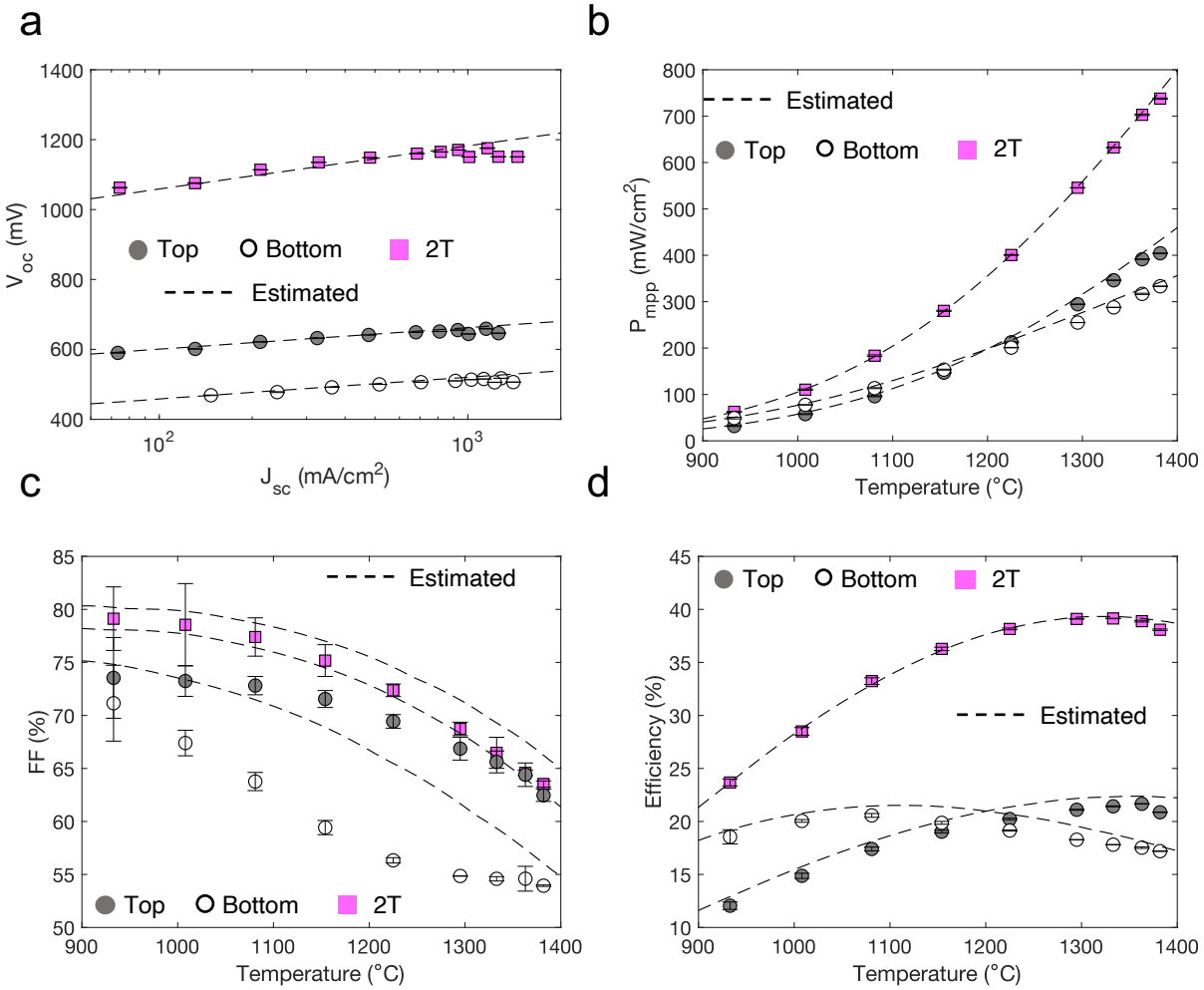

Figure C.1 0.90 eV/0.74 eV InGaAsP/InGaAs Hetero-tandem cell characterization. a. Open circuit voltage (V_{oc}) versus short-circuit current density (J_{sc}). b. Max-power point (P_{mpp}) versus emitter temperature. c. Fill factor (FF) versus emitter temperature. d. TPV efficiency versus emitter temperature.

Table C.1 Variation in measured open-circuit voltage (V_{OC}), short-circuit current (J_{SC}), fill factor (FF), and power density (P_{mpp}) versus emitter temperature (T_h) for the (a) top cell, (b) bottom cell, and (c) two-terminal operation in the hetero-tandem configuration.

(a) Top cell

T_h (°C)	J_{SC} (mA/cm^2)	V_{OC} (mV)	FF (%)	P_{mpp} (mW/cm^2)
933	73.453	589.97	73.542	31.869
1008	130.78	601.3	73.247	57.599
1081	212.4	621.49	72.814	96.119
1154	324.98	632.33	71.55	147.03
1225	477.03	641.33	69.438	212.44
1295	678.36	649.01	66.868	294.4
1333	810.04	651.2	65.615	346.12
1363	927.64	655.23	64.409	391.49
1382	1004.7	644.15	62.47	404.3
1414	1146.1	659.01	62.478	471.87
1434	1256.6	646.36	60.48	491.23

(b) Bottom cell

T_h (°C)	J_{SC} (mA/cm^2)	V_{OC} (mV)	FF (%)	P_{mpp} (mW/cm^2)
933	147.06	468.73	71.154	49.046
1008	241.13	477.78	67.398	77.648
1081	362.43	491.51	63.767	113.59
1154	516.61	499.96	59.424	153.48
1225	704.83	506.23	56.332	201
1295	911.44	510	54.856	254.99
1333	1026.4	513.5	54.589	287.72
1363	1126	515.35	54.598	316.83
1382	1221.1	505.82	53.941	333.18
1414	1281	517.42	54.765	363
1434	1402.9	506.44	54.468	386.99

(c) Two-terminal hetero-tandem

T_h (°C)	J_{SC} (mA/cm^2)	V_{OC} (mV)	FF (%)	P_{mpp} (mW/cm^2)
933	74.468	1062.5	79.126	62.607
1008	130.61	1075.7	78.553	110.37
1081	212.92	1113.9	77.397	183.56
1154	328.41	1135.1	75.173	280.22
1225	482.01	1148.6	72.372	400.68
1295	684.17	1160.1	68.73	545.5
1333	816.59	1164.9	66.477	632.36
1363	929.99	1170.4	64.573	702.83
1382	1009.6	1150.4	63.525	737.8
1414	1157.5	1175.7	60.998	830.09
1434	1256.4	1151	59.592	861.8
1471	1448.9	1150.8	59.419	990.76